AD-A030 430

Library
DRSAR-RDT
AD

EDGEWOOD ARSENAL TECHNICAL REPORT

ED-TR-76070

A TECHNIQUE TO MEASURE THE PRESSURE DISTRIBUTION ACTING ON THE SURFACE OF A SPINNING BODY IN A WIND TUNNEL

by

Miles C. Miller

Development and Engineering Directorate

TECHNICAL LIBRARY

September 1976

DEPARTMENT OF THE ARMY
Headquarters, Edgewood Arsenal
Aberdeen Proving Ground, Maryland 21010

BEST AVAILABLE COPY

Approved for public release; distribution unlimited.

Disclaimer

The findings in this report are not to be construed as an official Department of the Army position unless so designated by other authorized documents.

Disposition

Destroy this report when it is no longer needed. Do not return it to the originator.

REPORT DOCUMENTATION PAGE

READ INSTRUCTIONS BEFORE COMPLETING FORM

1. REPORT NUMBER: ED-TR-76070	2. GOVT ACCESSION NO.
3. RECIPIENT'S CATALOG NUMBER	
4. TITLE (and Subtitle): A TECHNIQUE TO MEASURE THE PRESSURE DISTRIBUTION ACTING ON THE SURFACE OF A SPINNING BODY IN A WIND TUNNEL	5. TYPE OF REPORT & PERIOD COVERED: Technical Report, December 1974 - October 1975
	6. PERFORMING ORG. REPORT NUMBER
7. AUTHOR(s): Miles C. Miller	8. CONTRACT OR GRANT NUMBER(s)
9. PERFORMING ORGANIZATION NAME AND ADDRESS: Commander, Edgewood Arsenal, Attn: SAREA-DE-W, Aberdeen Proving Ground, Maryland 21010	10. PROGRAM ELEMENT, PROJECT, TASK AREA & WORK UNIT NUMBERS: Project 1T662618AH80
11. CONTROLLING OFFICE NAME AND ADDRESS: Commander, Edgewood Arsenal, Attn: SAREA-TS-R, Aberdeen Proving Ground, Maryland 21010	12. REPORT DATE: September 1976
	13. NUMBER OF PAGES: 75
14. MONITORING AGENCY NAME & ADDRESS(if different from Controlling Office)	15. SECURITY CLASS. (of this report): UNCLASSIFIED
	15e. DECLASSIFICATION/DOWNGRADING SCHEDULE: NA

16. DISTRIBUTION STATEMENT (of this Report)

Approved for public release; distribution unlimited.

Copies available from: National Technical Information Service, Springfield, Virginia 22151.

17. DISTRIBUTION STATEMENT (of the abstract entered in Block 20, if different from Report)

18. SUPPLEMENTARY NOTES

19. KEY WORDS (Continue on reverse side if necessary and identify by block number)

Circular cylinder
Magnus effect
Spinning body
Pressure measurement
Wind tunnel testing

20. ABSTRACT (Continue on reverse side if necessary and identify by block number)

This report describes a new experimental technique evolved to measure the pressure distribution on the surface of a spinning body in a wind tunnel. The technique was successfully demonstrated by a series of wind tunnel tests of a spinning cylinder in crossflow. Surface pressure surveys were obtained on the cylindrical model for various tip speed ratios at subcritical, critical, and supercritical Reynolds numbers. The validity of the data was established by comparing the integrated pressure values with directly measured force data. The resulting pressure distribution data allow interpretation of the fundamental Magnus phenomenon and clearly indicate boundary layer and flow separation effects. This testing technique is applicable to various model configurations, angles of attack, and Mach number regimes.

PREFACE

This report presents the results of the initial phase of a study being supported by the AMC Ballistic Technology Program. Specifically, this study was funded under DA Project Title "Research in Exterior Ballistics"; Project 1T662618AH80.

The goal of the study is to experimentally obtain the pressure distribution acting on the surface of an autorotor as described by the author.* This was to be accomplished by means of wind tunnel tests using a new and unique instrumentation scheme. A series of tests was conducted with this instrumentation scheme incorporated into a smooth cylinder model. It was planned to compare these data with previously published data on this basic and heavily investigated shape and, thus, verify the fundamental experimental technique prior to testing the autorotor. However, it was discovered that complete surface-pressure-distribution measurements had never been successfully measured on the spinning cylinder or, in fact, on any spinning body. Because of the excellent results obtained from the initial model tests, it was decided to expand this phase of the study to investigate more thoroughly the pressure distributions on the spinning cylinder.

The results of this effort fully demonstrated the validity of the experimental technique. Since the basic approach can be extended to other applications, it was felt that the results to date should be published prior to the completion of the overall study.

The work described in this report was completed between December 1974 and October 1975.

The use of trade names in this report does not constitute an official endorsement or approval of the use of such commercial hardware or software. This report may not be cited for purposes of advertisement.

Reproduction of this document in whole or in part is prohibited except with permission of the Commander, Edgewood Arsenal, Attn: SAREA-TS-R, Aberdeen Proving Ground, Maryland 21010; however, DDC and the National Technical Information Service are authorized to reproduce the document for US Government purposes.

Acknowledgment

I wish to express my appreciation to several individuals for their contributions toward the completion of this study.

First, I would like to thank Mr. Abraham Flatau, Chief, Weapons Systems Concepts Office, for his encouragement and support during the course of this program.

I also wish to acknowledge the following personnel of the Weapons Systems Concepts Office for their assistance during the wind tunnel testing phases of the program: Mr. John Molnar, Mr. William Kelso, and LT John Dyer.

Finally, I would like to give special acknowledgment to Mr. Owen C. Smith who assisted me throughout this project. His technical support – particularly with regard to the detailed design and fabrication of the model components and associated testing hardware, the arrangement and functioning of the test instrumentation, and his patience and thoroughness during the actual testing operations – was essential to the success of this effort.

*Miller,, M. C. A Proposed Wind Tunnel Testing Method to Measure the Surface Pressure Distribution of an Autorotor. Internal Weapons Systems Concepts Office Report. November 27, 1974.

CONTENTS

A TECHNIQUE TO MEASURE THE PRESSURE DISTRIBUTION ACTING ON THE SURFACE OF A SPINNING BODY IN A WIND TUNNEL

1. INTRODUCTION.

The so-called "Magnus effect" refers to the aerodynamic forces and moments acting on a body which has both a rotational motion and a flight direction which is not aligned with the axis of rotation. The Magnus phenomenon is a fluid dynamic effect and can be best illustrated by the simple example of a smooth right circular cylinder located in a uniform airstream with the longitudinal axis of the cylinder being normal to the direction of the free-stream velocity. Also consider the cylinder to be spinning about its longitudinal axis. Figure A-1 (appendix A) contains a general representation of the local airflow over a particular section of the cylinder as viewed along the longitudinal axis. The streamlines indicate the general direction of the two-dimensional airflow as it passes over the circular-shaped section of the body. The effect of the body spin is to create an unsymmetric flow field over the body. This results in a higher local airflow velocity over the upper surface of the body as opposed to the lower surface.

This velocity differential produces a pressure differential due to Bernoulli's principle. In this example, the lower pressure acting over the upper surface will result in a net upward force being generated on the body. In effect, a Magnus "lift" force is created. Actually, the effect of the spin influences both the lift and the drag acting on the cylinder. The velocity field has established a pressure distribution on the cylinder surface which in turn results in the net forces. The details of the fluid dynamic mechanism involved are quite complex even for this simple case and involve the nature of the boundary layer, flow separation, and their interactions with the aforementioned effects. Many factors such as the Reynolds number, tip speed ratio, and surface roughness determine the specific forces created.

This simple illustration applies directly to familiar examples of the Magnus effect such as the slice of a tennis ball and the flight of a curve ball. The Magnus phenomenon is of particular importance in the ordnance field in the case of spin-stabilized projectiles and other spinning flight vehicles. Although the Magnus effects are small as compared to the nonspinning static aerodynamic forces and moments, they often have a significant influence on the projectile stability and consequent flight motion and trajectory. "Magnus" has been cited as the cause of the poor performance and failures of several projectile-based weapon systems.

Consider a typical spinning projectile flying at an angle of attack as shown in figure A-2. This condition results in a velocity component normal to the projectile longitudinal or spin axis. If a section of the projectile is viewed along the spin axis, a condition results which is somewhat analogous to the simple cylinder case previously described. The actual flow situation involves skewed flow over the entire body and is further influenced by Mach number effects and body surface irregularities. The Magnus forces act along the entire length of the projectile. This distributed Magnus force results in a net Magnus moment about the projectile center of gravity, which can affect the projectile stability.

In the case of spin-stabilized projectiles just discussed, the combination of projectile spin and angle of attack results in a Magnus force and moment which are often the cause of flight instabilities. Even fin-stabilized projectiles which have a relatively low rotation rate possess Magnus

effects which often degrade their flight performance. Sometimes "Magnus" is used to advantage as in the case of autorotor configurations.

The Magnus phenomenon has been extensively investigated by both theoretical and experimental means. An excellent survey of the general Magnus topic including a substantial bibliography pertaining to both theoretical and experimental studies is Jacobson's report.[1] However, experimental data have been limited to force- and moment-type measurements either obtained directly from wind tunnels or indirectly from ballistic ranges.

These data indicate the net results of the Magnus effect. While providing useful information with regard to the projectile flight stability and trajectory, they often do not give an insight into the cause of the resulting forces and moments.

Various experimental flow-visualization techniques have also been evolved to analyze the source of the Magnus phenomenon. These methods are used to determine the general nature of the flow field and are limited to providing a qualitative assessment of the resulting Magnus effects.

Numerous attempts have been made to evolve a fundamental analytical method to describe the Magnus effect from a theoretical fluid dynamic viewpoint. These attempts have been confined to simple body shapes and limited-flow situations and have been only partially successful.

One of the factors preventing the formulation of such a theoretical analysis is the lack of knowledge of the pressure distribution acting over spinning bodies. If such data were available, they could prove to be an invaluable aid toward evolving a theoretical fluid dynamic analysis. In addition, they would represent actual data with which theoretical results could be compared.

This report describes a new experimental technique evolved to measure the pressure distribution on the surface of a spinning body in a wind tunnel. The technique used is unusual in that it avoids the technical problems and operational limitations associated with previous attempts to measure this effect.

The technique was demonstrated by a series of subsonic wind tunnel tests which measure the surface pressure distribution of a spinning right circular cylinder in crossflow. Pressure surveys were obtained for various tip speed ratios and Reynolds number conditions. The validity of the data was established by comparing the integrated-pressure values with directly measured force data. The resulting pressure distribution data allow interpretation of the fundamental Magnus phenomenon and clearly indicate boundary layer and flow separation effects. These are the first such experimental pressure data of this type ever obtained. More importantly, this testing technique can be applied in the future to other body configurations and Mach number regimes. Hence, it would appear possible to gain insights into the Magnus effect in both a basic and applied sense previously unattainable.

II. BACKGROUND.

Experimental determination of the pressure distribution acting on the surface of a wind tunnel model is a basic and vital step in the design and analysis of aircraft, missiles, and other

---

[1] Jacobson, I. D. AGARDograph No. 171. Magnus Characteristics of Arbitrary Rotating Bodies. November 1973.

aerodynamic devices. Yet, up to now, these tests have always been limited to nonspinning conditions. The complete pressure distribution acting on the surface of a spinning body has never been experimentally obtained, even for the most simple cases.

Pressure measurements near the surface of spinning bodies can be obtained indirectly by means of a hot wire anemometer. However, the body surface must not contain any protuberances which could physically interfere with the anemometer probe. In addition, the anemometer probe itself can create local flow disturbances which affect the validity of the measured data.

Simple pressure probes have similar problems. Also, their alignment with the local airflow direction and their proximity to the body surface are critical.

The use of a pressure transducer attached to the surface of the rotating body has several technical drawbacks. The high spin rates result in high cyclic rates of pressure change. The very short time in which the pressure must be measured requires extremely fast response time performance for the transducer. The transducer, rotating with the body, would be subjected to centrifugal loads much larger than the pressure load being measured, making accurate pressure measurements difficult and placing high structural loads on the transducer mechanism.

The technique utilized in this study is fundamentally different from other approaches previously attempted. This concept has only the surface of the model rotating. A pressure tap is located in the nonspinning core of the model and is positioned to measure the pressure on the outside of the body surface at a particular location on the body. The actual pressure-monitoring instrumentation is located outside the tunnel and is, thereby, free of any severe dynamic or environmental effects. The transducer does not spin, and because it measures a constant pressure, the major problems associated with the other approaches are thereby avoided.

The method was evolved in order to measure the surface pressure of spinning configurations whose external surface includes relatively large protuberances. The basic approach, however, can be applied to a variety of both smooth and irregular-shaped bodies. Although the method was demonstrated for a body in pure subsonic crossflow, there do not appear to be any basic limitations in applying it to other Mach numbers and angle-of-attack conditions.

This report includes the results of a series of tests which demonstrate the feasibility of this basic instrumentation arrangement and testing technique.

III. GENERAL APPROACH.

Figure A-3 contains a simplified schematic drawing of a cross-sectional view, looking along the longitudinal axis (i.e. spin axis) of the cylindrical model, and illustrates the basic method of instrumentation.

The model consists of a stationary (i.e., nonspinning) cylindrical core. A pressure tap is located in this core and is oriented radially outward at a fixed angle (ϕ) to the direction of the crossflow. The angle (ϕ) indicates the circumferential location of the pressure tap on the surface of the model thereby defining the point at which the pressure is being measured.

A thin-walled, cylindrical shell is located concentrically around the core. This shell is attached to the core by means of bearings located at each end of the core. The shell is thus free to

rotate or spin about the core and represents the spinning surface of the model body. Shell rotation or spin can be obtained by means of either an internal or an external motor drive arrangement.

A small vent hole is located through the shell such that it will align with the face of the pressure tap once every revolution of the shell about the core. The gap between the face of the pressure tap and the inner surface of the shell is sealed in all directions (i.e., longitudinally and circumferentially) by means of a cylindrical cross-section seal located around the face of the pressure tap.

The cylindrical cavity created within this seal will be open to the pressure acting on the outside surface of the shell when the vent hole is aligned with the tap. When the shell vent hole rotates past this aligned position, the presence of the seal will cause the cavity to retain this pressure.

A pressure tube from the tap is routed through the model core and out of the wind tunnel section through the model attachment strut to a pressure transducer and associated instrumentation equipment located outside of the tunnel. Since the tap is mounted in the fixed core, a direct tubing connection is possible.

Since the vent hole will only be aligned with the cavity for a very short time per revolution, it may require several revolutions of the shell in order to have the pressure in the cavity reach a condition of equilibrium having a constant value equal to that acting on the outer surface of the shell. Thus, the transducer should eventually read a constant pressure with time as shown in figure A-4; that being the pressure acting on the surface of the spinning body at a particular circumferential location relative to the direction of the free-stream velocity.

In this approach, the pressure transducer which is located outside of the tunnel does not spin. Therefore, the transducer does not experience any centrifugal or dynamic loading. This allows a very sensitive transducer to be used without having the accuracy or structure of the transducer affected by dynamic motion. It should be noted that an extremely sensitive transducer is required in order to measure the very low pressure readings. Also, since the pressure reading is constant, the transducer response time is not critical.

Pressure measurements at various points on the surface of the spinning body can be obtained by positioning the core and the attached tap at different attitudes (ϕ) to the airflow. This can be accomplished by simply rotating the core about its longitudinal axis to a particular angle and holding it there sufficiently long to obtain the pressure measurement. This can be done while the tunnel is running and while the model is spinning, allowing a very rapid survey of the surface pressure distribution to be made.

The time to achieve a steady state pressure reading for a given location could be further reduced by increasing the number of holes in the shell. But this could only be done for a smooth, symmetrical model.

Since the pressure is constant, there should be no pressure lag or losses in the tube. This should allow multiple pressure taps to be located within the model at various circumferential and longitudinal locations, thus further reducing the time to complete a pressure survey.

This basic technique should allow the model to be placed at any attitude and any angle of attack. Also, it should work at all Mach number regimes including subsonic, transonic, and supersonic.

Even in the case where a cyclic or nonsteady flow field exists, the instrumentation should still record the average pressure acting on the model which would cause the projectile motion in actual flight.

The most important features of this approach are summarized in figure A-5.

IV. METHOD OF ANALYSIS.

A smooth right-circular-cylinder model was selected to demonstrate the testing technique for several reasons. First, it represents a simple shape that has been heavily investigated, both theoretically and experimentally, especially with regard to the Magnus phenomenon. Secondly, it can be easily converted to an autorotor configuration for the next phase of the study. Further, the pressure distribution over the surface of the cylinder undergoes extreme changes within the Reynolds number range of these wind tunnel tests. Therefore, this configuration represented an excellent means to demonstrate the validity and capabilities of the testing technique.

The absence of any previous experimental pressure data for this specific model configuration required that force test data be acquired with which the pressure data could be compared. Thus, the basic model was initially configured and tested as a force model. Force data, consisting of lift and drag coefficients, were obtained on the model at various tip speed ratios over a Reynolds number range that encompassed subcritical to supercritical conditions. Based on these data, conditions of tip speed ratio and Reynolds numbers were selected at which pressure data would be measured. Specifically, three tunnel velocities were chosen representing a subcritical, critical, and supercritical Reynolds number condition. Tip speed ratios were selected at each condition that would exemplify characteristic Magnus effects.

The cylindrical model was then configured to include the pressure-measuring instrumentation components. Wind tunnel tests were conducted at the selected conditions and the resulting pressure distributions obtained.

The surface pressure distribution for each case was integrated and the resulting force coefficients were compared to the force data obtained directly during the earlier force tests. Thus, the force data from the pressure measurements could be compared to force data developed at the same test conditions on the same model and in the same facility. The correlation of these data verified the validity of the pressure data and demonstrated the feasibility of the pressure measurement technique.

V. FORCE TESTS.

A. Model Description.

Both the force and pressure model are identical in external configuration. The model, as shown in figure A-6, was a right circular cylinder having an outside diameter of 5.171 inches and a span of 8.482 inches. Selection of the model dimensions was based on providing adequate internal volume for instrumentation while not causing unacceptable blockage in the tunnel test section. In addition, it was also desired that the cylinder diameter be such that the model could be tested over the desired Reynolds number range which included both subcritical and supercritical conditions for the velocity range of the wind tunnel.

Circular end plates were located at each end of the cylinder to reduce tip effects. The end plates rotated with the model shell.

Details of the basic wind tunnel model as configured for the force tests are shown in figure A-7. The 4.687-inch-diameter model core was fabricated from aluminum and attached directly to the steel strut with which it was mounted to the tunnel turntable. The steel shell measured 5.171 inches in outside diameter and 8.482 inches in length. The 0.125-inch-thick shell was attached to the core by means of precision ball bearings located at each end of the cylinder. This resulted in a nominal gap between the inside surface of the shell and the outside surface of core of 0.117 inches.

The 10-inch-diameter end plates, located at each end of the cylinder, were attached to an end cap which was, in turn, attached to the shell. The outer edge of the end plates contained a 15-degree bevel, as shown, providing a relatively sharp edge.

Model spin for the force test was achieved by means of a 1/2-horsepower electric motor. This motor was selected because of its high-spin-rate capability and the fact that it could fit completely within the model core. In order to achieve valid force measurements, the model and associated mounting components must be only in contact with the balance. This required that the spin-driving mechanism be an integral part of the model. The model core was fabricated in two halves to allow motor installation. Motor electrical leads were routed down through the mounting strut.

Vent holes were placed in the top end of the model. This allowed cooling air to be drawn from outside the tunnel, through the strut and core, past the motor and out the top of the model. Although the motor included a small cooling fan, the cooling airflow was established due to the low static pressure in the tunnel test section drawing air from outside the tunnel through the strut. The motor was controlled by means of a variable speed switch located outside the tunnel. This allowed the model to be spun at spin rates up to 4300 rpm. Figure A-8 illustrates the model in partially disassembled form showing the location of the internal motor.

B. Test Arrangement and Instrumentation.

The force tests were conducted in the Weapons Systems Concepts Office 28- by 40-inch subsonic wind tunnel. This is an open circuit, continuous flow tunnel. Test section velocity is established by a variable-opening louver forward of the constant speed fan located downstream of the test section. Maximum velocity in the test section is 160 mph. The test section which is 40 inches in width and 28 inches high is relatively long (60 inches) to allow good model wake formation. The turbulence factor of the test section was determined experimentally to be about 1.09. The Plexiglas test section permits excellent visibility of the model being tested. Figure A-9 shows the tunnel test section area.

The cylindrical model was mounted in the wind tunnel such that the longitudinal (i.e., spin) axis was vertical as shown in figure A-10. The lower end of the mounting strut was attached to the turntable located in the test section floor. The turntable is an integral part of the main tunnel balance system. Motor control wiring was routed from the model through the hollow strut and out of the tunnel through the balance area beneath the test section.

Aerodynamic force measurements were obtained by means of a six-component pyramidal strain-gage balance located beneath the test section floor. In addition to having excellent

sensitivity and resolution, this balance possesses negligible interaction characteristics. Thus, the forces and moments indicated do not need to be corrected for interaction effects. The balance indicates the force and moment components relative to the wind axes.

The lift and drag data were then reduced to coefficient form as defined in figure A-11. The force coefficients are based on the projected frontal area of the cylinder.

Output from the force balance is indicated in microvolts and was recorded as a function of time on a strip chart recorder. For these tests, only the drag and side force components were measured. Because of the vertical orientation of the model, the balance side force is actually the lift force acting on the model. This follows the conventional definition of the Magnus lift as being perpendicular to both the free stream and the model spin axis.

The spin rate of the model shell was indicated by a magnetic tachometer located under the model. The tachometer was rigidly attached to the support strut just beneath the lower end plate and was located on the downstream side of the strut to reduce its tare effect. The model spin rate was indicated on a dial instrument and was also recorded as a function of time on the strip chart recorder along with the force measurements.

C. Test Procedure.

The procedure employed during the force test portion of this study was as follows: With the tunnel running, the velocity in the test section was established at the specific value for the particular test run. The model was then spun up, by means of its internal motor, to a spin rate of about 4300 rpm. Power to the motor was then cut off and the spin rate of the cylindrical shell gradually diminished due to bearing friction and external aerodynamic effects. The time histories of the drag and lift force readings from the balance and the cylinder spin rate were simultaneously traced on the strip chart recorder during both the spin-up and spin-down processes. Data were obtained until the spinning ceased. The trace from a typical run is included in figure A-12. The time span for the spin-up phase shown was on the order of 40 seconds. Thus, the change in spin rate with time was relatively mild, effectively eliminating any transient effects due to the change in spin rate. Using this procedure, the aerodynamic characteristics of the cylinder were rapidly obtained over a wide range of tip speed ratios (i.e., spin rates) for a given Reynolds number (i.e., free stream velocity). This type of basic run was repeated at each of the tunnel velocity conditions as indicated in the test program shown in table B-1 (appendix B).

Tare effects, due to the presence of the end plates, strut, and tachometer, were determined by means of separate test runs using the configurations shown in figure A-13 (a, b, and c).

The configuration shown in figure A-13(a) includes all the components present in the basic runs except that the cylindrical body has been replaced by two thin circular-support rods. This arrangement was tested in a nonspinning condition over the same velocity range as the basic runs. Because of the symmetry of the configurations, there was no significant lift force produced. Thus, only the drag force was measured. This model arrangement, designated tare configuration 1, provides the drag of the strut, end plates, and two support rods.

In order to evaluate the drag of the support rods, the model was further tested as shown in figures A-13 (b and c) designated tare configurations 2 and 3, respectively. Both these arrangements included an aerodynamic shield around the strut. This eliminated the relatively large

drag force acting on the strut and allowed a more accurate drag measurement of the remaining portions of the model to be made. Tare configuration 2 included two support rods whereas configuration 3 only had one support rod. The difference in drag between these two arrangements was the contribution due to a single support rod.

This latter value was then doubled and subtracted from the drag data obtained from tare configuration 2. This effectively removed the contribution due to the two support rods, leaving only the drag produced by the end plates and main model support strut. This represents the final drag tare. Figure A-14 shows the drag coefficient obtained as a function of test section velocity. The coefficient is referred to the cylinder reference area. Note that the coefficient is independent of velocity for the range considered. When this is subtracted from the basic runs, the resulting drag coefficient is only that due to the cylinder alone.

Figure A-15 (a through q) presents the lift and drag coefficients as a function of tip speed ratio for each test velocity condition. Data points measured both during the spin-up and spin-down phases are included. It can be seen that, for a given free-stream velocity, the same aerodynamic forces were obtained during spin-up and spin-down except for the velocity range between 110 and 140 mph. This hysteresis effect at the higher velocities is characteristic of the spinning cylinder and will be discussed in detail later. The fact that identical data were achieved regardless of the spin acceleration indicates that the varying spin test procedure produced results equivalent to a constant spin rate condition. The coefficient data obtained during these tests show excellent correlation with results published by numerous other investigators. (Swanson's paper is an excellent example.)[2]

It should be noted that the cylindrical model used in these tests represented a specific aspect ratio (i.e., span to diameter ratio) and included a particular end plate configuration and size. These physical factors influence the magnitudes of the coefficients and their specific relationship to tip speed ratio and Reynolds number when compared to other referenced data. However, the trends and phenomena occur which are typical of a spinning cylinder in crossflow.

D. Test Results.

The major purpose of the force tests was to obtain data with which the pressure test results could be compared. Favorable agreement between the forces obtained from integrating the measured pressure distribution and the forces measured directly would demonstrate the validity of the pressure measurement techniques. Consequently, a limited number of test conditions (i.e., combinations of free stream velocity and model spin rate) were selected for subsequent pressure tests. A further consideration was to select test conditions which would exemplify typical characteristics of the aerodynamics of the spinning cylinder. Accordingly, three free-stream velocity conditions were selected. These represented a typical subcritical, supercritical, and near-critical Reynolds number condition for the nonspinning cylindrical model.

The drag coefficient of a nonspinning cylinder undergoes an abrupt change between a Reynolds number of 300,000 to 500,000. This transient area is termed the critical Reynolds number range. Below this Reynolds number range, in the so-called subcritical area, the drag coefficient has a relatively high value. As the Reynolds number is increased through this range, the drag coefficient suddenly decreases. Above this Reynolds number range, the drag coefficient

[2]Swanson, W. M. The Magnus Effect: A Summary of Investigations to Date. pp 461-470. J. Basic Eng. Trans. ASME. September 1961.

remains constant at the lower value. This is termed the supercritical condition. The critical Reynolds number for a cylinder is roughly defined at the Reynolds number at which the drag coefficient value is halfway between these two relatively constant values.

The fluid dynamic mechanism for this effect primarily involves the nature of the boundary layer and depends on the turbulence level of the air and model surface roughness. These effects will be discussed in more detail in the section on the pressure test results. At this point, it will suffice to say that the pressure distribution on the surface of the cylinder undergoes very drastic changes in this Reynolds number range which result in a large change in the drag force.

Figure A-16 shows the drag coefficient as a function of velocity for the nonspinning cylindrical model with end plates used in the force tests. Note that the critical Reynolds number occurs at a tunnel velocity of about 90 mph.

Based on this, test velocities of 60 mph and 120 mph were selected as representative subcritical and supercritical test conditions. The three velocity conditions selected and their respective Reynolds number are summarized below:

Condition	Velocity	Reynolds number
Subcritical	60 mph (88 ft/sec)	250,620
Critical	90 mph (132 ft/sec)	375,930
Supercritical	120 mph (176 ft/sec)	501,240

Figure A-15(j) contains the lift and drag coefficients as a function of tip speed ratio for the 60-mph subcritical Reynolds-number condition. The lift remains zero with increasing tip speed ratio up to a tip speed ratio of about 0.1. Above this tip speed ratio, the lift becomes negative up to a tip speed ratio of 0.5 where the lift coefficient becomes increasingly positive with increasing tip speed ratio. The drag coefficient remains fairly constant up to a tip speed ratio of 0.1. Above this tip speed ratio, the drag coefficient experiences a gradual reduction in value until a tip speed ratio of about 0.4, where it remains constant with increasing tip speed ratio.

For this subcritical condition, tip speed ratios of 0, 0.2, and 0.75 were chosen for subsequent tests with the pressure model. These points are indicated by the circled numbers 1, 2, and 3 in figure A-17(a). Condition 1 represents the nonspinning subcritical condition; condition 2 lies within the region of negative lift; and the positive lift region is represented by condition 3.

Figure A-15(m) shows the force coefficients measured at the critical Reynolds number condition of 90 mph. For this situation, the lift coefficient of the cylinder becomes strongly negative as soon as spin is initiated, and remains negative until a tip speed ratio of about 0.45. Above this tip speed ratio, the lift coefficient becomes increasingly positive with increasing tip speed ratios. The drag coefficient gradually decreases from a tip speed ratio of zero to about 0.4, above which it remains a constant with increasing tip speed ratio. Here again, the three tip-speed-ratio conditions chosen for the pressure tests were selected to represent the basic nonspinning case, the negative lift region, and the positive lift region. These conditions are indicated by points 4, 5, and 6 in figure A-17(b).

Force coefficients, obtained at the supercritical Reynolds number condition shown in figure A-15(p), include an interesting effect that was first noted during the force test. During the

spin-up phase of this test run, the lift increased with increasing spin rate until a tip speed ratio of about 0.4. At this point, the lift abruptly decreased to a near-zero value, where it again increased positively with increasing spin rate. During the spin-down phase, the lift values matched those of the spin-up phase at the higher spin rates, but continued this trend down into the negative lift condition. At a tip speed ratio of 0.2, the lift suddenly jumped up to the positive trend and coincides with the previous spin-up values. This hysteresis effect occurs because of an unstable flow situation characteristic of this Reynolds number and tip speed ratio condition. As shown in figure A-17(c), tip speed ratios designated as 7, 8, and 10 were selected as the nominal conditions for the pressure tests at the supercritical Reynolds number. In addition, pressure tests were conducted at condition 9 to investigate the unstable flow regime.

VI. PRESSURE TESTS.

A. Model Description.

The internal details of the pressure model are contained in figure A-18. This model utilized the same components as the force model except for the core element. The pressure model core was machined from a single piece of aluminum which attaches directly to the hollow support strut with the strut hole extended up through the center of the core piece. A circular hole located at midspan extended radially from the center of the core to the outer surface. All the pressure-measuring elements were contained within this radial hole.

The pressure tap component consisted of a cylindrical brass element containing a .046-inch-diameter circular hole through its center. The tap included a circumferential shoulder on the outer surface to facilitate its mounting to the seal block. The inner end of the tap was composed of a stem component, to which the plastic pressure tubing could be attached.

The pressure tap was held in position by means of the seal block. The cylindrically shaped seal block consisted of an outer section made of Teflon and an inner section made of brass. These two sections were placed over the pressure tap and threaded together. A flat circular rubber washer was included between these pieces, as shown, to prevent air leakage between the seal block sections. The surface of the outer end of the Teflon seal block component was shaped to the contour of the inner surface of the shell. A semicircular groove was then machined into this face. A rubber "O" ring washer was then placed into this groove. This washer represents the most important element of the system in that it provided the sealing function between the pressure cavity and the rotating cylindrical shell and is the key to the success of the testing technique. The circular "O" ring used in these tests was termed a "quad-ring" due to its four-sided cross-sectional shape. The "O" ring was not directly attached to the seal block, but was held in the groove by means of vacuum grease. Vacuum grease was also placed on both the outer and inner sides of the ring to aid in sealing and provide a lubricating effect.

The seal block not only positioned and aligned the pressure tap in the core hole, but formed the cavity between the face of the pressure tap and the inner surface of the rotating shell. This entire assembly was free to translate radially in and out of the core hole. Sealing was aided by means of four small coil springs located within the spring block which acted to press the seal block and rubber "O" ring against the inner surface of the shell.

The final component consisted of the retention block which functions as a spacer to position the pressure tap seal block and spring block assembly toward the outer end of the core hole.

A 0.0625-inch-diameter vent hole is located through the shell at the center span location. The inner edge of this hole was slightly rounded to prevent it from cutting into the rubber "O" ring seal as it slid by. Dimensional details of the seal area are shown in figure A-19.

A photograph of the seal components prior to assembly is contained in figure A-20. The model assembly procedure was as follows: The model core was attached to the support strut. This could be done before the model was placed in the tunnel test section. The pressure tube, which was routed up through the strut and core, was pulled through the core hole and attached to the pressure tape of the assembled seal components as shown in figure A-21(a). The entire seal assembly was then placed into the core hole as illustrated in figure A-21(b). The shell, with the bottom end plate removed, was slid down over the core from the top. The seal assembly was manually pushed into the core hole to allow the shell to slip by. A portion of the bearing retention step, running circumferentially around the lower inside surface of the shell was cut out to allow the seal to slide past. With the shell in place, the bottom end plate was attached, locking the model together.

B. Test Arrangement and Instrumentation.

The pressure tests were conducted in the same wind tunnel facility as were the force tests, described previously. Figure A-22 shows the details of the model installation in the wind tunnel. Model spin was obtained by means of an external drive motor arrangement. The two-horsepower, constant-speed, electric motor was mounted on top of the wind tunnel. A drive shaft extended from the top end of the model out through a hole in the roof of the test section. A series of pulley wheels of different diameters was fabricated that could be used in various combinations on both the motor shaft and the model drive shaft. In this way, the 1950-rpm motor could spin the model at spin rates of approximately 1000, 2000, 3000, 4000, and 5000 rpm. Figure A-23 shows the motor installation arrangement.

The model core was attached to the single support strut which, in turn, was mounted to the turntable located beneath the test section floor. The turntable included its own motorized drive mechanism. A control box, located outside the tunnel, allowed the turntable to be rotated through 360 degrees and set at any yaw angle within a 0.1-degree increment. This allowed the core and pressure tap to be rapidly set at the desired angle to the flow. The shell and attached end plates could rotate freely around the core as in the force test. Only the airflow over the cylindrical portion of the model was of interest for the pressure tests. This area is effectively screened by the end plates. Thus, the presence of the drive shaft, the presence of the tachometer, and the movement of the tachometer with yaw did not affect the pressure data. Although the model was mounted to the turntable and balance, no aerodynamic loads were measured during the pressure tests.

A schematic, describing the instrumentation arrangement used in the pressure test, is included in Figure A-24. The pressure in the cavity was transmitted from the pressure tap and out of the tunnel by means of flexible plastic tubing. The 0.125-inch (inside diameter) tubing was attached directly to the pressure tap and routed down the model core and support strut through the floor of the test section where it was attached to one end of the plenum cylinder. The plenum cylinder was simply a 0.25-inch-thick aluminum cylinder measuring 7.0 inches in length and 2.5 inches in diameter with caps at each end to form a closed contour as shown in figure A-25.

The combination of the volume in the model cavity (forward of the pressure tap), the internal tubing volume, and the volume of the plenum cylinder provides a sufficient volume reservoir to reduce any transient pressure noise effects. Thus, the constant pressure in the model

cavity is the dominant pressure in the plenum cylinder. This pressure was measured by means of a transducer located at the other end of the plenum cylinder. A commercially available strain-gage-type transducer was used for these tests. The unit used was a Statham differential pressure transducer, model PM131TC, having a ±10-psi maximum-pressure capability. This instrument measured the pressure in the model cavity relative to the test section static pressure. The reference pressure input to the transducer was attached directly to a standard static pressure probe located in the tunnel test section upstream of the model. A relatively sensitive pressure transducer is required because of the low pressure characteristics of these flow characteristics. For example, in these tests pressure readings within 0.01 psi were required. This illustrates one of the major advantages of this technique, in that the transducer is not subjected to a severe dynamic environment, which would require specially "hardened" transducer of decreased sensitivity. The fact that a constant pressure is being measured eliminates any requirements for high transducer response performance. This factor also lends itself toward the use of a very sensitive transducer, since rapid response characteristics are not critical. The electronic signal from the transducer was traced out as a function of time on the strip chart recorder, as was the output from the magnetic tachometer.

The reading of a constant pressure inherent in this technique simplified the overall instrumentation scheme from another standpoint. That is, the measuring instrumentation can all be located outside of the model and the tunnel test section in an area free from dynamic and environmental effects which could degrade the performance of the instruments. The length of the pressure tubing is not critical and, in fact, is beneficial in damping out any environmental transient signals. Figure A-26 shows the tunnel arrangement for the pressure tests.

C. Test Procedure.

The pressure tests involved two separate procedures depending on whether the model was nonspinning or spinning. Prior to either type of test, a static calibration of the pressure transducer and a check of the seal were conducted. A special fixture was used consisting of a short tube stem placed on the outside of the cylinder shell over the vent hole. The vent hole was initially positioned over the model cavity (i.e., the pressure tap). This stem was held in place by a metal hose clamp placed around the cylinder as illustrated in figure A-27. The inner surface of the stem fixture included a rubber ring seal to prevent leakage between the stem and the vent hole. This fixture allowed direct attachment to a small compressor by which the model cavity can be submitted to either an overpressure or a vacuum of a precise magnitude. This pressure was indicated by the transducer and proper calibration could be completed.

Static checkout of the rubbing seal could be accomplished by rapidly rotating the shell a few degrees until the vent hole was past the cavity. If the seal was functioning, the pressure in the cavity was retained.

For the nonspinning tests, the shell was locked to the core by means of a set screw such that the vent hole was positioned directly over the pressure tap. Thus, both the core and shell could be set at a particular angle to the flow by means of the tunnel turntable. With the tunnel running at the desired velocity, the model was rotated through a complete 360-degree revolution in 5-degree increments by means of the tunnel turntable. At each 5-degree position, the cylinder was stopped and the pressure reading obtained. The basic terms utilized in the pressure tests are defined in figure A-28.

For the pressure tests on the spinning model, the set screw was removed so that the shell could rotate relative to the core. The testing procedure was to first establish the airflow in the tunnel test section at the desired velocity. The spin motor, which had been set up with the proper pulleys for the spin rate desired, was turned on which rapidly brought the cylindrical shell up to the steady-state spin-rate condition. The core was then rotated through a complete 360-degree revolution in 5-degree increments similar to the nonspinning tests. Core rotation is accomplished by means of the tunnel turntable. The core was held at each position until the pressure reading assumed a constant value.

Typical pressure data obtained from tests on the spinning cylinder are shown in figure A-29 (a and b). The examples shown are for the same free-stream velocity and model spin rate, but for different values of ϕ. For these two test runs, the vent hole was initially aligned with the pressure tap at a particular circumferential position (i.e., value of ϕ). With the tunnel running, and the model not spinning, the pressure indicated is the value at that position for the nonspinning condition. The motor was then turned on bringing the cylinder up to the steady spin rate desired. The desired spin rate was achieved very rapidly (approximately 1 second for the cases shown). Note that a finite time is required for the pressure reading to change from the nonspinning value to that for the spinning condition. Figure A-29(a) shows data measured on the nose area of the cylinder (i.e., $\phi = 0°$). This represents a positive pressure region, relative to the free-stream static pressure. Figure A-29(b) contains data obtained in a negative pressure area (i.e., $\phi = 90°$). Note the low magnitude of the pressures being measured.

The most common procedure followed, however, was to rotate the core to the desired position, to hold it there until the pressure measurement was obtained, then to move it to the next position while the model was spinning. Rotation of the core to the new ϕ position only required a few seconds. A few more seconds were then required to allow the new pressure reading to stabilize as illustrated in figure A-30. This procedure was then repeated. In this manner, a very rapid survey of the surface pressure over the circumference of the model was accomplished. The wind tunnel test program for the pressure tests is included in table B-2.

Figure A-31 contains data obtained at selected values of ϕ for a typical test run, and illustrates the manner in which the pressure data vary over the surface of the model. Similar data were obtained at 5-degree increments over the entire circumference of the cylinder surface. The pressures were then reduced to coefficient form as defined in figure A-28.

Additional comments relative to the testing arrangement and procedure are included in section VIII, E. These have been included in a separate section so as not to detract from the actual testing methodology utilized.

D. Test Results.

The data, resulting from the pressure test runs, are presented in figures A-32 through A-41. The length of each radial arrow is proportional to the magnitude of the pressure coefficient acting on the model outer surface at that particular circumferential location. The direction of the arrow indicates whether the pressure is positive (directed toward the surface) or negative (directed away from the surface). This method graphically illustrates the pressure distribution acting on the surface of the cylindrical model. In addition, the pressure distribution for each run was integrated over the surface of the cylinder to obtain the resultant lift and drag force coefficient. Derivation of the pressure integration equations and definition of terms are described in figure A-42. The circumferential pressure distribution obtained in the wind tunnel test was measured at the midspan

location of the cylinder. In integrating this pressure to obtain the resultant force coefficients, it is assumed that the pressure distribution does not vary along the cylinder length. The actual pressure coefficient values as measured were used in compiling the integrated force value. No data smoothing was involved in this process.

In order to compare the force coefficients obtained from the measured pressure data with the coefficients measured directly during the force tests, both the tip speed ratio and Reynolds number conditions had to match for both types of tests.

Although the pressure test runs were made at the previously selected free stream velocities, the ambient temperature and pressure resulted in a Reynolds number condition somewhat different than that present during the force tests. Also, mechanical effects resulted in slightly different spin rates (and consequently, a different tip speed ratio) than planned. However, enough force data had been obtained to allow interpolation of any Reynolds number and tip speed ratio value.

Consequently, the lift and drag coefficients measured during the force tests were plotted as a function of Reynolds number for constant tip speed ratio equal to that used in each of the pressure runs. The specific lift and drag coefficient coresponding to the Reynolds number of the pressure test could then be determined. Figure A-43 includes the lift and drag coefficients plotted as a function of Reynolds number for all the tip speed ratios of the ten pressure runs. The coefficients determined by each means are summarized in table B-3. The excellent agreement between the coefficient values determined by integrating the pressure profiles and the coefficient values measured directly during the force tests demonstrate the validity of the testing technique.

E. Comments.

The previous sections described the arrangement and procedures used to obtain the experimental results presented in this report. As with any new test technique, this final arrangement was the result of evaluating various components and procedures and making changes or modifications as required. The following comments are intended to illustrate certain instances which provide further background into the evolution of the current test setup. This information might be useful toward future applications of the technique.

The original approach for the seal assembly was to have the Teflon seal block alone provide the rubbing-seal function. It was hoped that the combination of preshaping the outer surface of the seal block to the inner contour of the shell would result in the airtight seal desired. Also, the rubbing action of the Teflon against the shell would act to wear the seal block into an exact fit and better seal. This was the reason for selecting Teflon as the material for the seal block component. Preliminary tests with this approach revealed severe leakage, even with a polished inner shell surface. Accordingly, it was decided to add a rubber "O" ring to the end of the seal block in order to create a line seal rather than the area seal of the plain seal block. The "O" ring resulted in a much improved seal and was used from then on.

Originally, the transducer was located inside the model within the seal assembly. Initial testing of this arrangement produced a transducer output signal which occurred as a function of the shell rotational position. When spinning, this produced a periodic signal which appeared to be caused by seal leakage. Attempts to eliminate the leakage concentrated on using different washer "O" ring configurations and spring sizes. Increasing the spring force (i.e., causing the seal to press

tighter against the inner surface of the shell) appeared to improve the sealing. However, the periodic change in transducer output still occurred.

It was then determined that the periodic signal from the transducer was not due to seal leakage but was, in fact, caused by transducer acceleration. This acceleration resulted from model vibration during spin. The model was fabricated to close tolerances and did not possess an observable motion while spinning. Even a minute acceleration, however, produced a large signal relative to the very small pressures being measured.

The transducer was then replaced by a simple brass pressure tap. The external shaping of the tap was identical to that of the actual transducer so that the existing seal assembly components could be retained. The transducer itself was located outside the tunnel at the end of 6 feet of plastic tubing.

Tests with this arrangement showed a marked improvement, in that it eliminated the acceleration effect without any leakage occurring. However, the signal from the transducer did possess a considerable amount of noise superimposed onto the valid signal. This noise was evidently due to small pressure oscillations between the pressure tap and the transducer. The addition of the aluminum plenum cylinder effectively damped out this effect, resulting in a smooth pressure signal from the transducer. Figure A-44 illustrates the improvement in signal quality obtained by locating the transducer outside of the model and these increases of the reservoir volume between the model vent hole and the transducer face.

The existing strong springs were retained from the actual pressure tests. These springs caused the seal assembly to press against the shell with a force of about 16 pounds and resulted in relatively large friction. No attempt was made to investigate whether this force could be reduced without degrading the seal performance.

During the course of the tests with the cylindrical model, pressure data were measured at spin rates as high as 5000 rpm. Because of the high friction inherent in this type of seal, the electric motor could not sustain this spin rate long enough to obtain a complete circumferential survey. The motor would hold this spin rate for a few minutes until it overheated at which time an automatic switch turned the motor off. Several hours were then required to allow the motor to cool off before it could be run again. This prevented accomplishment of a complete survey.

However, the pressure measured over a portion of the cylinder surface held steady values and appeared to be valid in sign and magnitude. These results indicate that the present seal design will provide valid pressure data at conditions where the velocity of the shell to the seal is as high as 115 feet per second.

The pressure wind tunnel tests were conducted during the summer months. This situation resulted in an "insect" problem. During these tests, gnats and other small insects were drawn into the wind tunnel test section from outside. During a run, these insects became deposited onto the front surface of the model, increasing the surface roughness of the model. This effectively acted as a transition grit, and had a profound effect on the formation of the boundary layer and consequently affected the pressure distribution. This was especially troublesome at the subcritical and critical Reynolds number condition. The problem was solved by periodically cleaning the model surface free of bugs after every few pressure measurements.

VII. ANALYSIS OF PRESSURE DATA.

A. General.

The manner in which the aerodynamic forces acting on the spinning cylinder vary with spin and free stream velocity have been previously investigated by means of conventional force-type wind-tunnel tests and flow visualization studies. Theoretical and experimental studies, which included both force and pressure tests using nonspinning cylinders, have revealed the importance of the boundary layer to the flow field and resulting forces acting on the nonspinning cylinder. These results have then been extended to explain the mechanism behind the forces acting on a spinning cylinder and other general Magnus situations.

In particular, the interaction between the different types of boundary layer, tip speed ratio, Reynolds number, and resulting flow field has previously been used to qualitatively describe the pressure distribution and consequent forces acting on the spinning cylinder.[1]

However, the data obtained during this study provide the first experimental verification of the pressure distribution resulting from these effects. Thus, it was felt appropriate to briefly discuss and illustrate these effects by using the pressure distribution data obtained in this study.

B. Nonspinning Cylinder.

Potential flow theory can be used to predict the pressure distribution on the surface of a nonspinning cylinder in uniform flow. This approach combines the velocity potential for a doublet and a uniform flow to generate the two-dimensional flow field about a circular cross-sectional shape. The equation for the resulting pressure distribution on the surface of the circle is shown below:

$$C_P = \frac{P - P_\infty}{q_\infty} = 1 - 4 \sin^2 \phi$$

where

C_P = pressure coefficient ($\Delta P/q_\infty$)

P = pressure

P_∞ = free-stream static pressure

q_∞ = dynamic pressure ($P_\infty V_\infty^2/2$)

ϕ = angle defining location on circumference of cylinder at which pressure is measured

This approach assumes an inviscid, incompressible fluid and is thus independent of Reynolds number and Mach number effects. Figure A-45 presents a plot of the pressure distribution based on this ideal situation. Note that, as the air approaches the nose area, it decelerates as it turns to flow around the body. This results in a positive pressure region on the nose of the cylinder.

The airflow achieves a higher than free-stream velocity as it passes around the sides of the body, resulting in a large negative pressure on the upper and lower portions of the cylinder. The minimum pressure point corresponds to the point of maximum velocity which occurs at the $\phi = \pm 90$ degree locations. After this point, the air gradually slows down, turns into and accelerates up to the free-stream flow. The streamline pattern on the rear surface of the cylinder is the mirror image of that on the front surface. This results in identical pressure distribution on front and rear areas of the body. In addition, because of the body and flow symmetry, the pressure distributions on the upper and lower surfaces are identical. Thus, integration of the pressure results in both zero net lift and drag forces.

These results are, of course, at variance with actual experimental results where a net drag force is always present. For the subsonic case considered here, the main reason for the difference is the assumption that the fluid is inviscid. Air does possess viscosity resulting in the development of a thin layer of slow-moving air along the surface of the body. The basic nature of this so-called "boundary layer" is illustrated in figure A-46 which shows the airflow over a flat plate. In the simple case shown, the plate is very thin and includes a sharp beveled nose so that no flow field is created by the plate shaping. No airflow occurs directly at the surface of the plate. (This is an observed fact and is termed the "no slip" condition.) However, the air velocity increases with increasing distance from the surface until it assumes the full value for the local flow at that point. In the case of the flat plate, this would be the free-stream velocity. The region in which this change of velocity occurs is termed the boundary layer. The boundary layer increases in thickness as it moves back from its point of initiation.

In the initial portion of the boundary layer, the velocity gradient across the boundary layer has a definite profile. Further down the plate, the boundary layer will become thicker, and a greater portion of the layer will consist of low-velocity air. At some point, airflow within the boundary layer will actually contain an area of reverse flow. This breakdown of the boundary layer has the effect of pushing the airflow away from the body surface. This "separation" causes the airflow to create a region of multidirectional, high-velocity, swirling air termed a wake.

The airflow outside of the boundary layer acts as if it were inviscid and will assume a flow field in accordance with potential theory being influenced by the body shape and the physical presence of the boundary layer. All viscous effects are limited to the boundary layer. The flow within the boundary layer creates viscous or friction drag, which is usually a small proportion of the total drag. The presence of the boundary layer, however, can create very large effects in the overall flow field around the body because it influences the separation point.

There are basically two different types of boundary layer, which are essentially characterized by the general shape of the velocity profile. At conditions where there is little transverse fluid motion within the boundary layer, a so-called "laminar" boundary layer will exist. These conditions would include a low free-stream Reynolds number, low turbulence flow, and low local Reynolds number (i.e., in the early portions of the boundary layer). The general laminar boundary profile is shown in figure A-47(a). This type of boundary layer is relatively thin and results in low friction drag. However, it tends to separate very easily.

The other type of boundary layer is termed a "turbulent" boundary layer. This type of boundary layer has a somewhat fuller profile as illustrated in figure A-47(b) and is characterized by the presence of transverse random motion of the fluid, normal to the body surface. A turbulent boundary layer is considerably thicker than the laminar type and it causes a higher degree of friction drag. However, it is less prone to separate than the laminar type.

High Reynolds number situations, airflow having a high turbulence level, and relatively rough body surface conditions are conducive to the formation of a turbulent boundary layer. Even in conditions where a laminar boundary layer is initially formed, it will become turbulent at some distance down the body (i.e., at a higher local Reynolds number). This change from laminar to turbulent usually occurs very abruptly.

The separation of both types of boundary layer is influenced by several factors as described in chapter 2 of Schlichting's monograph.[3] For the situation considered in this study the most important considerations are the effects of free-stream and local Reynolds number, surface roughness, body shaping, and surface motion. The effect of Reynolds number and surface roughness primarily effect the type of boundary layer formed which, in turn, determines the location on the body at which separation will occur.

The shape of the body affects the pressure gradient over the surface of the body in the direction of flow. The nature of this pressure gradient will either act to initiate or delay separation. If this pressure gradient is negative (i.e., the local pressure decreases in the direction of the airflow), separation will be delayed. This would occur in a region on the body surface where the flow was accelerating such as on the nose. Conversely, a situation where the pressure increases in the direction of the airflow (i.e., positive pressure gradient) will facilitate separation. This latter "adverse" pressure gradient situation occurs in regions of decelerating flow and is the primary cause of the flow separation characteristic on the back surfaces of bodies.

The effect that the type of boundary layer has on the separation point is the major factor behind the subcritical and supercritical drag phenomena. For example, consider the pressure distribution measured over the nonspinning cylindrical model at the subcritical Reynolds number (case 1) as shown in figure A-48. In this case, because of the low free-stream Reynolds number, the boundary layer formed on the front surface of the cylinder is laminar. This boundary layer remains laminar and, because of its unstable nature, separation occurs on the front surface of the cylinder. The effect of this flow separation is to create a large wake region behind the cylinder. The wake results in a constant and relatively large negative pressure acting over the entire rear surface of the cylinder aft of the point of separation. This area of negative pressure acting on the cylinder results in the high drag force characteristic of the subcritical condition.

Figure A-48 also includes subcritical pressure distribution data from Schlichting.[3] Note that the results from the Edgewood Arsenal study indicate a somewhat earlier separation and a lower value of negative pressure in the base region. This is primarily due to the differences in the test conditions. The flow is subcritical in both cases as evidenced by the early separation point and the relatively high drag coefficient value obtained. However, the higher Reynolds number condition of the Edgewood Arsenal data, being closer to the critical Reynolds number, is somewhat within the transition region between the subcritical and supercritical condition. In this transition region, the base pressure undergoes a gradual increase from the high negative value of pure subcritical condition prior to the shift in separation point which is the dominant effect. In addition, the presence and size of the end plates used with the Edgewood Arsenal model contribute some effect. However, for the purpose of this study, the 60-mph test condition is representative of the subcritical phenomena.

Figure A-49 shows the pressure distribution obtained in this study at the supercritical Reynolds number conditions (case 7). In this case, because of the high free-stream Reynolds

[3]Schlichting, Dr. H. Boundary – Layer Theory. Sixth edition. McGraw-Hill Book Company, New York, New York. 1968.

number, a turbulent boundary layer is initially formed on the front surface of the cylinder. Because of the inherent stability of the boundary layer, it does not separate until it reaches a point on the back surface of the cylinder. This results in a smaller wake and produces less of a negative pressure over the rear surface of the cylinder than occurs at the subcritical condition. Note also, the reduced magnitude of the negative base pressure. Both of these effects result in a marked reduction in drag for the supercritical condition as compared to the subcritical condition. Comparison of these data with a representative supercritical pressure distribution (also included in figure A-49) shows similar general effects. The differences between these two sets of data are again due to Reynolds number and the end plate effects.

Figures A-48 and A-49 illustrate the essential characteristics of the subcritical and supercritical conditions and describe the influence of the boundary layer on the resultant pressure distribution and aerodynamic forces. In the case of a nonspinning cylinder, the type of boundary layer formed under each condition is the major factor which influences the flow separation and the consequent pressure distribution.

C. Spinning Cylinder.

Potential flow theory has also been developed to describe the flow over a rotating cylinder as follows:

$$C_P = 1 - 4 \sin^2 \phi + 4 \hat{\omega} \sin \phi - \hat{\omega}^2$$

where

C_P = pressure coefficient ($\Delta P/q_\infty$)

ϕ = angle defining location on circumference of cylinder at which pressure is measured

$\hat{\omega}$ = tip speed ratio ($\omega d/2 V_\infty$)

In this case, a doublet, point vortex, and uniform flow are superimposed to result in an expression for the two-dimensional flow field over a rotating circular shape. As with the nonspinning case, inviscid theory results in an idealized pressure distribution shown in figure A-50 which is not achieved in actual experiments. This difference can also be explained by considering the effects of viscosity and the resultant boundary layer.

The motion of the body surface, relative to the direction of flow, influences the type of boundary layer formed as discussed by Schlichting, chapter 14.[3] If the surface is moving in the same direction as the flow, it has the effect of reducing the velocity gradient across the boundary layer normal to the surface. As far as the air is concerned, it is passing over the surface at a reduced velocity as illustrated in figure A-51(a). This reduction in the effective Reynolds number will allow a laminar boundary layer to be formed and retained on a moving surface at higher free-stream Reynolds number than would be possible on a stationary surface.

Conversely, if the surface were moving in an opposite sense to the flow, as shown in figure A-51(b), it would result in a higher effective Reynolds number. In this situation, the boundary layer would tend to become turbulent at a lower free-stream Reynolds number than would be the case with a nonspinning surface.

Translational movement of the body surface, parallel to the airflow, also has a profound effect on the flow separation. Movement of the surface in the same direction as the airflow has the effect of decreasing the velocity gradient across the boundary layer and thus delaying separation.

In effect, the moving surface gives the profile a shaping similar to that normally possessed earlier in the boundary layer for a stationary surface case. Thus, in the presence of a moving surface, the boundary layer is not at the stage conducive to separation until further along the body surface. Conversely, movement of the surface, opposite to the flow direction, acts to cause separation earlier.

In the case of this study, surface motion is a result of cylinder spin. A condition where the surface motion is in the same direction as the airflow exists on the region of the cylinder retreating due to spin. This region would be in the upper portion of the cylinder for the spin sense shown in the pressure plots. Conversely, the lower side of the cylinder would be advancing and would represent the surface moving opposite to the direction of the airflow.

Thus, the interrelation of four factors influencing the separation point can be used to interpret the pressure distribution and consequent forces measured on the spinning cylinder.

These four factors are shown in figures A-47 and A-51 and include:

1. The presence of a laminar boundary layer,

2. The presence of a turbulent boundary layer,

3. The surface movement in the same direction as the flow, and

4. The surface movement opposite in direction to the flow.

The existence and specific interaction of these four conditions is a function of the free-stream Reynolds number and tip speed ratio for the cylindrical model considered. All of these factors are based on the fact that they depend on the *relative* motion of the airflow and the model surface. In this regard, it is helpful to also consider the local effective Reynolds number which is based on the velocity of the airflow over a particular point on the body surface relative to the velocity of the surface at that point. This approach is discussed in detail in reference 1. The seemingly complex results of the force wind tunnel tests can be fully and simply explained by interpreting the pressure distributions measured during the pressure wind tunnel tests with regard to the interaction of these four factors.

D. Analysis of Pressure Distribution Data.

As was noted previously, the Magnus phenomenon affects both the lift and the drag forces. Discussion of the Magnus effect usually centers on the lift force generated because of its unique presence due to the effect of spin and its dominant effect as compared to the drag. The pressure distribution profiles graphically illustrate both the directional sense (positive or negative) and the relative magnitude of the resultant lift and drag forces.

Figure A-52 (a, b, and c) includes the pressure distribution measured on the cylindrical model at the subcritical Reynolds number condition for tip speed ratios of 0, 0.25, and 0.79,

respectively. For the nonspinning case shown in figure A-52(a), the boundary layer formed is laminar due to the low Reynolds number free-stream condition. The airflow in the nose region of the cylinder initially decelerates relative to the free-stream value, resulting in a region of positive pressure. The airflow then accelerates as it continues around the front face of the cylinder, resulting in the formation of the negative pressure region on the top and bottom of the cylinder. This laminar boundary layer separates on the front side of the cylinder. It should be noted that the specific location of the separation cannot be determined from the pressure distribution profile. This is demonstrated for the case of a nonspinning body in Prez and Pitkin's report.[4] However, the pressure profiles do indicate the general area in which separation occurs. At separation, the flow breakdown results in a pressure drop to a constant negative value which acts over the entire portion of the cylinder aft of the separation point. Because of the symmetry of flow, the pressure distribution is also symmetrical relative to the upper and lower surfaces of the cylinder.

Figure A-52(b) shows the pressure distribution at the same free-stream velocity, but with the cylinder spinning at a tip speed ratio of 0.25. Because of the rotational sense of the cylinder, an unsymmetrical flow field and pressure distribution result. Consider the flow situation over the top of the cylinder (i.e., the retreating side relative to the free-stream velocity). The boundary layer over this portion of the cylinder is laminar, as in the nonspinning case. However, the motion of the upper surface due to the cylinder spin is in the same directional sense as the local airflow. This velocity of the surface, relative to the free-stream velocity, has the effect of delaying separation on the upper surface until a circumferential location, further aft than for the nonspinning case, is reached. Beyond this point, the pressure assumes the constant negative value identical to that of the nonspinning case.

Because the motion of the lower surface is opposed to the direction of the free-stream velocity, this region is, in effect, at a higher local Reynolds number. Thus, the boundary layer over the bottom of the cylinder becomes turbulent. This allows the boundary layer to remain attached to the cylinder surface for a greater distance back than was possible for the laminar boundary layer present in the nonspinning case. However, the motion of the cylinder surface, being opposite to the flow, causes the turbulent boundary layer to separate more forward than was the case for the nonspinning supercritical case. The separation point is also affected by the degree of development of the turbulent boundary layer. In this case, both the top and bottom areas of the cylinder possess greater negative pressure regions than for the nonspinning case. However, a greater negative pressure acts over a larger area on the bottom resulting in the net negative lift force for the complete cylinder.

If the cylinder spin to tip speed ratio is increased to 0.79, the pressure distribution measured appears in figure A-52(c). The laminar boundary layer established in the upper surface remains attached to the surface due to the retreating movement of the cylinder surface over a considerably longer distance than for the latter two cases. On the bottom of the cylinder, the turbulent boundary layer formed by the advancing motion of the cylinder surface is forced to separate at a more forward location because of adverse (i.e., advancing) motion of the cylinder surface. This results in a net negative pressure on the upper surface of the cylinder with a consequent net positive lift force. There is also an indication of a slightly downward shift of the stagnation point on the front surface of the cylinder. This effect would become more pronounced at higher tip speed ratios, but would never achieve the large shifts predicted by potential flow theory.

---

[4]Prez, W. M., Jr., and Pitkin, E. T. Flow Separation over Axisymmetric Afterbody Models. AIAA Journal of Aircraft, Vol II, No. 11, pp 677-682. November 1974.

For a given Reynolds number condition, the magnitude of the surface pressure acting on the cylinder in the wake area remains constant. The location of the flow separation not only affects the size of the wake area, but it also influences the amount of negative pressure acting over the front surface of the cylinder. Both factors contribute greatly toward the net drag coefficient value. For example, from figure 52 (a, b, and c), it can be seen that the reduction in drag coefficient that occurs with the increasing spin rate for the cases shown is primarily a result of the increased areas of negative pressure which exist on the front surface of the cylinder as the spin rate is increased. This effectively decreased the drag coefficient.

The pressure distributions, obtained at the free-stream velocity corresponding to the (nonspinning) critical Reynolds number, are shown in figure 53 (a, b, and c) for tip speed ratios of 0, 0.167, and 0.53, respectively. Pressure data for the nonspinning cylinder at the critical Reynolds number is very difficult to obtain because of the unstable nature of the flow. As shown in figure A-52(a), the boundary layer is initially laminar, but is on the verge of changing to turbulent. If a laminar boundary layer exists, separation occurs on the front surface of the cylinder as in the case shown. The resulting negative base-pressure coefficient is lower in value than for the subcritical case. Pressure readings on the top and bottom tended to fluctuate between two pressure profiles; one represents a laminar boundary layer with its early separation and the other a turbulent boundary layer with its later separation. This fluctuating effect was experienced during the force tests.

As soon as the model possessed some spin, the forces and pressure distribution readings became more stable. Figure A-53(b) shows the pressure distribution obtained at a tip speed ratio of 0.167. Here again, because of the reduced local Reynolds number, a laminar boundary layer is firmly established on the upper surface and is then prevented from separating because of the retreating motion of the cylinder surface. In contrast, on the bottom, the relatively low spin motion is sufficient to establish a turbulent boundary layer with a consequent rearward shift in the separation point. Thus, the bottom of the cylinder possesses a large area of negative pressure, resulting in the large negative lift force previously obtained during the force tests.

In figure A-53(c), the tip speed ratio has been increased to 0.53. Here, again, the region of positive pressure on the nose has shifted slightly toward the underside of the model. The laminar boundary layer on the upper surface does not separate until it reaches a point on the back surface of the cylinder. But the effect of spin is now sufficient to cause early separation of the turbulent boundary layer on the bottom of the cylinder. This results in a reduced area of negative pressure over the bottom of the cylinder. The net lift is now near zero. A further increase in spin rate would result in additional forward shift of the bottom separation point with a consequent increase in positive lift.

Pressure data for the supercritical condition is presented in figure A-54 (a, b, c, and d) for tip speed ratios of 0, 0.125, 0.266, and 0.39, respectively. The nonspinning case shown in figure A-54(a) shows the effect of the turbulent boundary layer on both the upper and lower surfaces with a consequent separation point well into the back surface of the cylinder. Also of note is the reduced magnitude of the negative base pressure as compared to the previous free-stream velocity conditions.

A tip speed ratio of 0.125 at this Reynolds number results in the pressure distribution contained in figure A-54(b). Here, the turbulent boundary layer on the upper (retreating) surface is less turbulent due to the motion of the body surface being in the same directional sense as the airflow. Consequently, the separation point on the upper surface has moved forward slightly. Note

also that, when separation occurs on the front surface of the cylinder, the resulting drop in surface pressure is gradual as opposed to the more abrupt change experienced with separation on the back side. Separation of the turbulent boundary layer on the lower surface occurs more forward than the nonspinning case because of the adverse relative surface motion. The overall result is a net positive lift.

The data shown in figure A-54(c) are for a tip speed ratio of 0.266. This condition is within the tip speed ratio range where the unstable flow effects were obtained during the force tests and relates to test condition 9 as shown in figure 17(c). Note how the lift force could assume either of two distinct values. The reason for these dual results is revealed by the pressure data in figure A-54(c). The separation point of the turbulent boundary layer on the lower surface is caused by the advancing movement of the cylinder surface. However, on the upper surface, both the type and subsequent separation of the boundary layer are affected by the motion of the retreating surface of the cylinder. For this specific free-stream velocity and tip speed ratio, the local Reynolds number present on the upper surface is right at the point where either a laminar or a turbulent boundary layer could be created. If the boundary layer is laminar, the separation point occurs considerably more forward than with the turbulent boundary layer. The pressure distribution plot shows the fluctuation between these two situations obtained during the pressure tests. The dashed lines indicate the resulting profiles if each condition were to be fully established. If a laminar boundary layer were formed, there would be a larger negative pressure area on the bottom of the cylinder than on the top, resulting in a net negative lift force. Whereas, if a turbulent boundary layer were established, the pressure profiles on the upper and lower sides would be nearly identical, resulting in a near-zero lift force for this particular tip speed ratio.

This example also illustrates how the pressure distribution data determined by means of the testing technique can be used to evaluate transient or unsteady phenomena.

Figure A-54(d) shows pressure data for the supercritical condition at a tip speed ratio of 0.39. This tip speed ratio is beyond the unstable region just discussed. Here, a turbulent boundary layer is fully established in both the upper and lower surfaces with the respective separation points being determined by the favorable or adverse surface motion of the cylinder. In this case, a positive lift is generated.

VIII. FUTURE APPLICATIONS.

With the feasibility and validity of the testing technique demonstrated, several future applications are being considered.

This particular project effort will be extended to measure the pressure distribution on the surface of an autorotating configuration. For this effort, the current cylindrical model will be modified to a cylindrical autorotor by the addition of four spanwise driving vanes on the exterior of the shell as illustrated in figure A-55. Because of the irregular surface of the autorotor, the pressure distribution is also a function of the external surface feature. Thus, pressure readings at various locations relative to the driving vanes will be obtained as illustrated in figure A-55. Data will be obtained at the inherent autorotating-tip-speed ratio for this configuration. It is hoped that the resulting pressure distributions will allow a better understanding of the relatively complex flow phenomena associated with these devices. Also, this type of information could aid in evolving a theoretical fluid dynamic analysis.

This general testing technique can be applied to a variety of model configurations, model orientations to the airflow (i.e., angles of attack and yaw), and speed regimes including subsonic, transonic, and supersonic. The method could be utilized to investigate specific Magnus-related problems including the boattail area of spin-stabilized projectiles, the tail region of fin-stabilized missiles, and the nose portion of spinning bodies. Figure A56 contains schematic model designs for these particular examples.

Multiple pressure taps can be incorporated into a wind tunnel model at several locations along the length of the model. The circumferential pressure distributions obtained at various longitudinal locations will provide the pressure distribution acting over the surface of the entire model. Figure A-57 illustrates this approach as applied to a model of a spin-stabilized artillery projectile. This model could include actual body features such as the obturating ring and rotating band. The pressure data, resulting from this arrangement, could provide an insight into the cause of the Magnus-associated flight instability which has plagued several Army artillery systems.

The simple rubbing "O" ring seal configuration utilized in this study demonstrated the validity of the testing technique. Variations of this basic design can be used in a variety of Magnus-related investigations. However, the large rubbing friction and relatively large size inherent in this seal approach may impose limits on its application with regard to a model size and spin rate.

Accordingly, an alternate seal design, based on the use of a magnetic fluid, is being pursued. A magnetic fluid consists of a collodial suspension of ferrite particles in a carrier liquid. A variety of carrier liquids can be used ranging from hydrocarbons to plain water. The resulting magnetic fluid retains the chemical and mechanical characteristics of the carrier liquid. The ring-shaped magnetic fluid provides the seal function desired. This type of seal can hold a large pressure differential and, more importantly to this application, provide a very low-friction moving seal. A seal component based on a magnetic fluid has been designed and fabricated under an Edgewood Arsenal contract by Ferrofluidics Corporation. This seal is compatible with the cylindrical wind tunnel model described in this report. The basic configuration and dimensions of this seal are shown in figure A-58. A series of wind tunnel tests are planned to evaluate the performance characteristics of this seal design. If successful, this seal design would be applicable to very small wind tunnel models and very high spin rates.

IX. SUMMARY.

Spinning projectiles have occasionally shown erratic flight motion which has been attributed to the Magnus phenomenon. This fluid dynamic mechanism has been extensively investigated by both theoretical and experimental means. However, experimental data have been limited to force-type measurements either obtained indirectly from ballistic ranges or directly from wind tunnel tests. A detailed understanding of the Magnus effect has been hampered by the total lack of definitive experimental data describing the pressure distribution on the surface of spinning bodies. If this type of pressure data were obtained, it could provide a key element in assessing the flow field and boundary layer interactions and the resulting Magnus forces as they affect future projectile designs and flight performance.

This report describes a new experimental technique evolved to measure the pressure distribution on the surface of a spinning body in a wind tunnel. The technique is unique in that all elements of the instrumentation are internal to the model or are located outside of the wind tunnel. Thus, the approach avoids the technical problems and operational limitations associated with

previous attempts to measure this effect. The technique was successfully demonstrated by a series of wind tunnel tests of a spinning cylinder in crossflow. Surface pressure surveys were obtained on the cylindrical model for various tip speed ratios at subcritical, critical, and supercritical Reynolds numbers. The validity of the data was established by comparing the integrated-pressure values with directly measured force data. The resulting-pressure-distribution data allow interpretation of the fundamental Magnus phenomenon and clearly indicate boundary layer and flow separation effects. These are the first such experimental pressure data of this type ever obtained. More importantly, this testing technique can be applied in the future to other body configurations, angles of attack, and Mach number regimes. Hence, it would appear possible to gain insights into the Magnus effect in both a basic and applied sense previously unattainable. The results of the work described in this report were presented at the Ninth Aerodynamic Testing Conference sponsored by the American Institute of Aeronautics and Astronautics.[5]

X. CONCLUSIONS.

1. This study has demonstrated the validity of a new testing technique by which the aerodynamic pressure distribution acting on the surface of a spinning body can be measured in the wind tunnel.

2. Integration of the resulting-pressure-distribution data not only provided a quantitative measure of the Magnus forces but the pressure distribution profile allows interpretation of the boundary layer and flow separation effects.

3. Although the spinning right circular cylinder in crossflow was used to demonstrate the approach the basic technique can be applied to a variety of model configurations, angles of attack, spin rates, and Mach number regimes.

[5] Miller, M. C. A Technique to Measure the Pressure Distribution on the Surface of Spinning Wind Tunnel Models. Proceedings, AIAA Ninth Aerodynamic Testing Conference. pp 91-99. June 1976.

GLOSSARY

b	Span of cylindrical model
C_D	Drag coefficient ($D/q_\infty S$)
C_L	Lift coefficient ($L/q_\infty S$)
C_P	Pressure coefficient ($\Delta P/q_\infty$)
D	Drag force
d	Diameter of cylindrical model
F	Total aerodynamic force
L	Lift force
P	Pressure
P_∞	Free-stream static pressure
P_a	Ambient pressure
q_∞	Dynamic pressure ($P_\infty V_\infty^2/2$)
R	Radius of cylindrical model ($d/2$)
R_d	Reynolds number ($V_\infty d/\nu$)
S	Reference area (bd)
t	Time
t_a	Ambient temperature
u_R	Velocity of airflow in boundary layer relative to body surface
u_S	Velocity of moving surface
u_∞	Velocity at outer edge of boundary layer
V_∞	Free-stream velocity
α	Projectile angle of attack
ΔC	Arc length on circumference of cylinder
ΔP	Pressure referred to free stream static pressure ($P - P_\infty$)
ρ_∞	Air density

μ	Viscosity
ν	Kinematic viscosity (μ/ρ_∞)
π	Ratio of circumference of circle to radius of circle
ϕ	Angle defining location on circumference of cylinder at which pressure is measured
ω	Spin rate
$\hat{\omega}$	Tip speed ratio ($\omega d/2V_\infty$)
i	Index denoting discrete location on the surface of the cylinder at which pressure is being measured

APPENDIX A

FIGURES

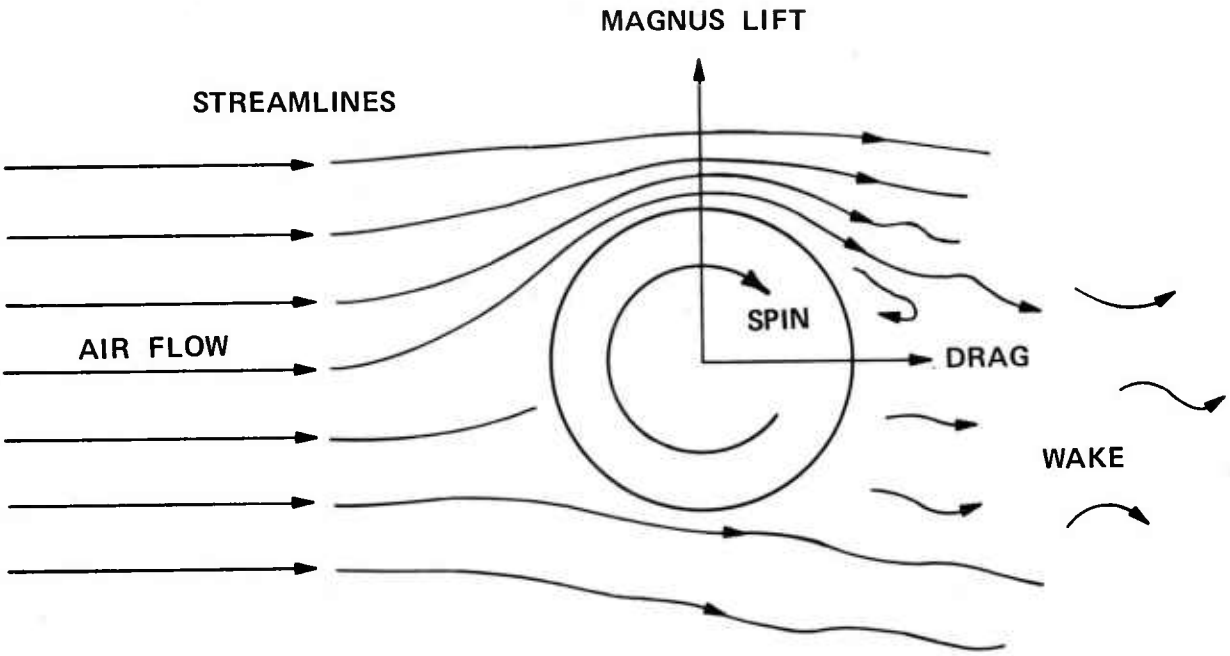

Figure A-1. Basic Magnus Phenomenon

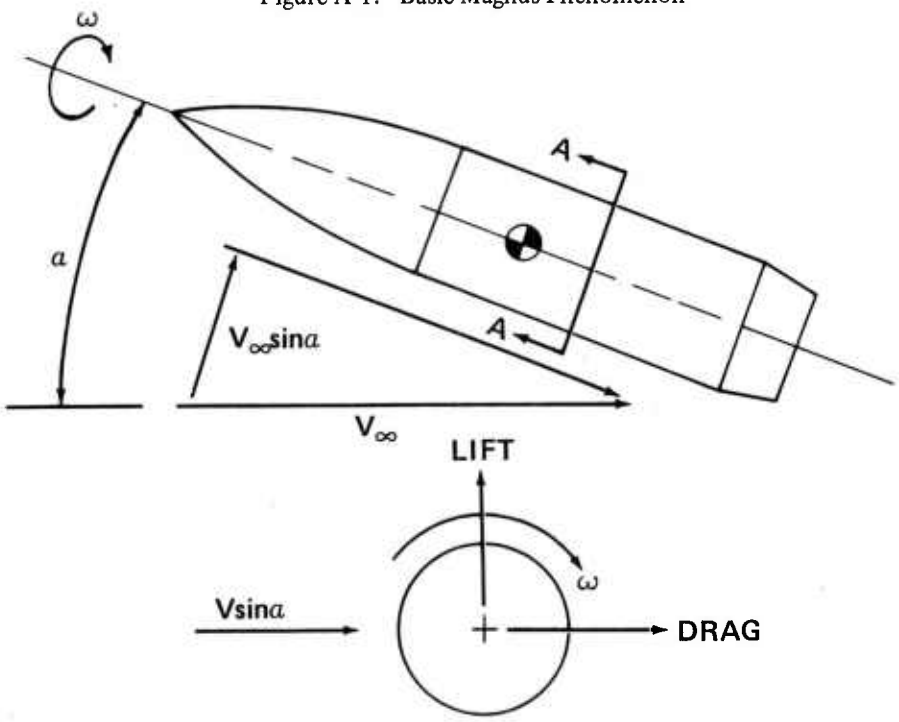

Figure A-2. Spinning Projectile

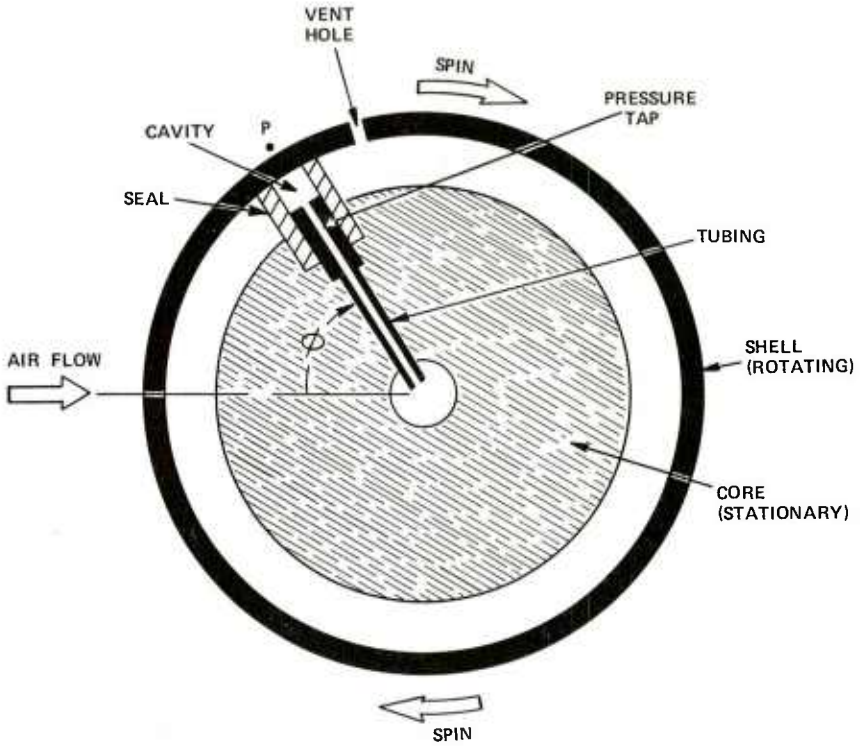

Figure A-3. Schematic of Model Interior Illustrating Basic Instrumentation Approach

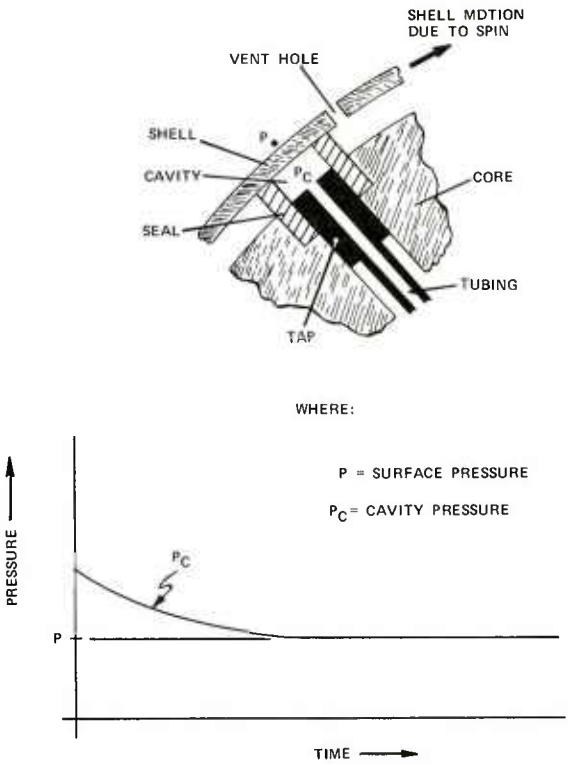

Figure A-4. Schematic of Seal Component

- ALL ELEMENTS OF INSTRUMENTATION LOCATED WITHIN MODEL OR OUTSIDE TUNNEL TEST SECTION
- NO INERTIAL OR DYNAMIC LOADS ACTING ON TRANSDUCER
- DIRECT CONNECTION BETWEEN PRESSURE TAP IN MODEL AND INSTRUMENTATION OUTSIDE TUNNEL
- CONSTANT PRESSURE READING DOES NOT REQUIRE HIGH RESPONSE TRANSDUCER
- RAPID PRESSURE SURVEYS POSSIBLE
- APPLICABLE TO ANY MODEL ORIENTATION TO FREE STREAM
- CAN BE USED IN ANY SPEED REGIME (SUBSONIC, TRANSONIC AND SUPERSONIC)
- WILL FUNCTION WITH MODELS HAVING IRREGULAR EXTERNAL SURFACE FEATURES

Figure A-5. Features of Testing Technique

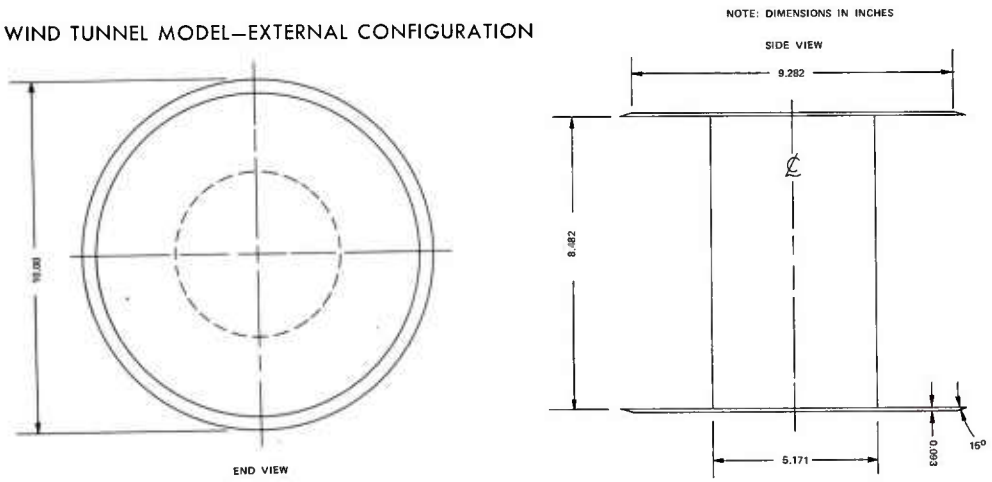

Figure A-6. Wind Tunnel Model – External Configuration

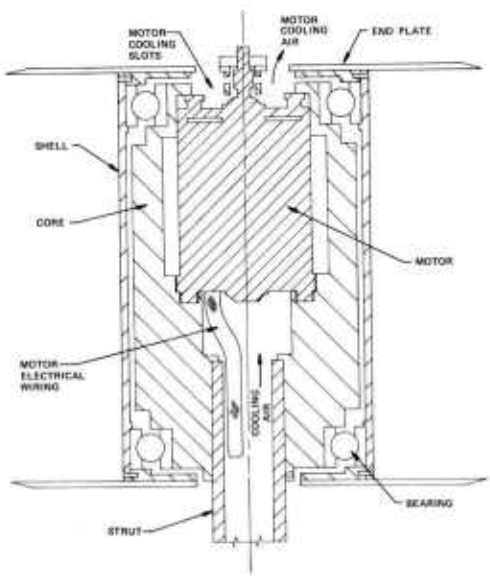

Figure A-7. Internal Details of Force Model

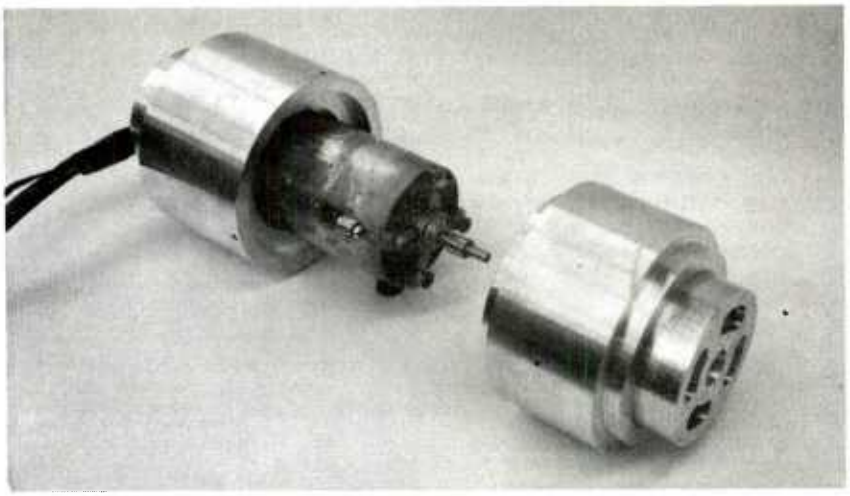

Figure A-8. Model Core Disassembled to Show Electric Spin Motor

Figure A-9. Edgewood Arsenal 28- by 40-Inch Subsonic Wind Tunnel

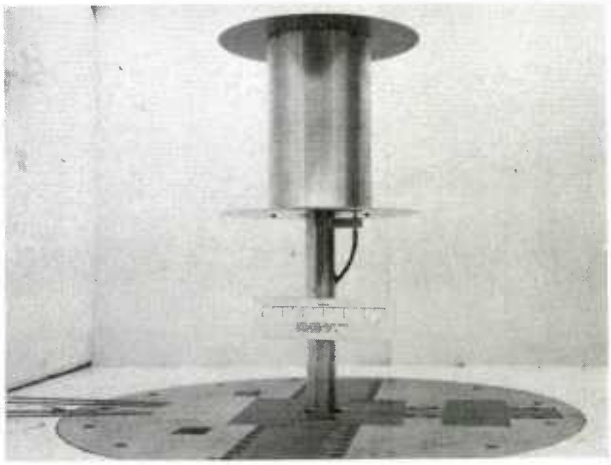

Figure A-10. Model Installed in Tunnel for Force Tests

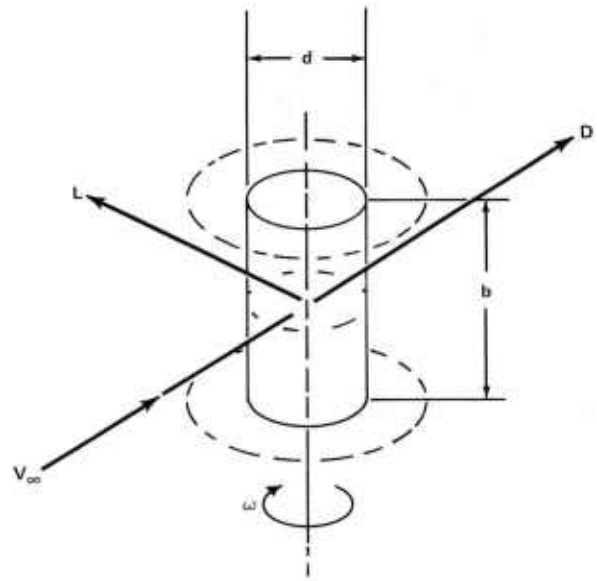

$$C_L = \frac{L}{q_\infty S} \qquad S = db$$

$$C_D = \frac{D}{q_\infty S} \qquad q_\infty = \frac{\rho_\infty V_\infty^2}{2}$$

$$\hat{\omega} = \frac{\omega d}{2V_\infty}$$

Figure A-11. Definition of Force Test Terms

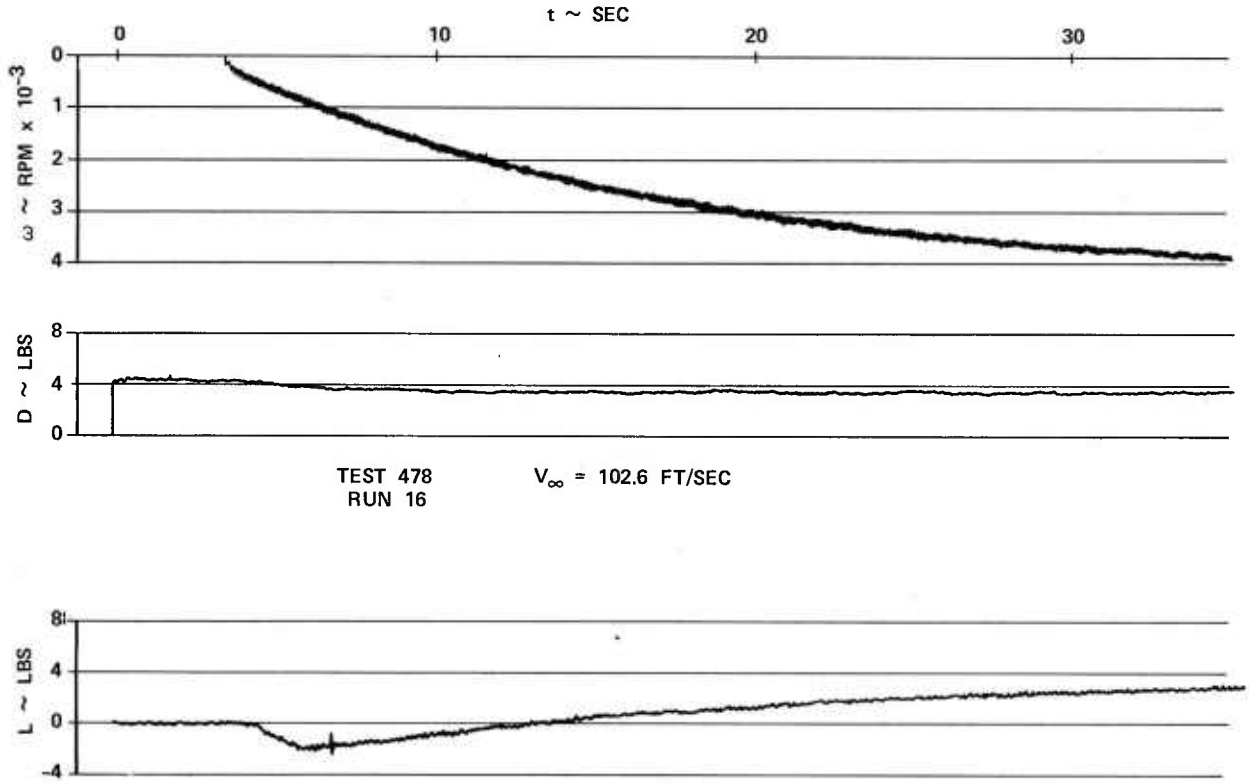

Figure A-12. Typical Force Data Traces

a. Configuration No. 2 – Tare b. Configuration No. 3 – Tare c. Configuration No. 4 – Tare

Figure A-13. Model Configurations Utilized to Determine Force Test Tare

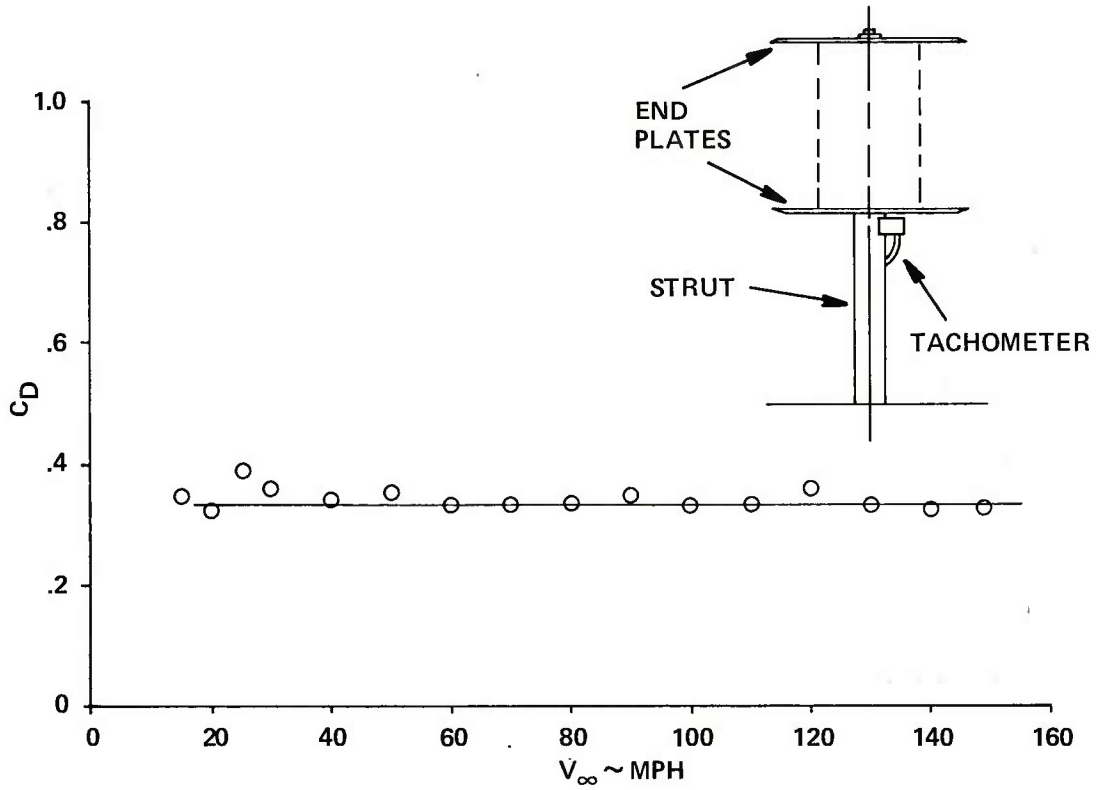

Figure A-14. Tare Drag Coefficient Versus Test Section Velocity

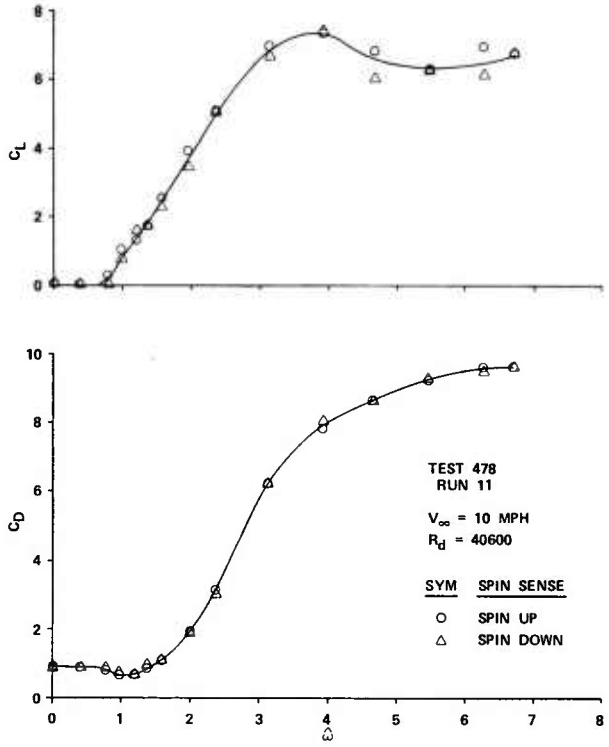

a. $R_d = 40600$

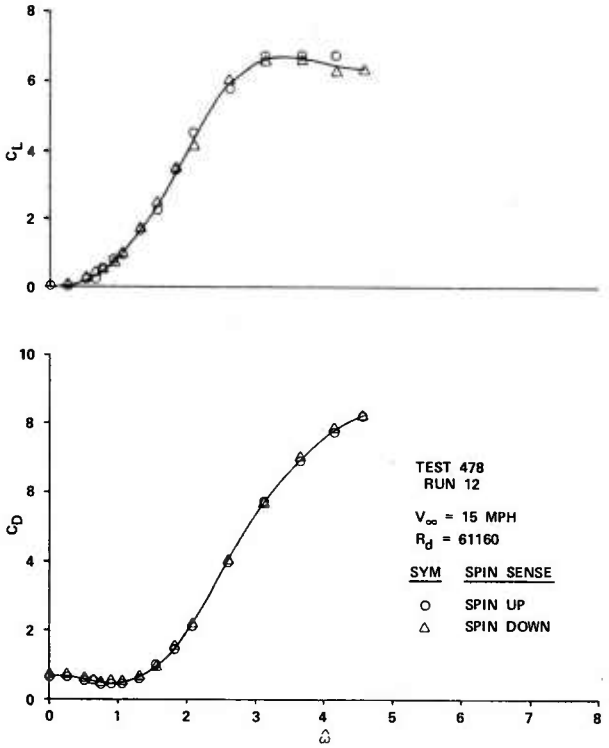

b. $R_d = 61160$

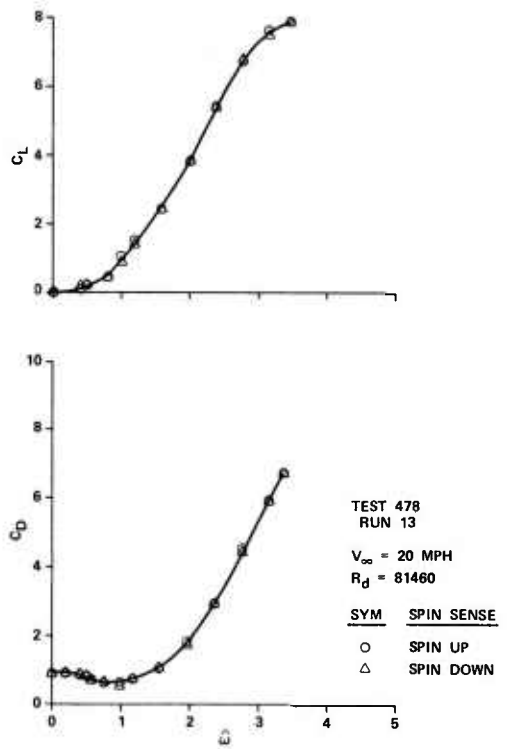

c. $R_d = 81460$

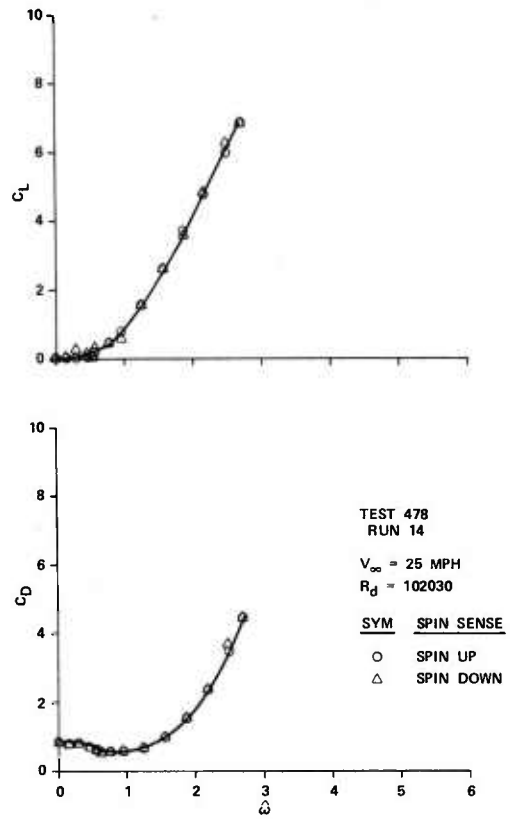

d. $R_d = 102030$

Figure A-15. Lift and Drag Coefficient as a Function of Speed Ratio

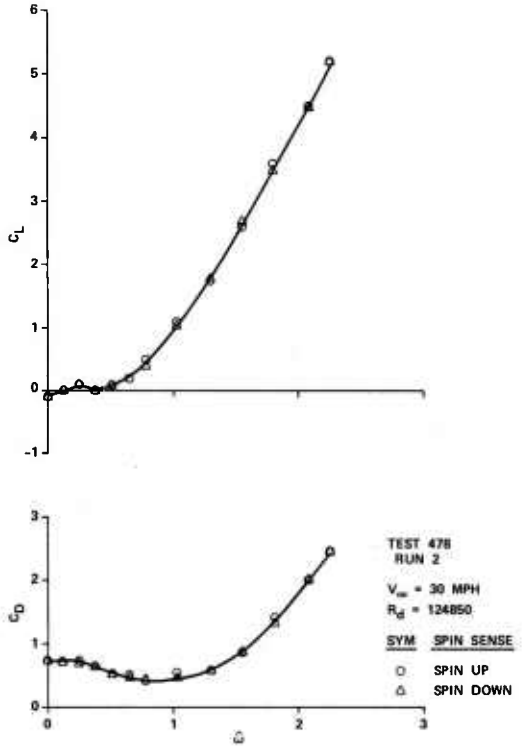

e. R_d = 124850

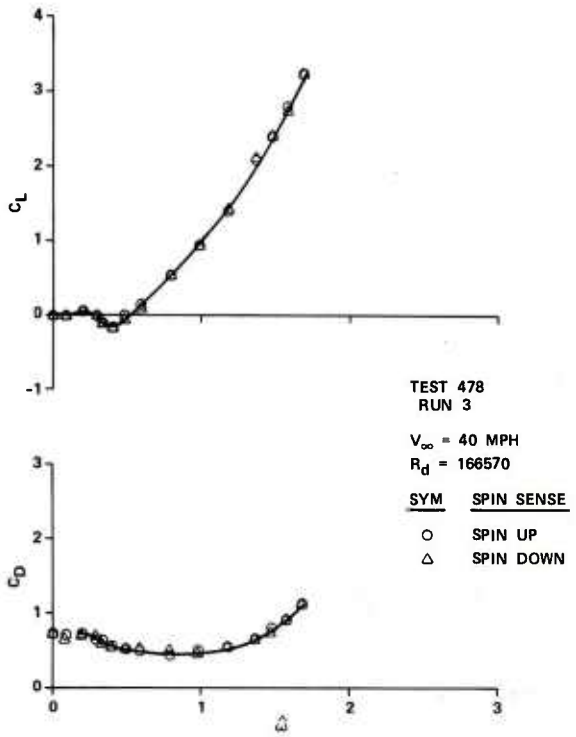

f. R_d = 166570

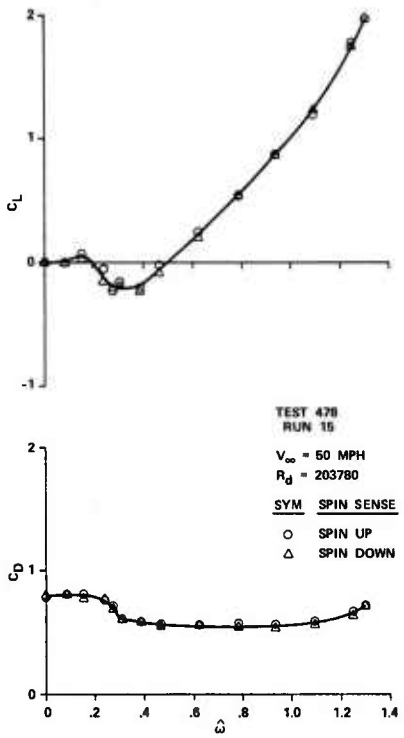

g. R_d = 203780

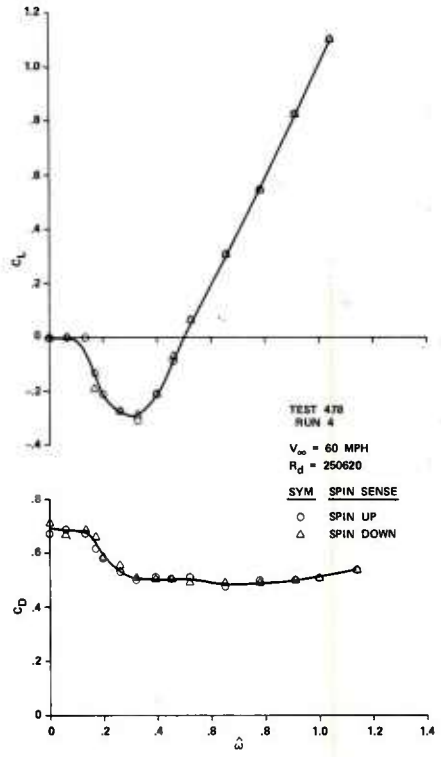

h. R_d = 250620

Figure A-15. (Contd)

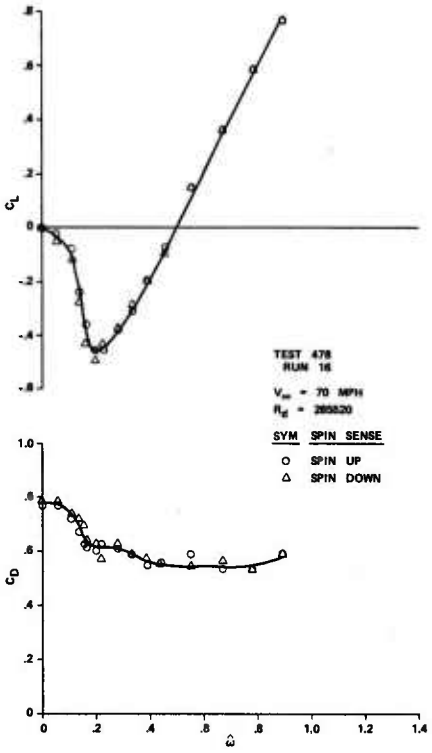

i. $R_d = 285520$

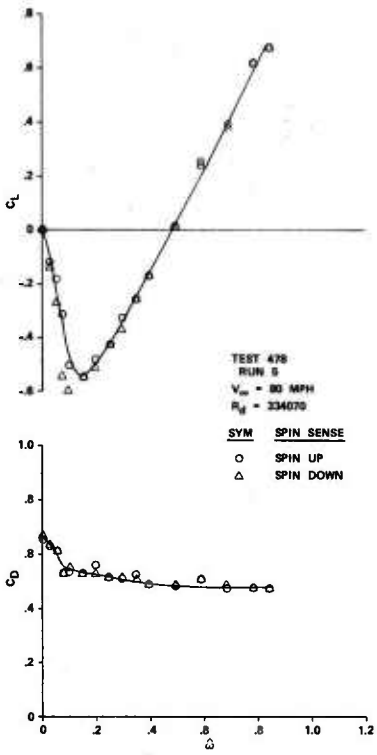

j. $R_d = 334070$

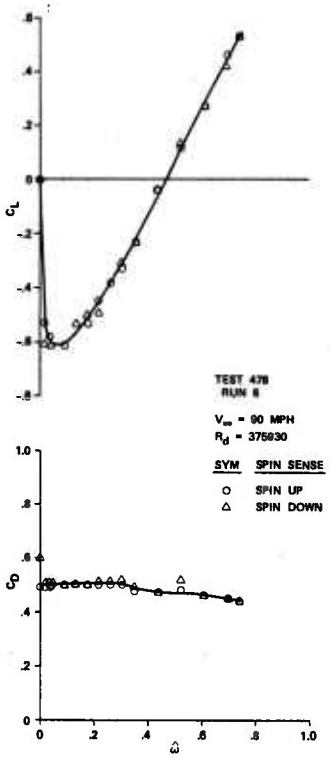

k. $R_d = 375930$

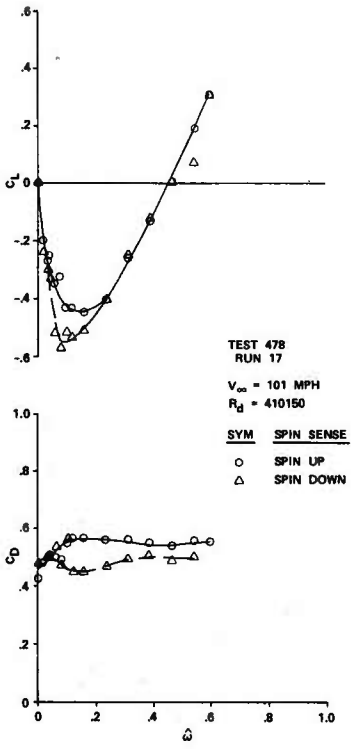

l. $R_d = 410150$

Figure A-15. (Contd)

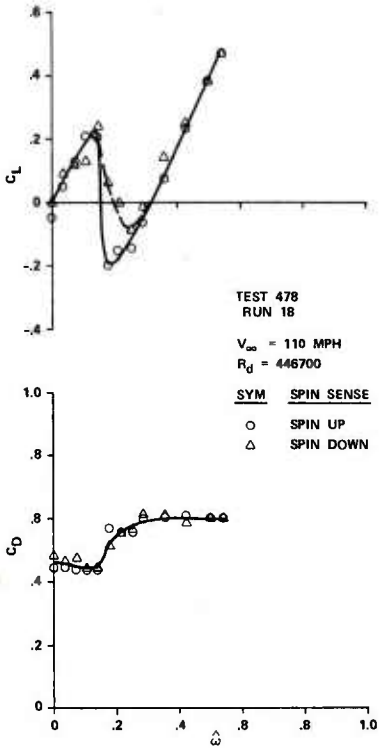

m. $R_d = 446700$

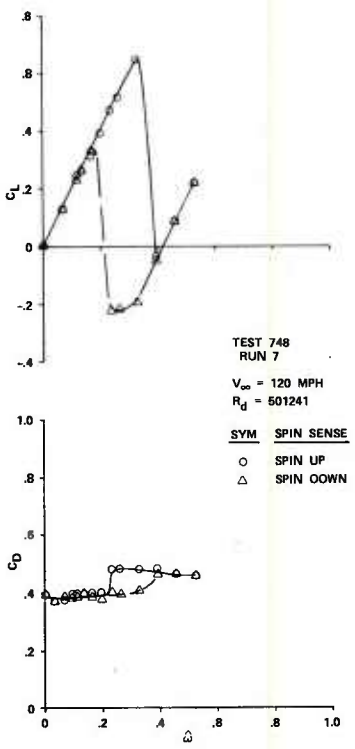

n. $R_d = 501241$

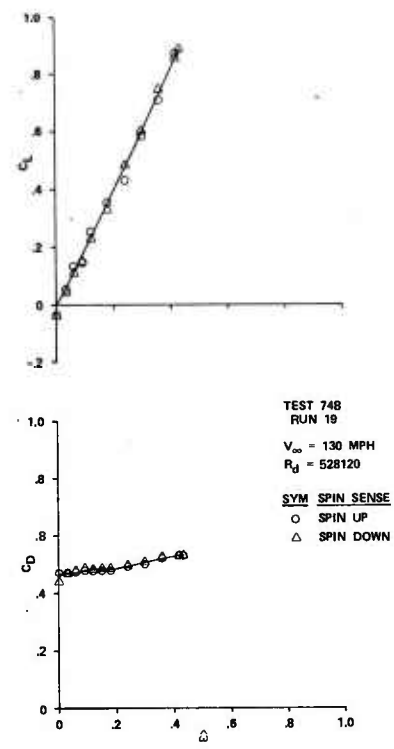

o. $R_d = 528120$

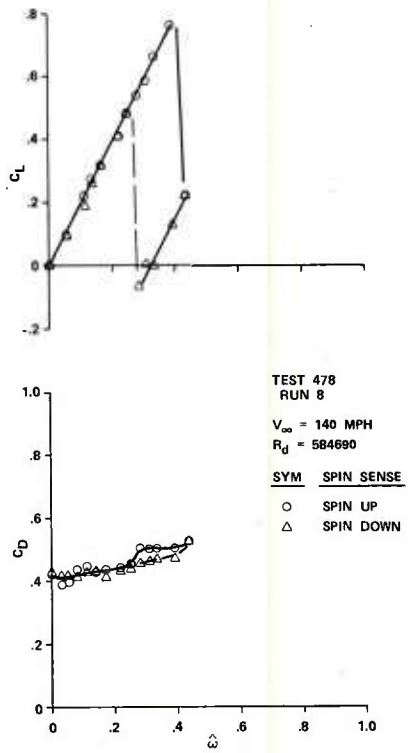

p. $R_d = 584690$

Figure A-15. (Contd)

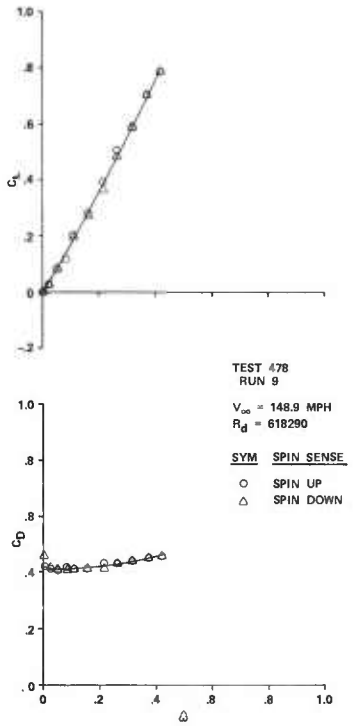

q. R_d = 618290

Figure A-15. (Contd)

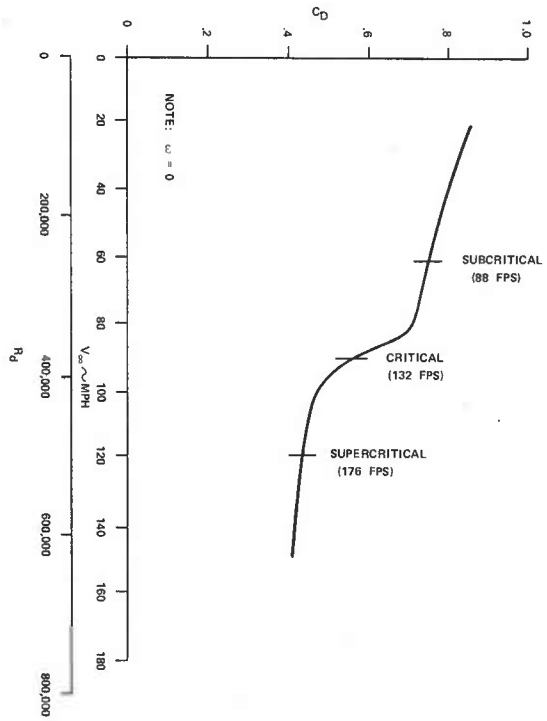

Figure A-16. Drag Coefficient Versus Free-Stream Velocity for the Nonspinning Cylinder

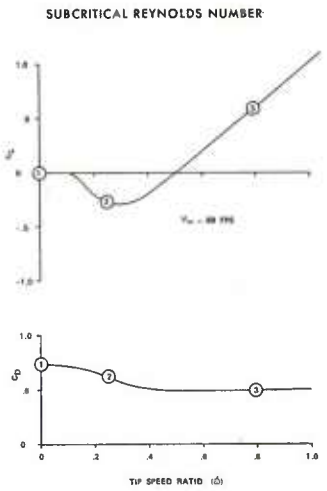

a. Subcritical Reynolds Number

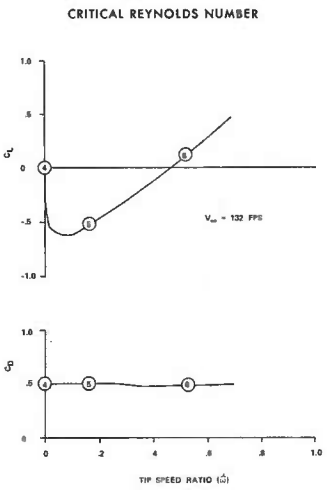

b. Critical Reynolds Number

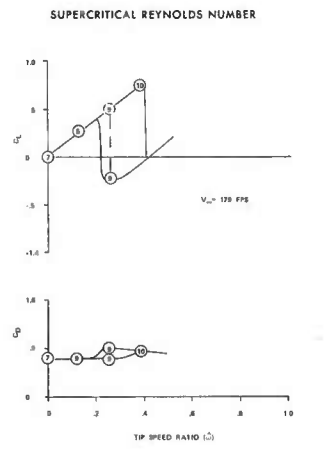

c. Supercritical Reynolds Number

Figure A-17. Summary of Test Conditions Selected for Pressure Surveys

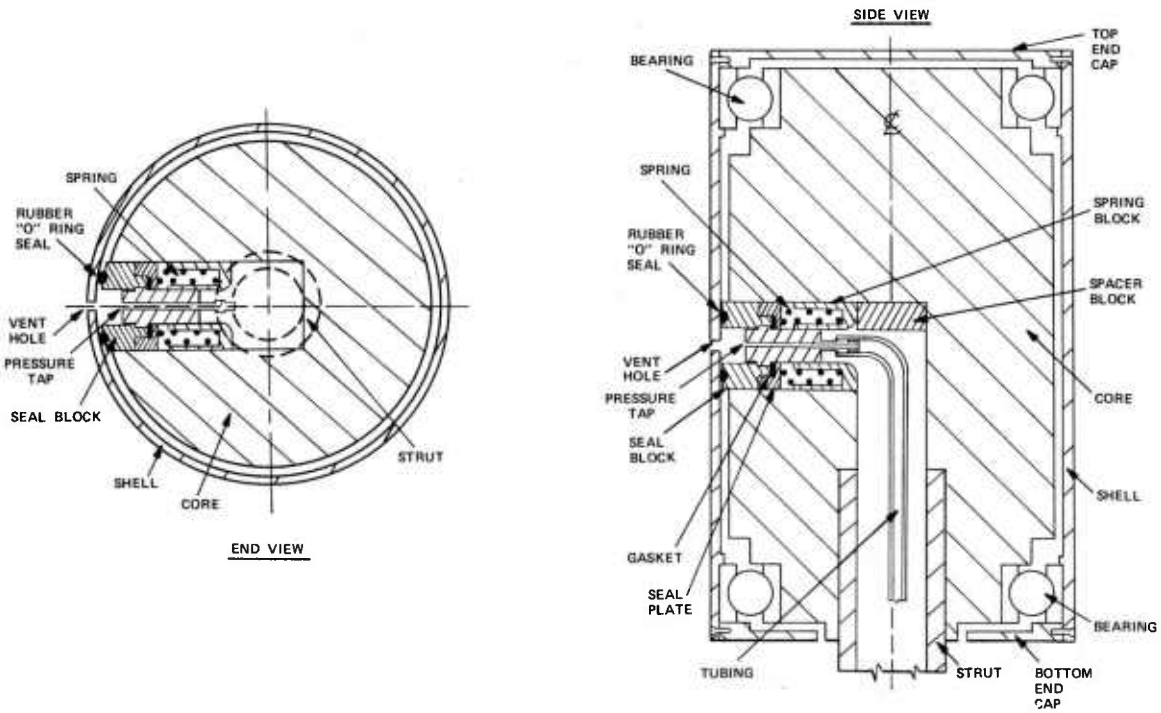

Figure A-18. Pressure Model, Internal Details

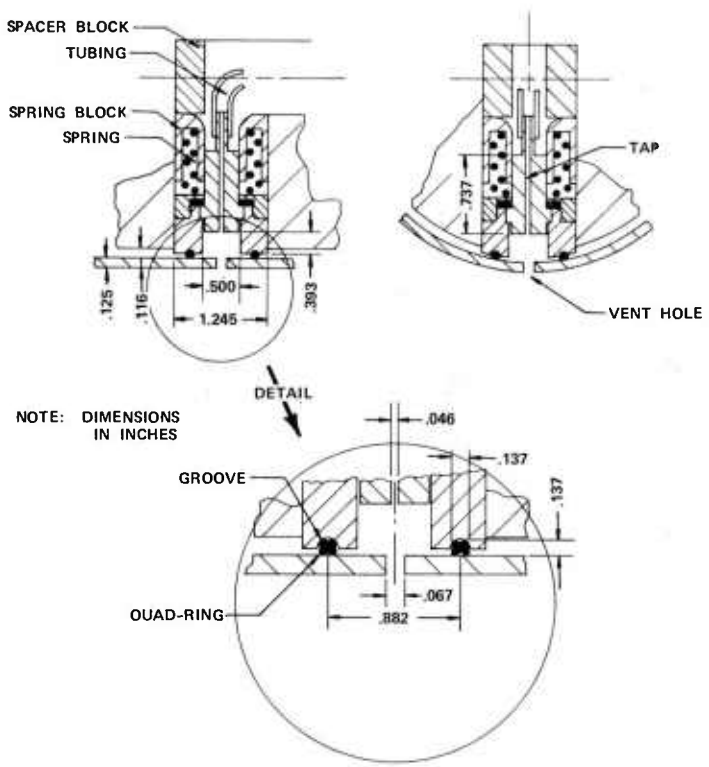

Figure A-19. Seal Details

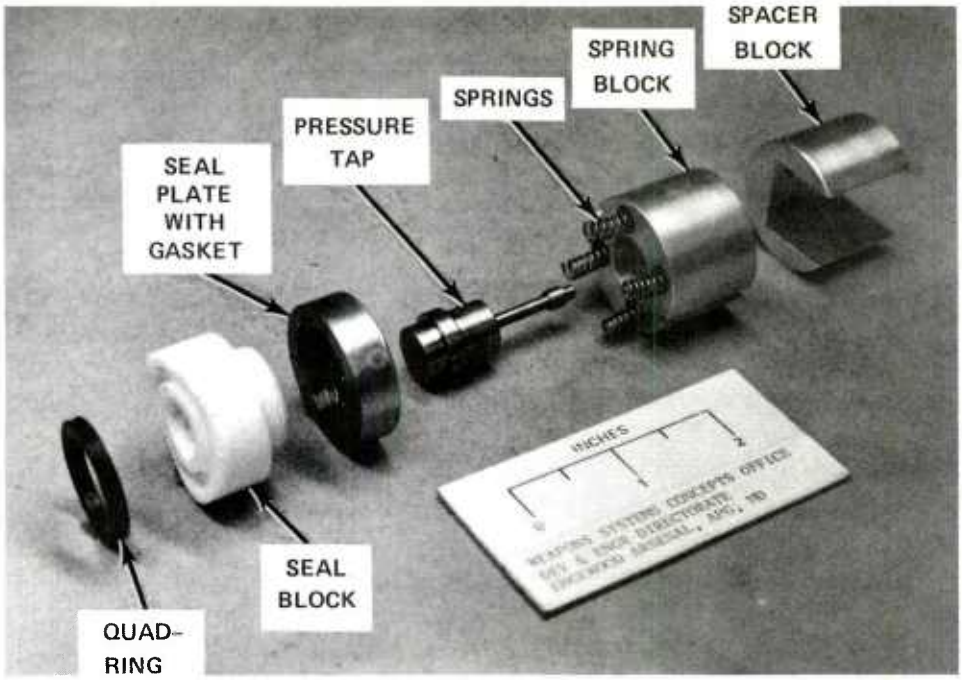

Figure A-20. Seal Assembly Components

a. Prior to Installation

b. Fully Installed

Figure A-21. Seal Installation Procedure

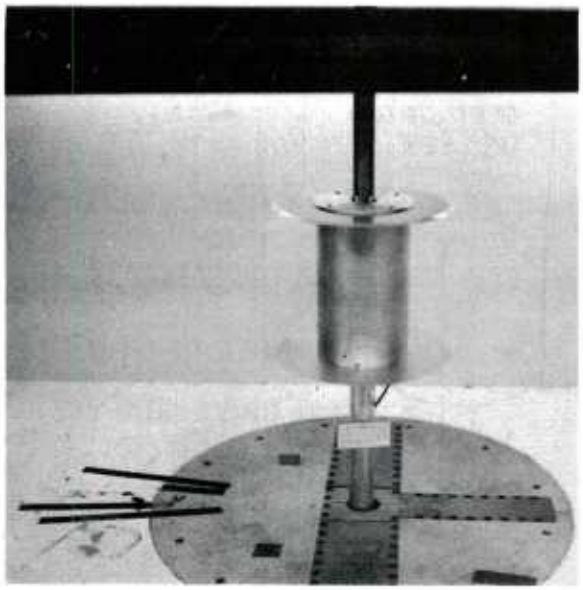

a. Viewed from Above

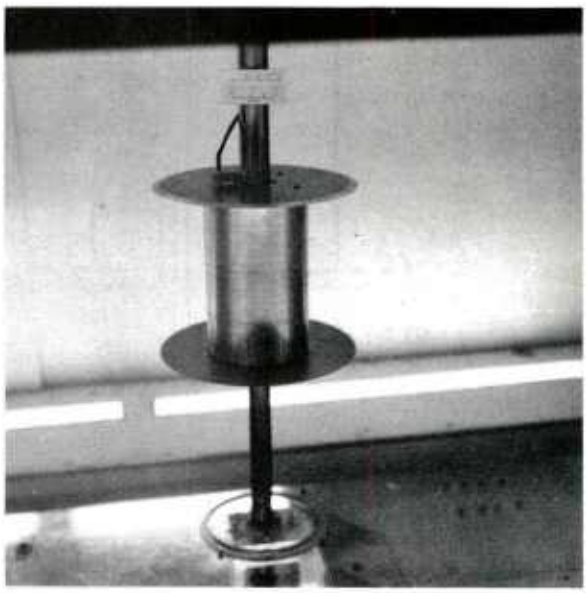

b. Viewed from Below

Figure A-22. Model Installed in Tunnel for Pressure Tests

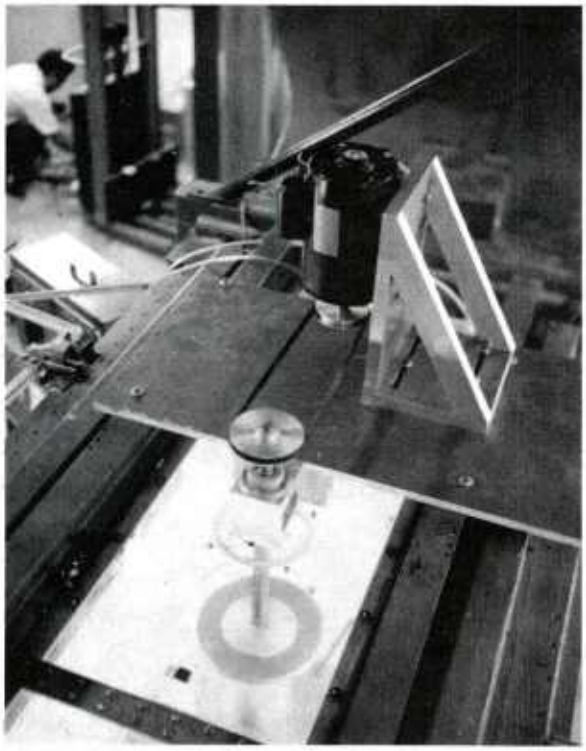

Figure A-23. Spin Motor Mounting Arrangement

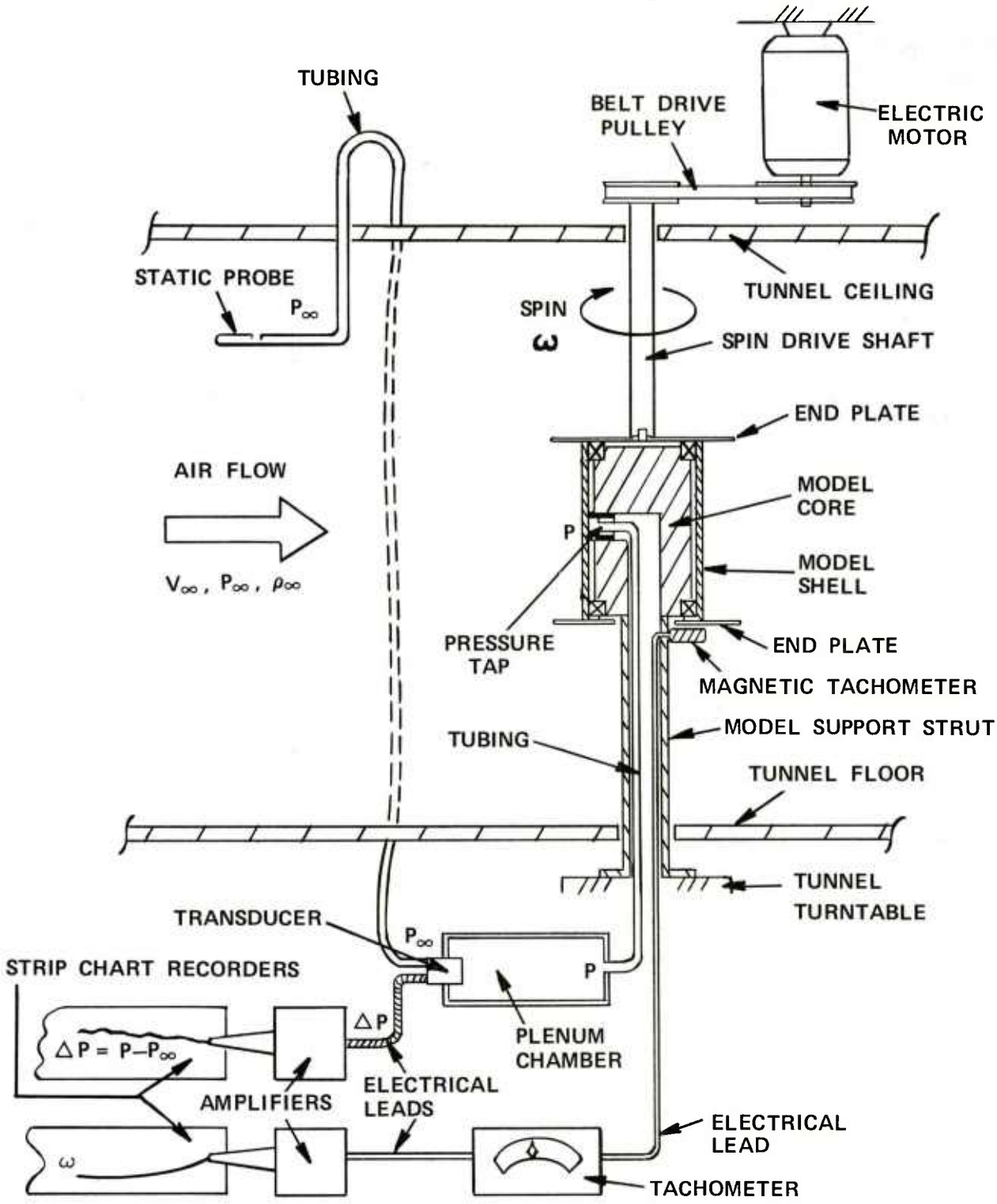

Figure A-24. Schematic of Tunnel Installation and Instrumentation Arrangement for Pressure Tests

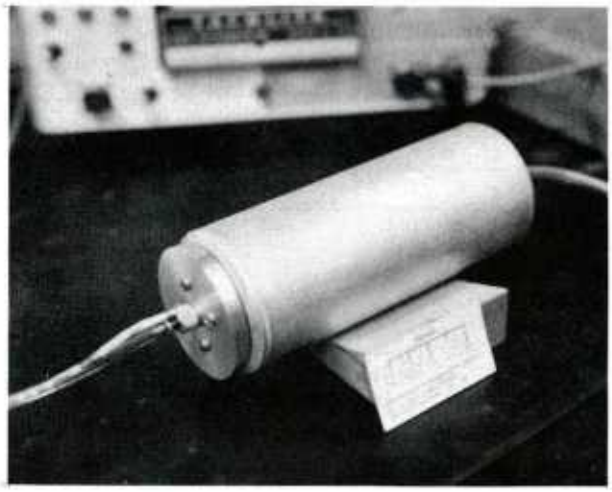

Figure A-25. Plenum Chamber

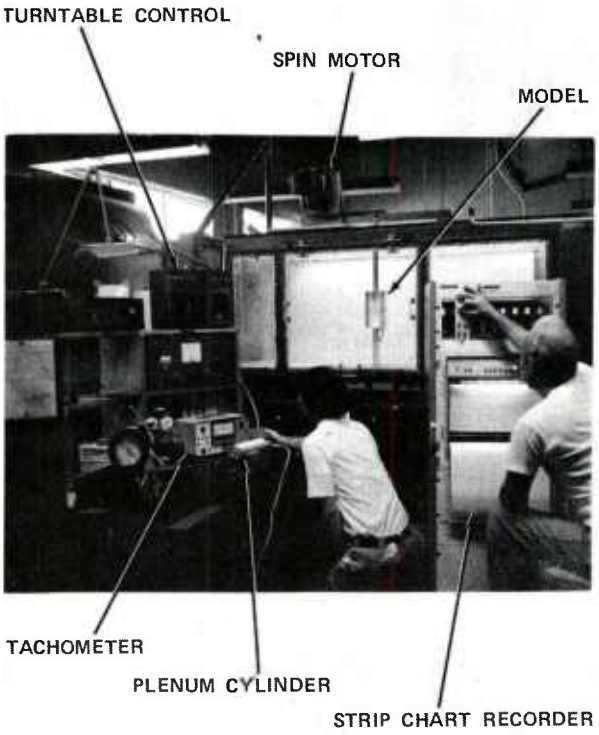

Figure A-26. Photograph of Pressure Test Setup

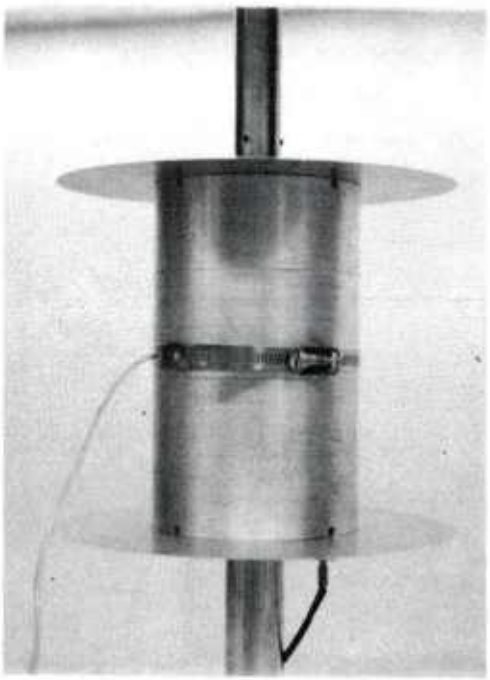

Figure A-27. Calibration Fixture for Pressure Model

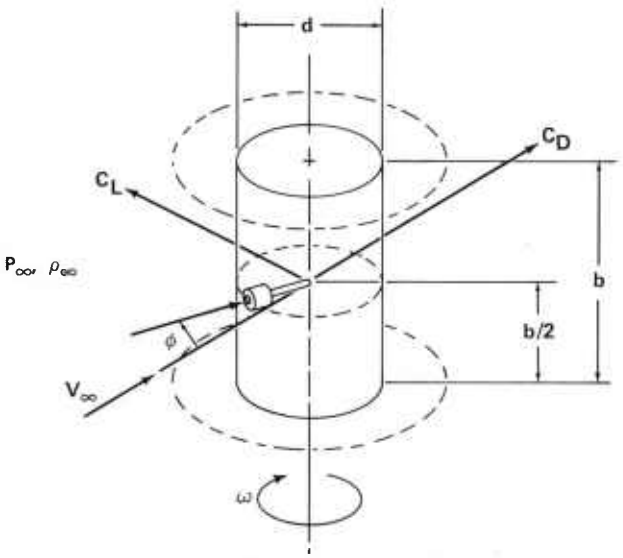

$$C_P = \frac{\Delta P}{q_\infty} \qquad \hat{\omega} = \frac{\omega d}{2V_\infty}$$

WHERE:

$$\Delta P = P - P_\infty$$

$$q_\infty = \frac{\rho_\infty V_\infty^2}{2}$$

Figure A-28. Definition of Pressure Test Terms

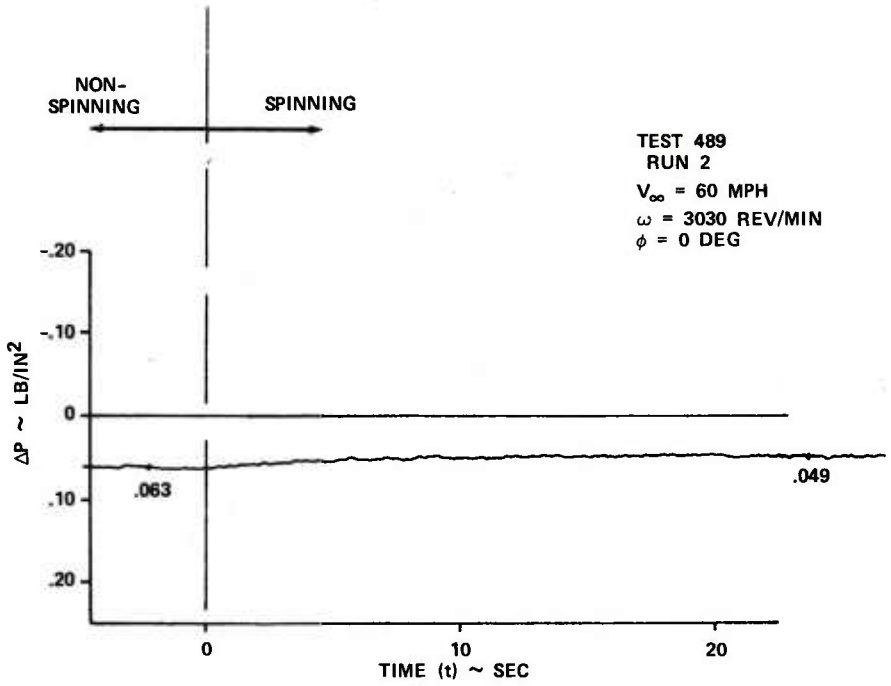

a. $\phi = 0$ (Positive Pressure Region)

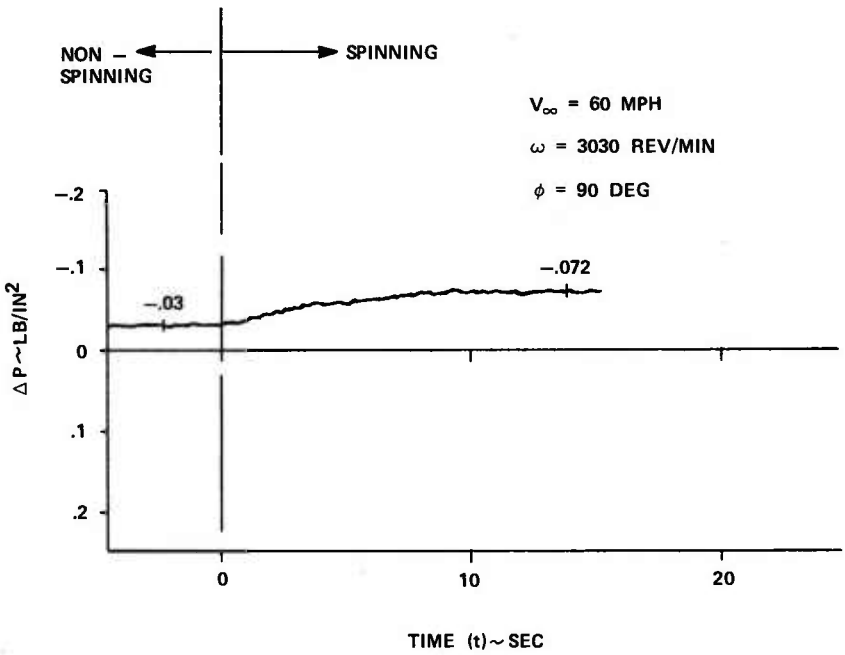

b. $\phi = 90^\circ$ (Negative Pressure Region)

Figure A-29. Typical Pressure Data Trace Showing Effect of Spin

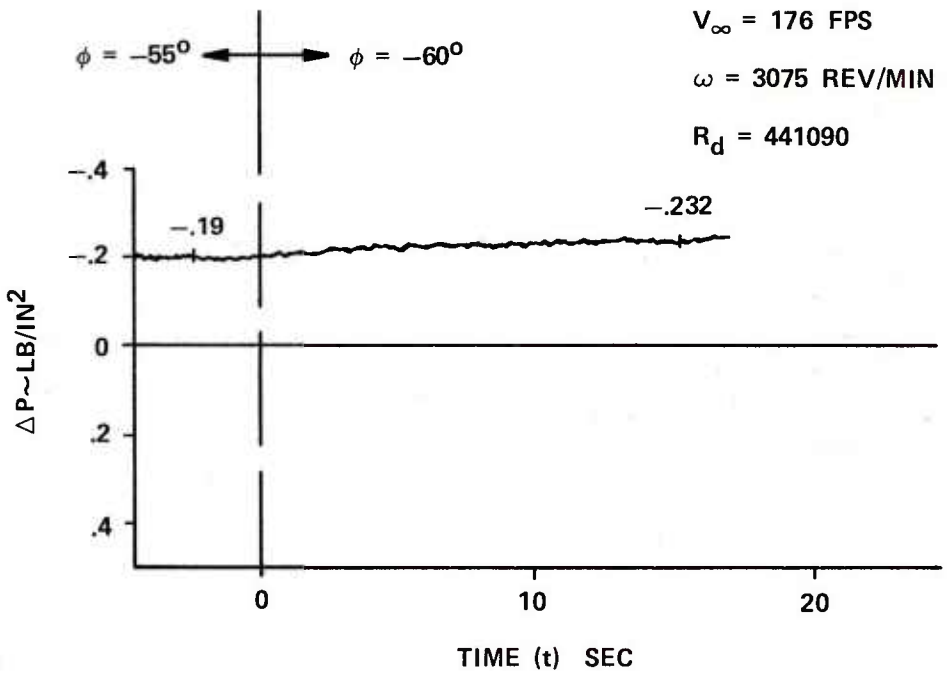

Figure A-30. Typical Pressure Data Trace Showing Effect of Circumferential Location

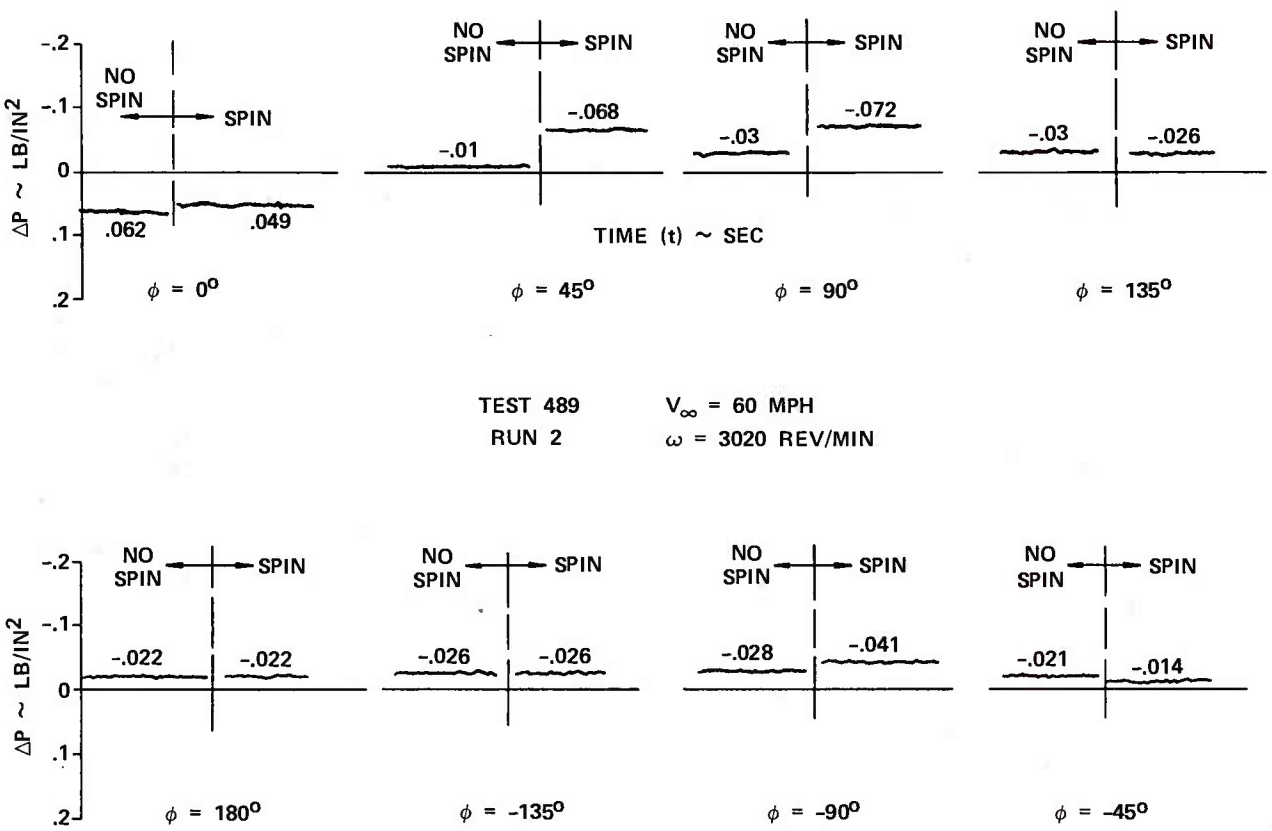

Figure A-31. Representative Pressure Data Obtained at Several Circumferential Locations

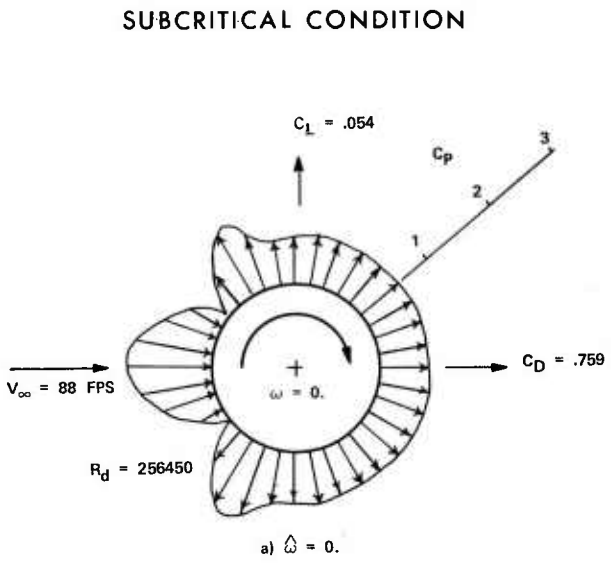

Figure A-32. Surface Pressure Distribution Obtained at Subcritical Reynolds Number, $\hat{\omega} = 0$ (Case 1)

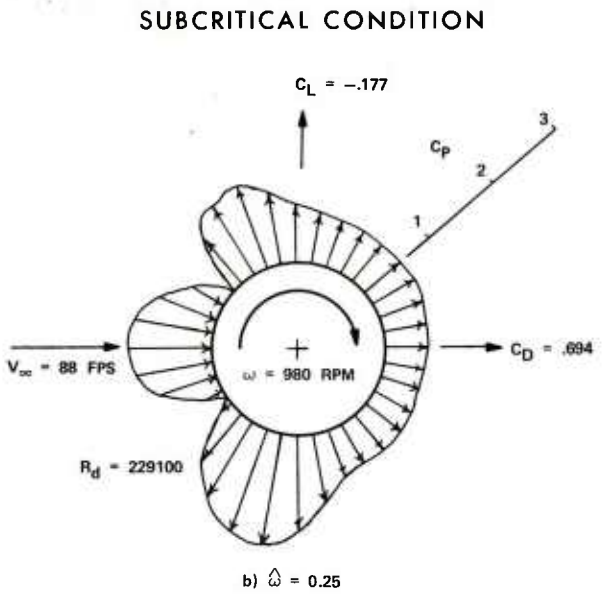

Figure A-33. Surface Pressure Distribution Obtained at Subcritical Reynolds Number, $\hat{\omega} = 0.25$ (Case 2)

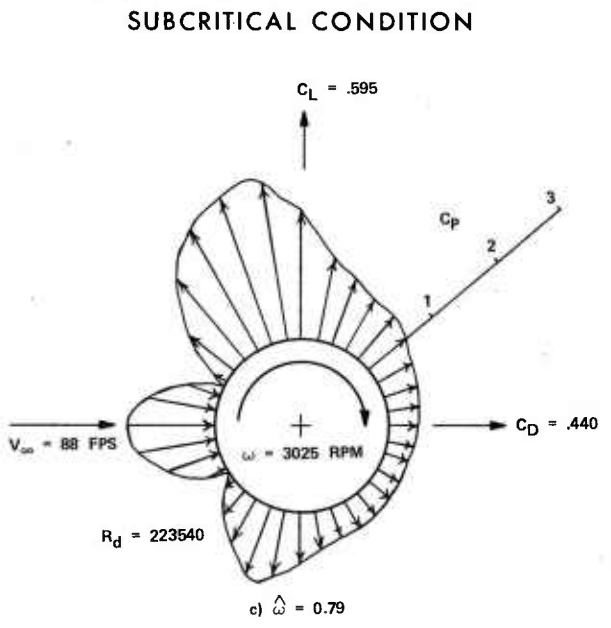

Figure A-34. Surface Pressure Distribution Obtained at Subcritical Reynolds Number, $\hat{\omega} = 0.79$ (Case 3)

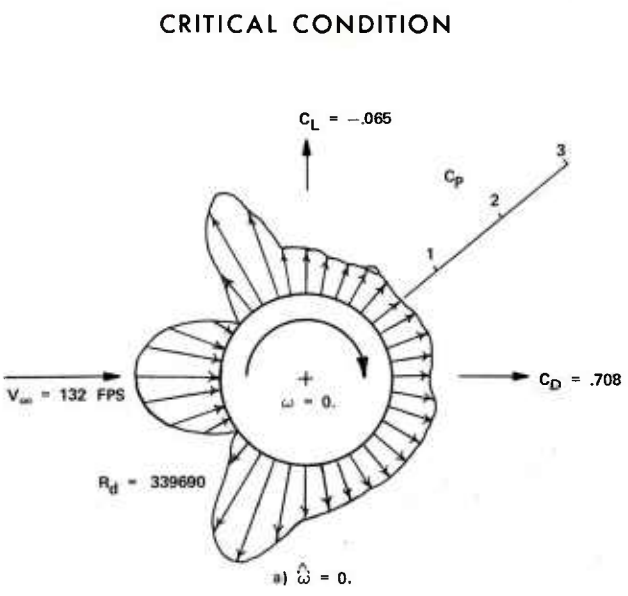

Figure A-35. Surface Pressure Distribution Obtained at Critical Reynolds Number, $\hat{\omega} = 0$ (Case 4)

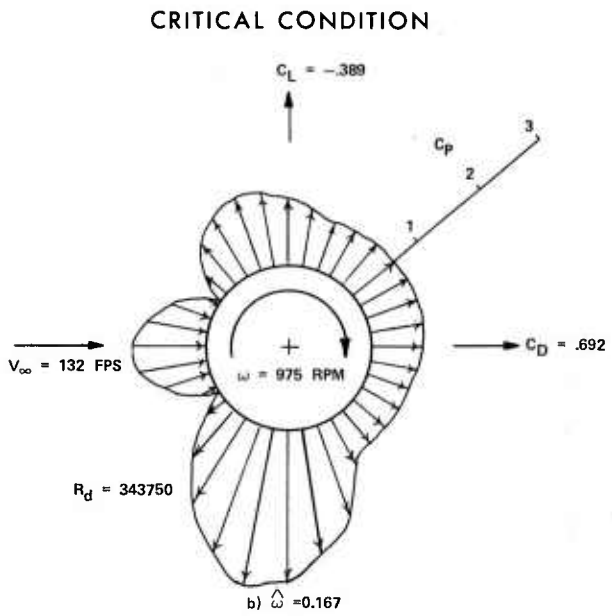

Figure A-36. Surface Pressure Distribution Obtained at Critical Reynolds Number, $\hat{\omega} = 0.167$ (Case 5)

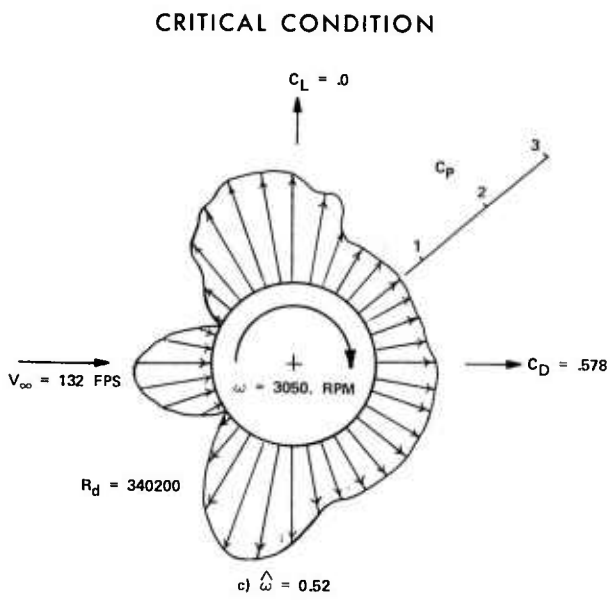

Figure A-37. Surface Pressure Distribution Obtained at Critical Reynolds Number, $\hat{\omega} = 0.52$ (Case 6)

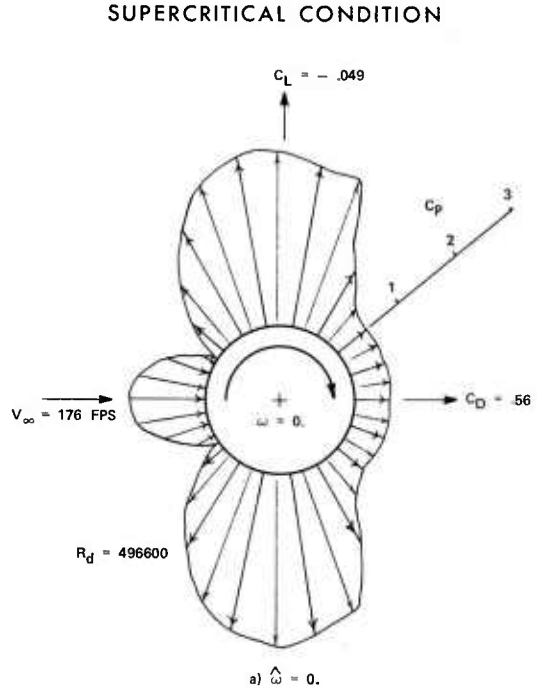

Figure A-38. Surface Pressure Distribution Obtained at Supercritical Reynolds Number, $\hat{\omega} = 0$ (Case 7)

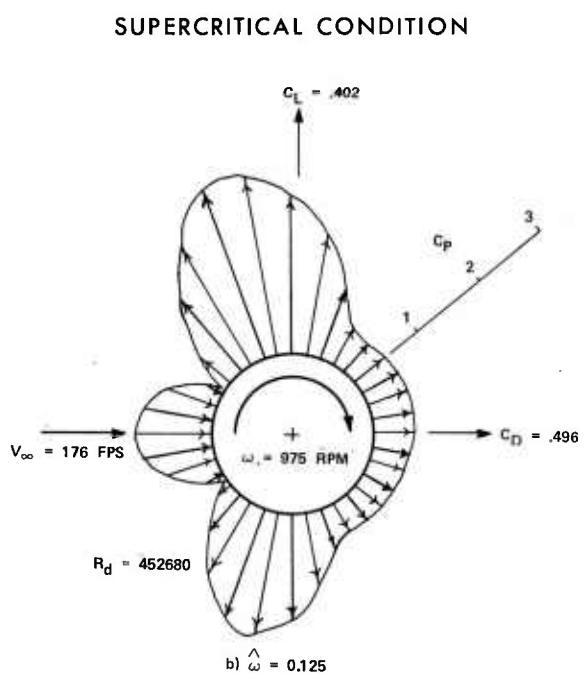

Figure A-39. Surface Pressure Distribution Obtained at Supercritical Reynolds Number, $\hat{\omega} = 0.125$ (Case 8)

SUPERCRITICAL CONDITION

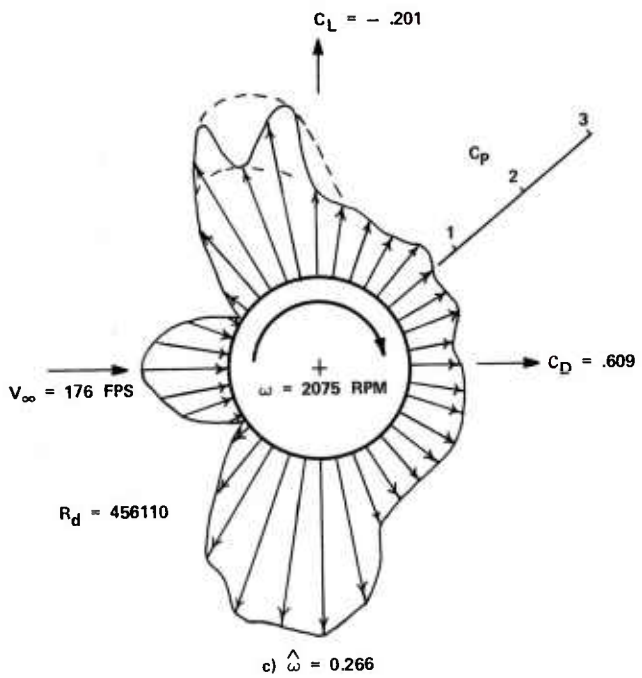

Figure A-40. Surface Pressure Distribution Obtained at Supercritical Reynolds Number, $\hat{\omega}$ = 0.26 (Case 9)

SUPERCRITICAL CONDITION

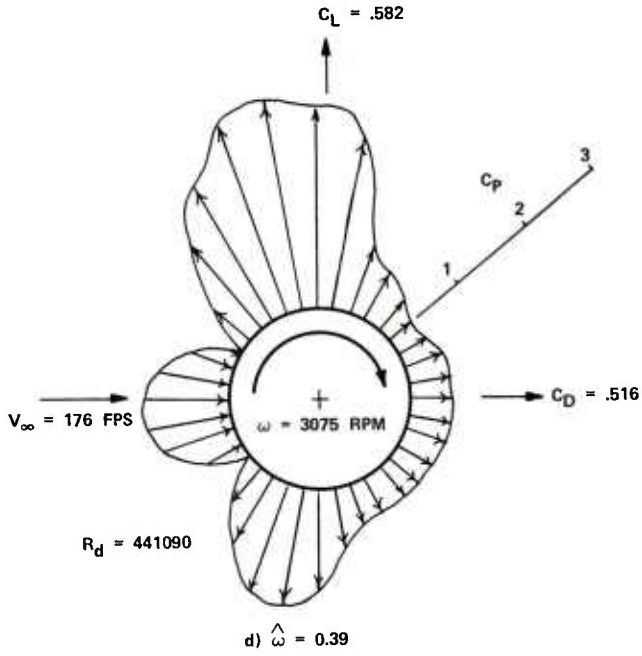

Figure A-41. Surface Pressure Distribution Obtained at Supercritical Reynolds Number, $\hat{\omega}$ = 0.39 (Case 10)

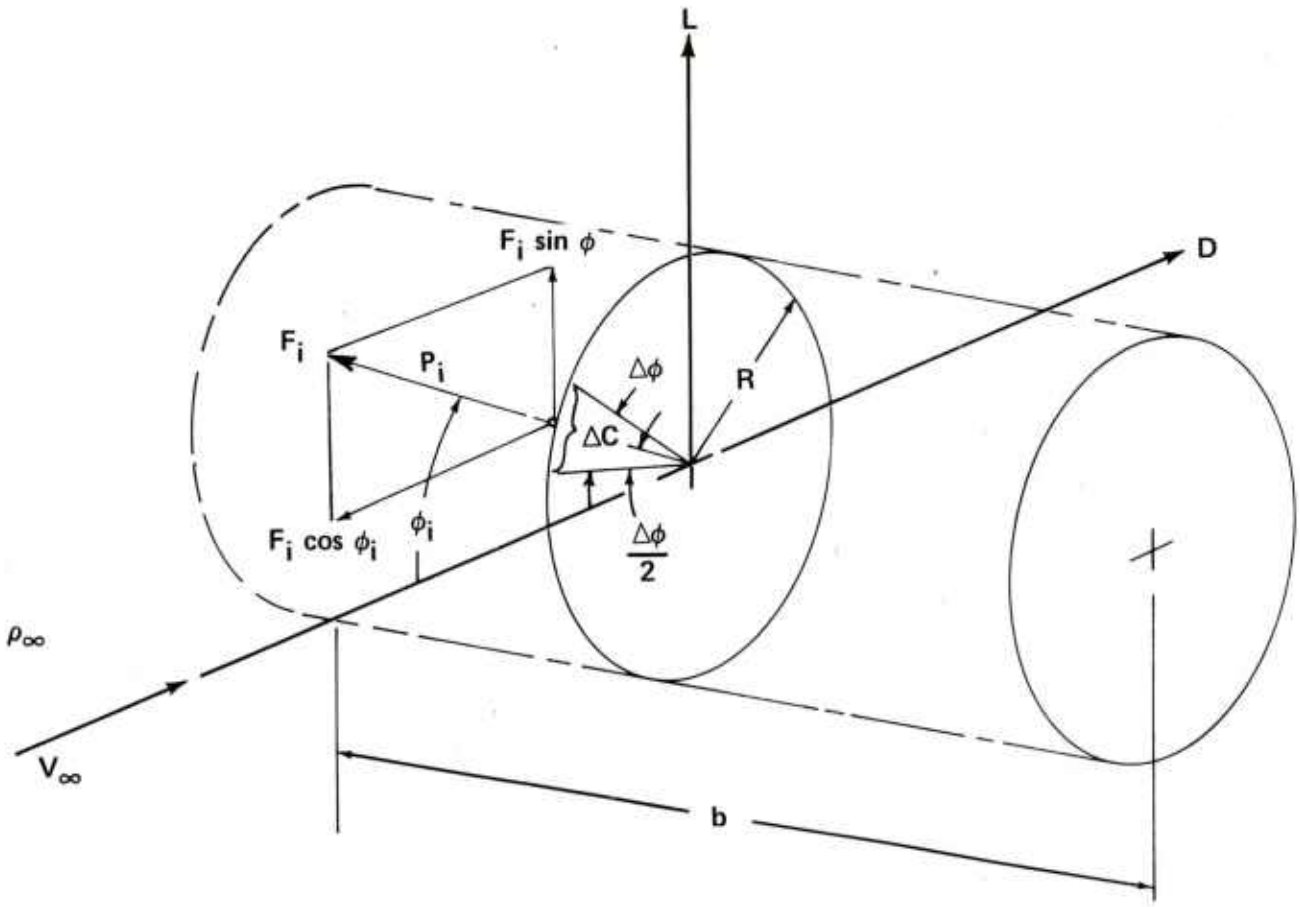

LIFT COEFFICIENT

$$L_i = F_i \sin \phi_i \, b$$

DRAG COEFFICIENT

$$D_i = F_i \cos \phi_i \, b$$

$$F_i = P_i \, \Delta C R$$

$$\Delta C = R \sin \Delta\phi$$

$$\therefore F_i = P_i \, R \sin \Delta\phi \, b$$

$$L_i = P_i \, R \sin \phi_i \sin \Delta\phi \, b \qquad D_i = P_i \, R \cos \phi_i \sin \Delta\phi \, b$$

let $\Delta\phi = 5^o$

THIS DETERMINES THE NUMBER AT PRESSURE MEASUREMENT LOCATIONS AS 360/5 = 72

$$L = b \, R \sin \Delta\phi \sum_{i=1}^{72} (P_i \sin \phi_i) \qquad D = b \, R \sin \Delta\phi \sum_{i=1}^{72} (P_i \cos \phi_i)$$

$$C_L = \frac{L}{q_\infty S} \qquad C_D = \frac{D}{q_\infty S}$$

$$S = 2R \, b$$

$$P_i = C_{P_i} \, q_\infty$$

$$C_L = \frac{\sin \Delta\phi}{2} \sum_{i=1}^{72} C_{P_i} \sin \phi_i \qquad C_D = \frac{\sin \Delta\phi}{2} \sum_{i=1}^{72} C_{P_i} \cos \phi_i$$

Figure A-42. Derivation of Pressure Integration Equations

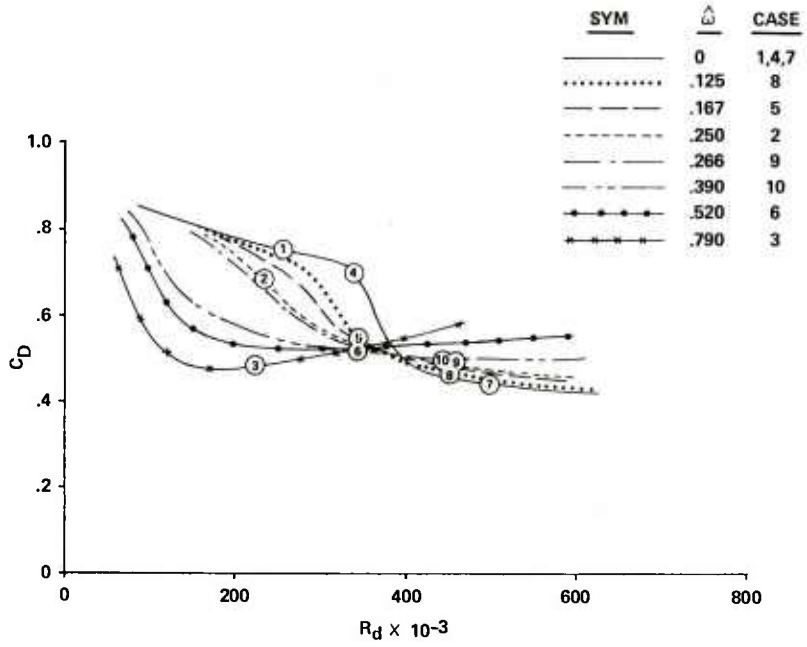

a. Lift

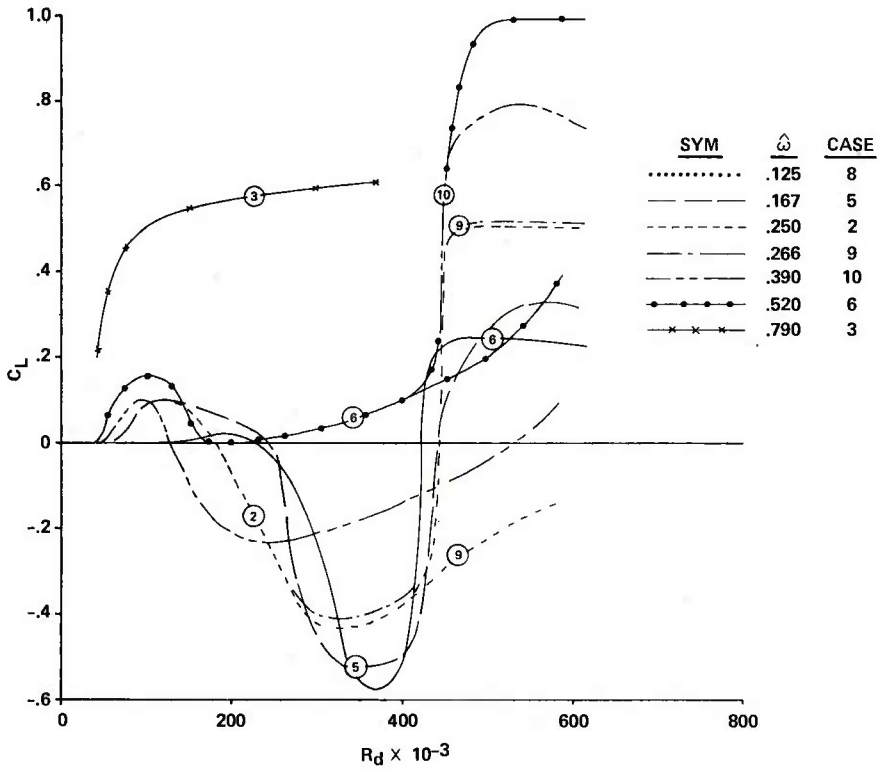

b. Drag

Figure A-43. Lift and Drag Coefficients as a Function of Reynolds Number for Constant Tip Speed Ratio Values as Determined from Wind-Tunnel Force Tests

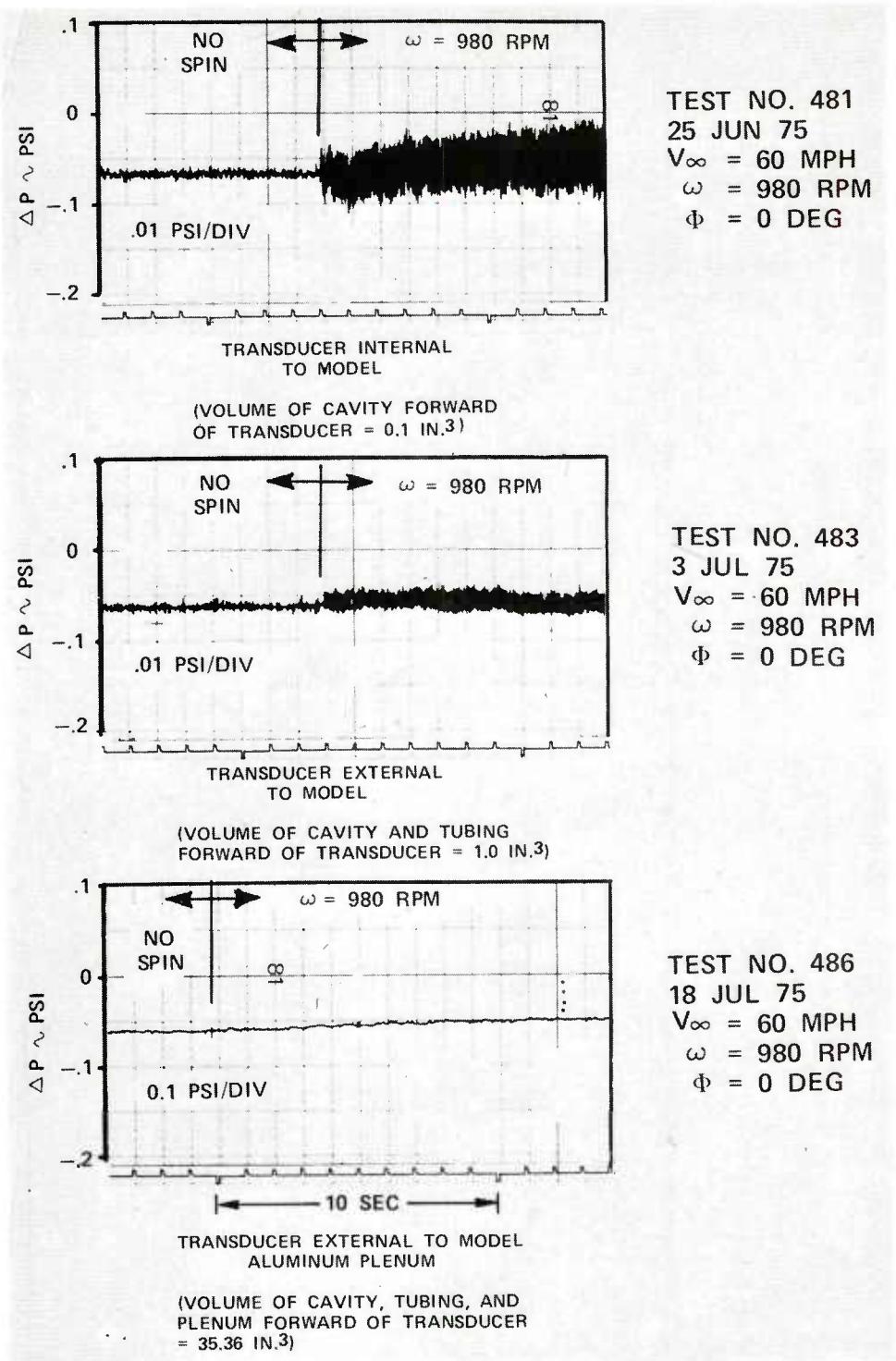

Figure A-44. Effect of Transducer Location and Volume Forward of Transducer

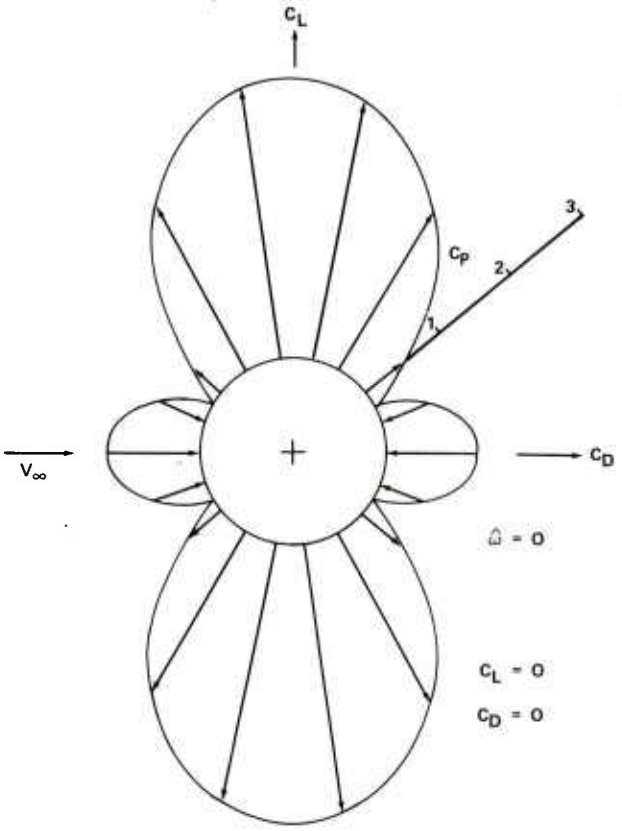

Figure A-45. Surface Pressure Distribution on Nonspinning Cylinder as Computed Using Simple Potential Flow Theory

a. Flow Over Flat Plate

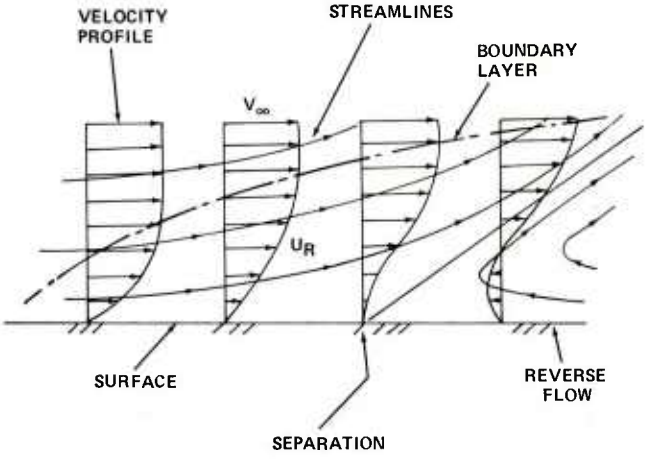

b. Boundary Layer Details

Figure A-46. Boundary Layer Characteristics

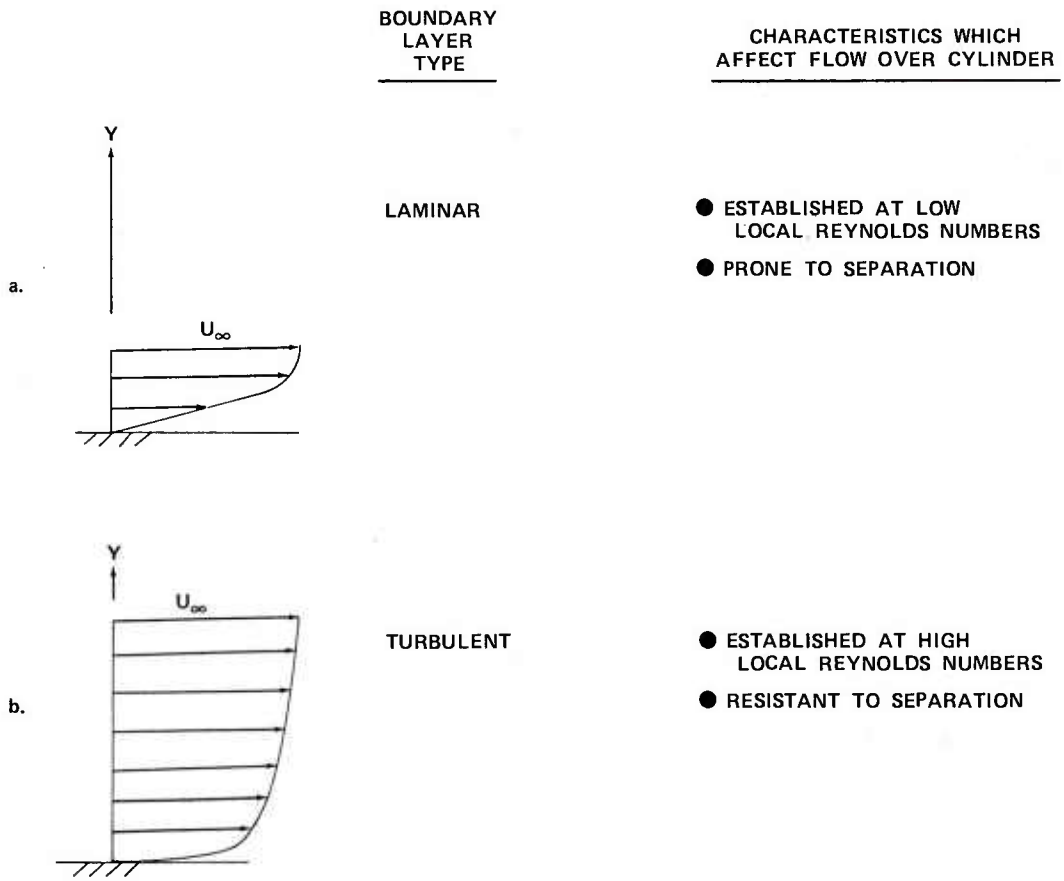

Figure A-47. Effect of Boundary Layer on Flow Over Cylinder

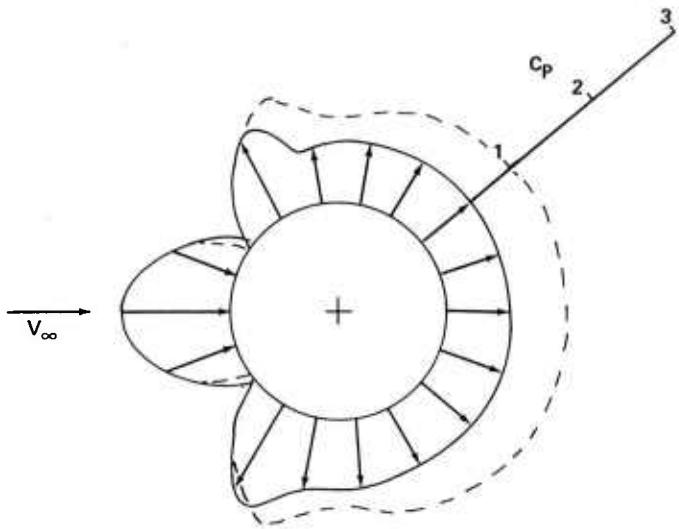

SYM	R_d	SOURCE
———	256450	TEST 461
- - - - - -	186000	SCHLICHTING

Figure A-48. Typical Subcritical Pressure Distribution on Nonspinning Cylinder

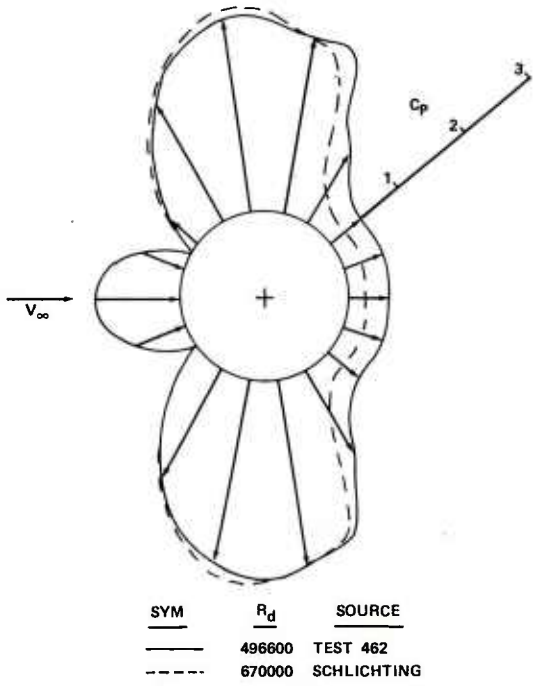

Figure A-49. Typical Supercritical Pressure Distribution on Nonspinning Cylinder

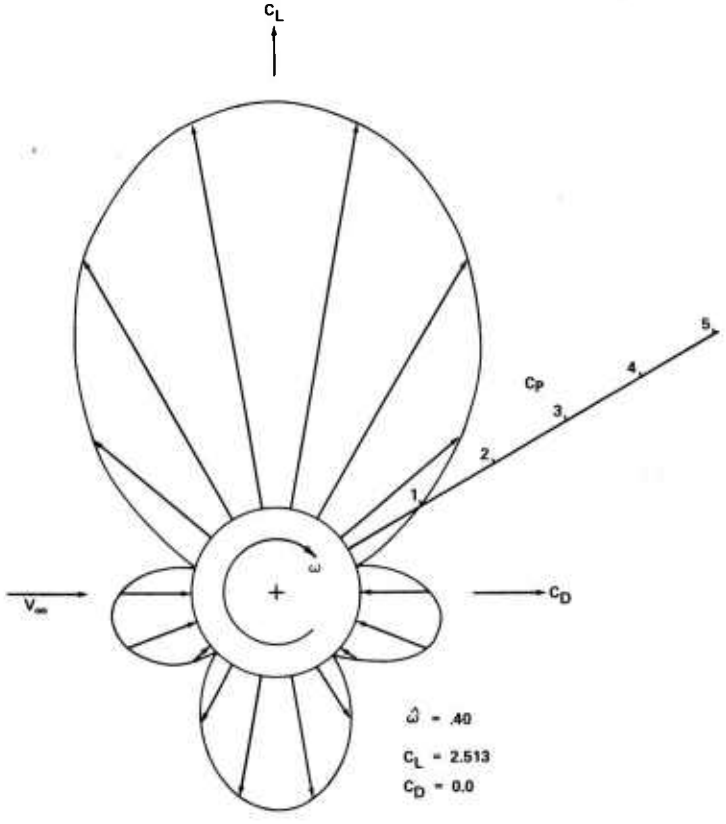

Figure A-50. Surface Pressure Distribution on Spinning Cylinder as Computed Using Simple Potential Flow Theory

	SURFACE MOTION	CHARACTERISTICS WHICH AFFECT FLOW OVER CYLINDER
a.	SAME DIRECTIONAL SENSE AS LOCAL FREE STREAM	● REDUCES LOCAL REYNOLDS NUMBER ● REDUCES TENDENCY OF BOUNDARY LAYER TO SEPARATE
b.	OPPOSITE DIRECTIONAL SENSE AS LOCAL FREE STREAM	● INCREASES LOCAL REYNOLDS NUMBER ● INCREASES TENDENCY OF BOUNDARY LAYER TO SEPARATE

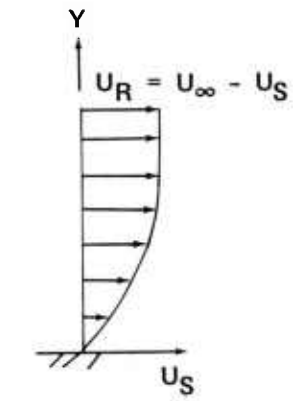

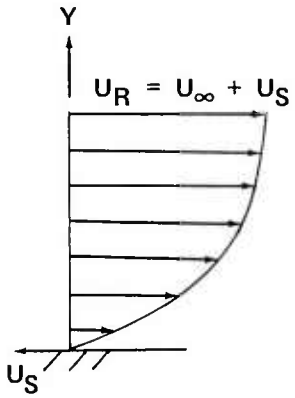

Figure A-51. Effect of Surface Motion on Flow Over Cylinder

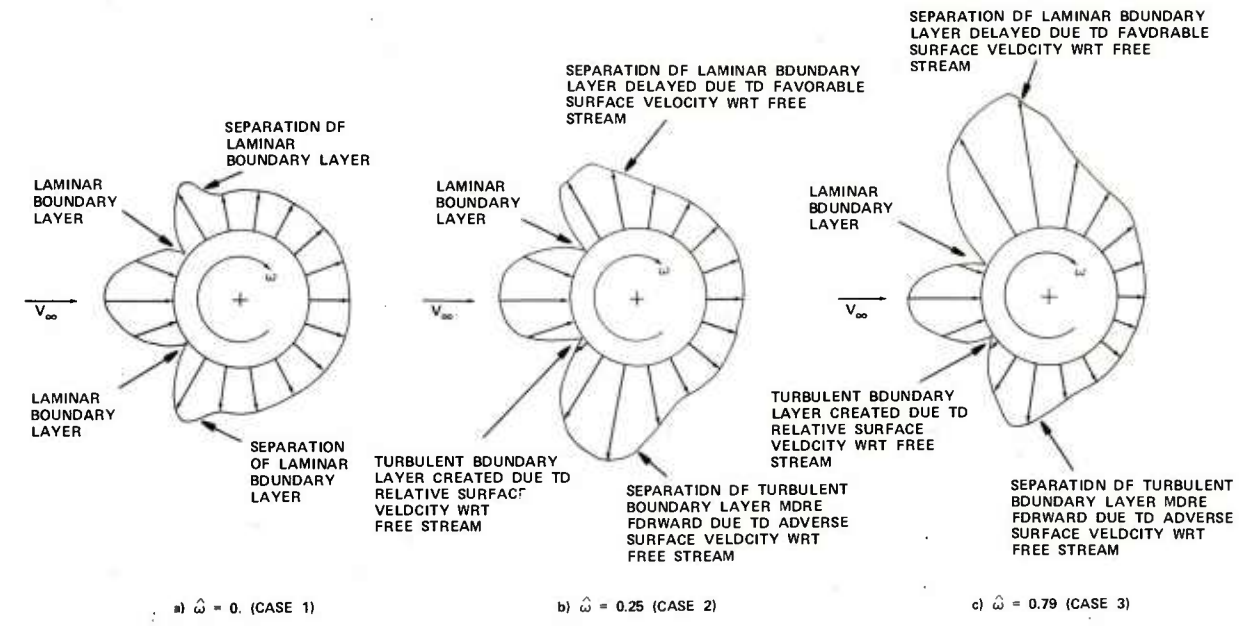

Figure A-52. Effect of Tip Speed Ratio on Pressure Distribution at Subcritical Reynolds Number Test Condition

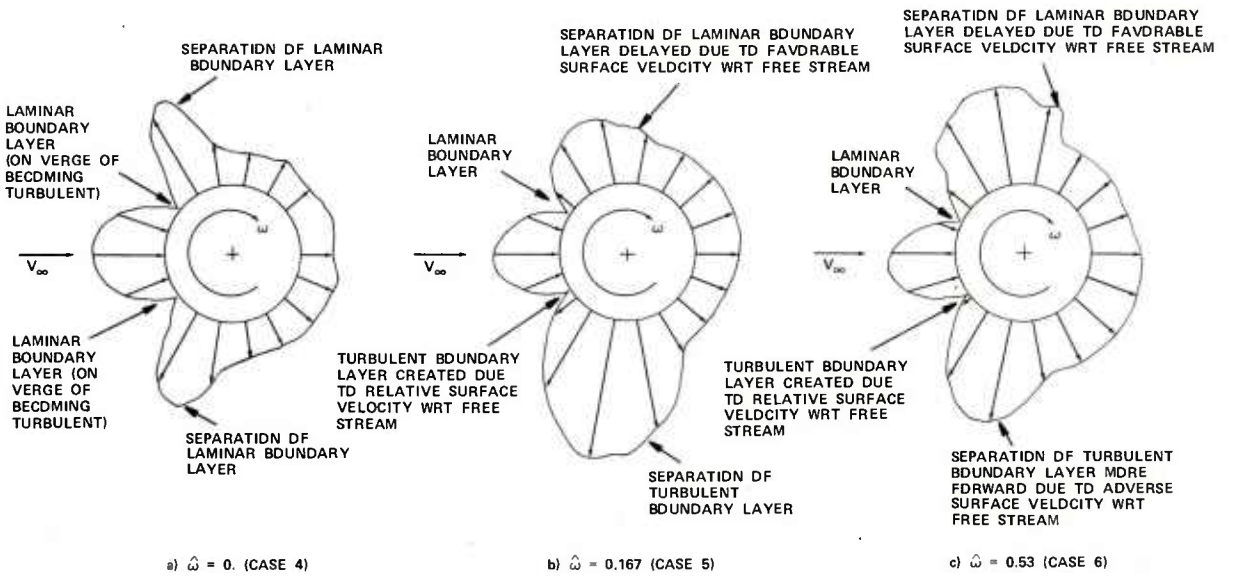

Figure A-53. Effect of Tip Speed Ratio on Pressure Distribution at Critical Reynolds Number Test Condition

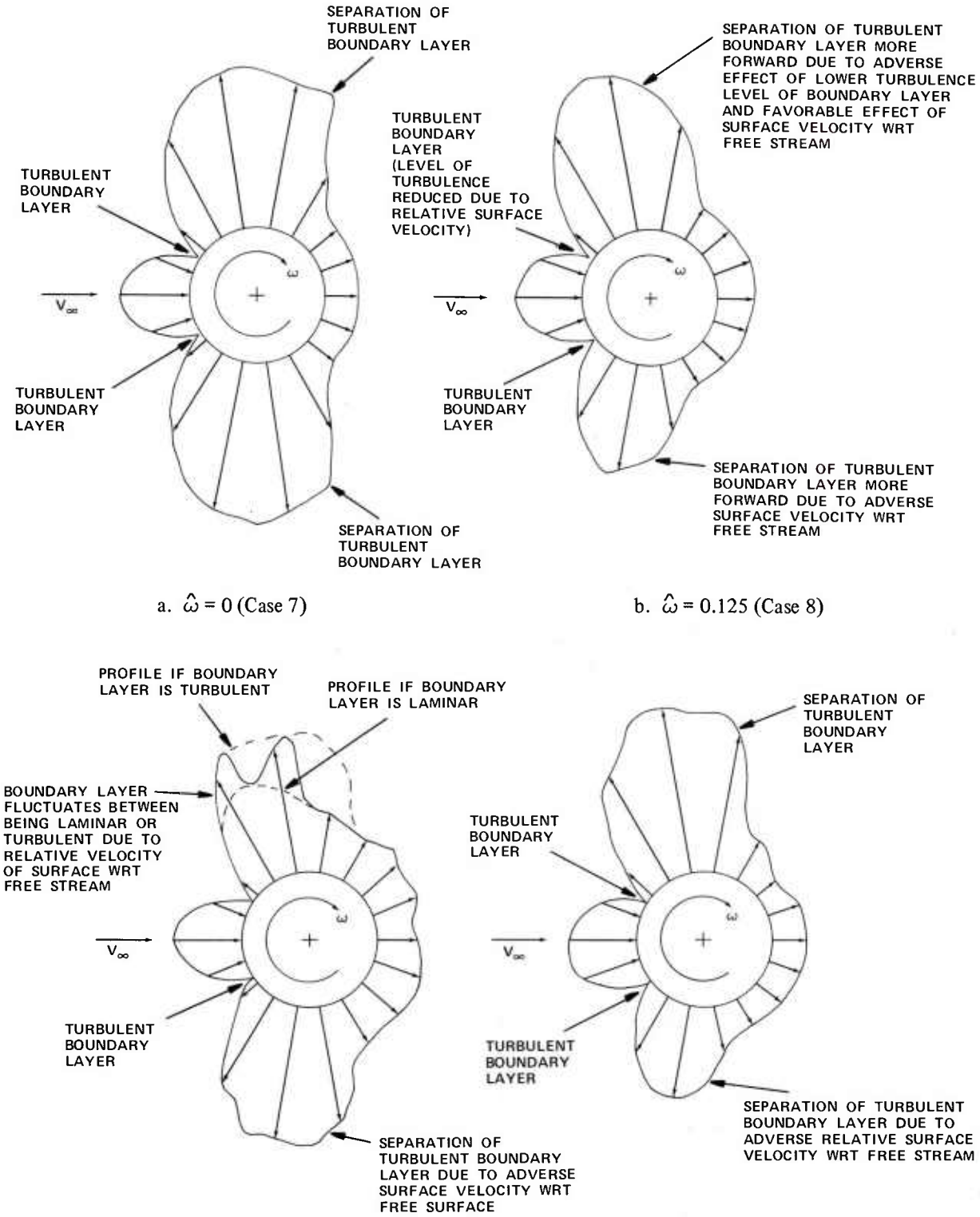

Figure A-54. Effect of Tip Speed Ratio on Pressure Distribution at Supercritical Reynolds Number Test Condition

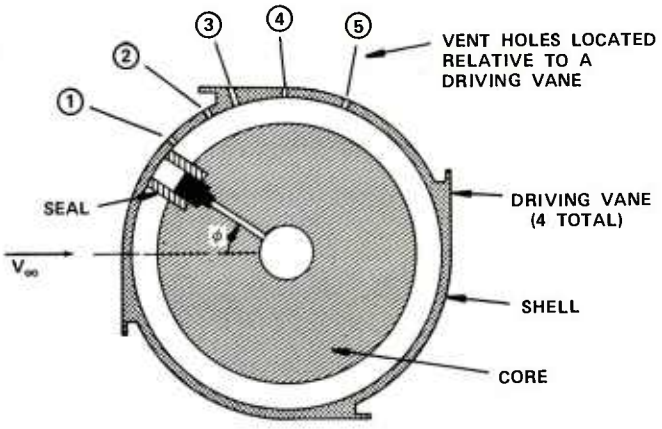

Figure A-55. Schematic of Autorotor Model

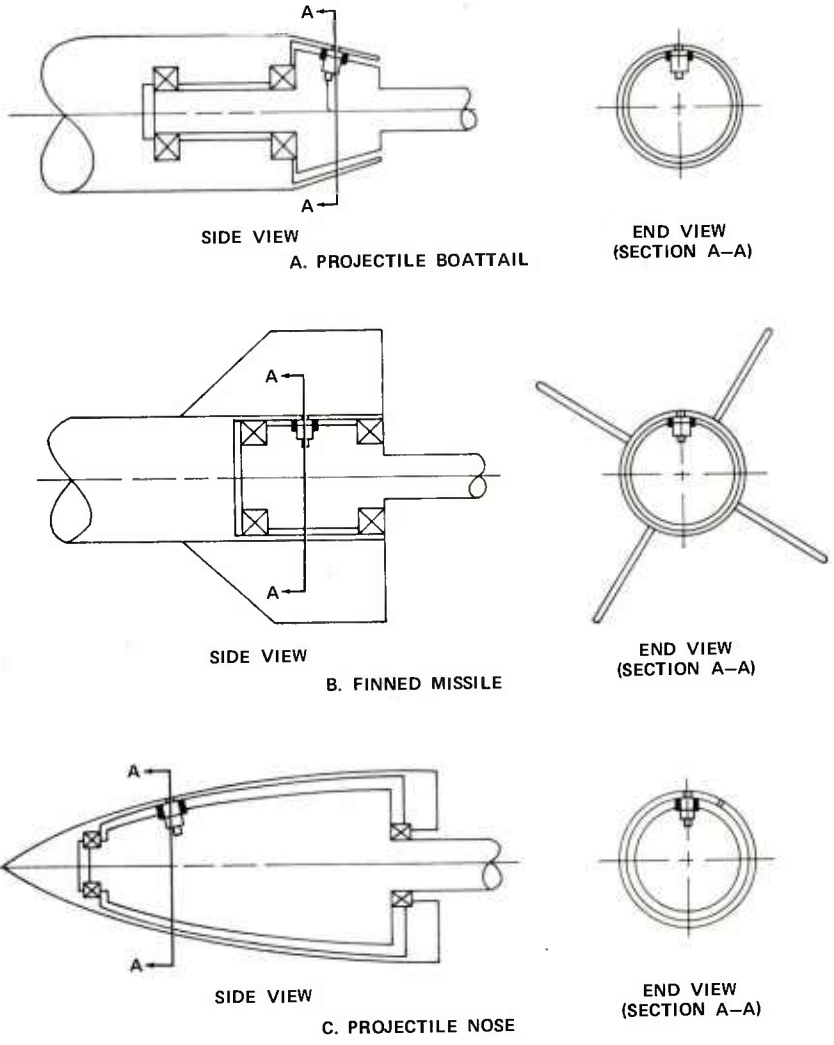

Figure A-56. Instrumentation Technique Applied to Various Projectile Configurations

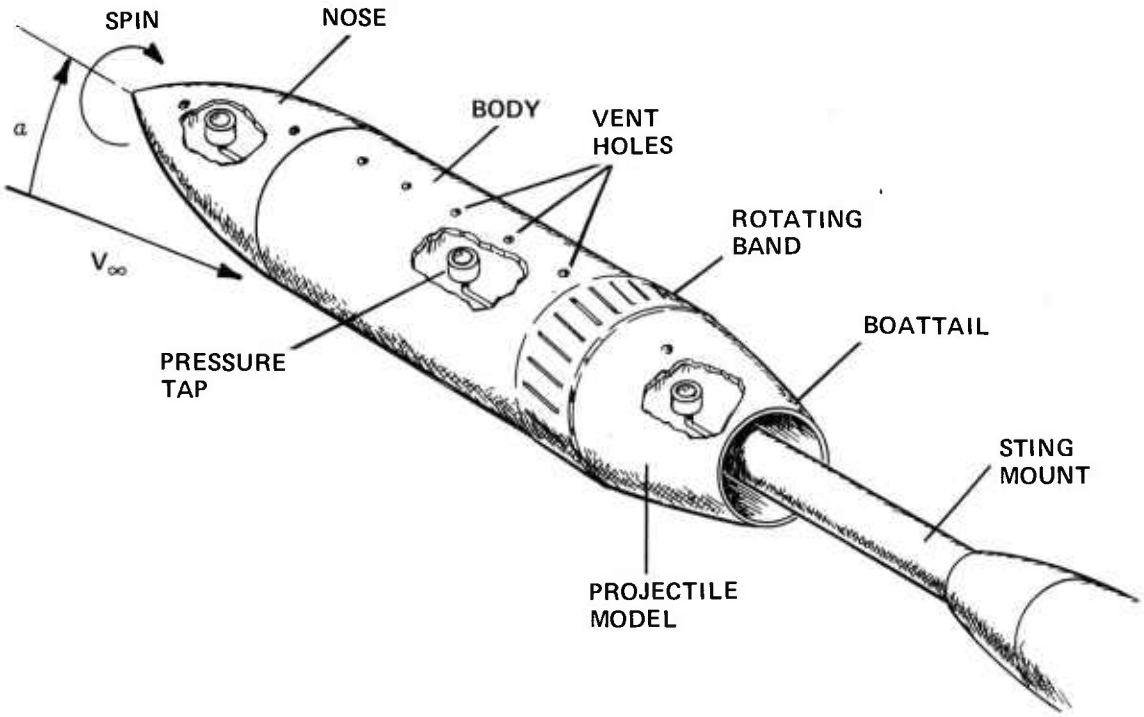

Figure A-57. Testing Technique Applied to a Spin-Stabilized Projectile

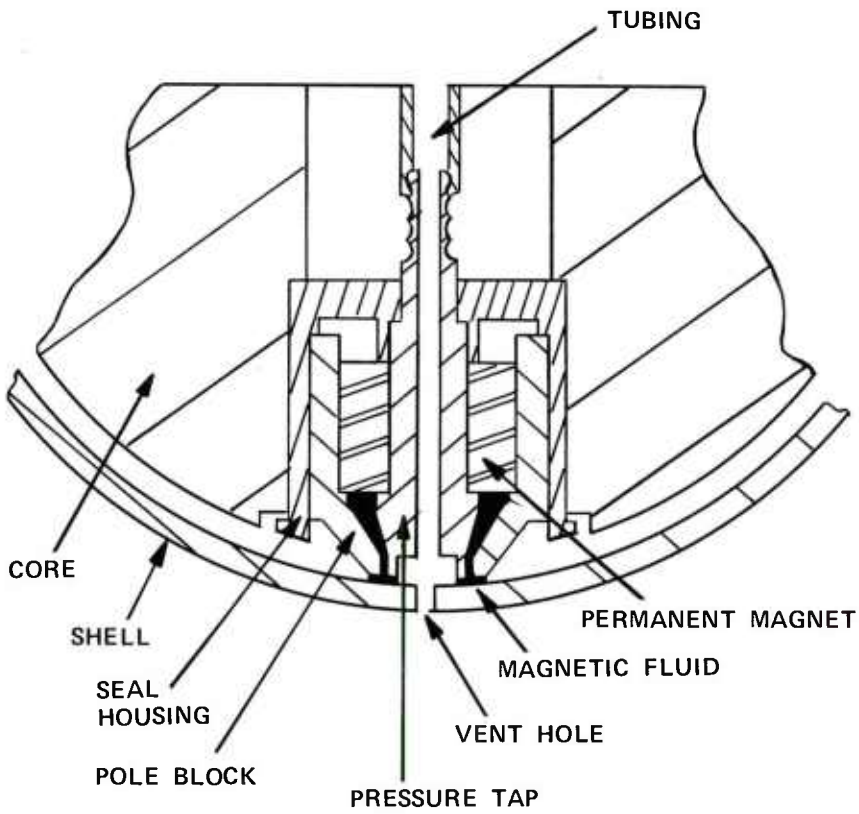

Figure A-58. Magnetic Fluid Seal

Table B-1. Wind-Tunnel Test Program for Force Tests

Test	Run	Date	V_∞ (mph)	V_∞ (fps)	t_a (°F)	P_a (mm-Hg)	R_d	ω (rpm)	$\hat{\omega}_{max}$	Type data	Configuration
478	11	4/22/75	10	14.6	57	762.0	40590	0→4300	6.02	C_L, C_D	#1 – Basic cylindrical body, end plates, and support strut
↓	12	↓	15	22.0	↓	↓	61160	↓	4.00	↓	↓
↓	13	↓	20	29.3	↓	↓	81460	↓	3.00	↓	↓
↓	14	↓	25	36.7	↓	↓	102030	↓	2.40	↓	↓
↓	2	4/15/75	30	44.0	51	↓	124860	↓	2.00	↓	↓
↓	3	↓	40	58.7	↓	↓	166570	↓	1.50	↓	↓
↓	15	4/22/75	50	73.3	57	↓	203780	↓	1.20	↓	↓
↓	4	4/15/75	60	88.0	50	↓	250620	↓	1.00	↓	↓
↓	16	4/22/75	70	102.7	57	↓	285520	↓	0.86	↓	↓
↓	5	4/15/75	80	117.3	49	↓	334070	↓	0.75	↓	↓
↓	6	↓	90	132.0	50	↓	375930	↓	0.67	↓	↓
↓	17	4/22/75	101	148.1	59	761.8	410150	↓	0.60	↓	↓
↓	18	↓	110	161.3	58	↓	446700	↓	0.54	↓	↓
↓	7	4/15/75	120	176.0	50	762.0	501240	↓	0.50	↓	↓
↓	19	4/22/75	130	190.7	58	761.8	528120	↓	0.46	↓	↓
↓	8	4/15/75	140	205.3	50	761.5	584690	↓	0.43	↓	↓
↓	9	↓	148	217.1	↓	↓	618290	↓	0.40	↓	↓
↓	23	4/21/75	10 to 148	14.6 to 217.1	66.5	761.0	–	–	–	C_L, C_D	#2 – Tare, two rods, end plates, and support strut
↓	24	4/21/75	10 to 148	14.6 to 217.1	59.0	758.0	–	–	–	C_L, C_D	#3 – Tare, two rods, end plates, support strut, and strut shield
↓	25	4/21/75	10 to 148	14.6 to 217.1	59.0	758.0	–	–	–	C_L, C_D	#4 – Tare, one rod, end plates, support strut, and strut shield

Table B-2. Wind-Tunnel Test Program for Pressure Tests

Case	Test	Run	Date	V_∞ (mph)	V_∞ (fps)	t_a (°F)	P_a (mm-Hg)	R_d	ω (rpm)	$\hat{\omega}$	ϕ (Degree)	Type data
1	461	1	1/23/75	60	88.0	47.0	771.4	256450	0	0	0 → 360	ΔP
2	484	1	7/ 7/75	↓	↓	74.5	757.5	229100	975	.25	in 5°	↓
3	502	3,4	8/14/75	↓	↓	83.5	761.5	223540	3025	.79	Increments	↓
4	503	3,4	8/15/75	90	132.0	80.0	762.5	339690	0	0	↓	↓
5	499	1,2	8/12/75	↓	↓	75.5	761.0	343750	975	.167	↓	↓
6	490	1,2	7/24/75	↓	↓	79.0	761.0	340200	3050	.52	↓	↓
7	462	1	1/27/75	120	176.0	55.0	768.2	496600	0	0	↓	↓
8	488	1,2	7/25/75	↓	↓	76.0	760.0	452680	975	.125	↓	↓
9	504	1,2	8/18/75	↓	↓	77.0	760.2	456110	2075	.26	↓	↓
10	491	1,2	7/24/75	↓	↓	87.0	760.0	441090	3050	.39	↓	↓

Table B-3. Comparison of Coefficients Obtained from Pressure and Force Tests

Case	V_∞ (fps)	$\hat{\omega}$	R_d	Data obtained from pressure tests		Data obtained from force tests	
				C_L	C_D	C_L	C_D
1	88	0	256450	.054	.759	0	.755
2	↓	.25	229100	-.177	.694	-.180	.690
3	↓	.79	223540	.595	.440	.560	.480
4	132	0	339690	-.266	.732	0	.700
5	↓	.167	343750	-.389	.692	-.530	.560
6	↓	.520	340200	0	.578	.06	.530
7	176	0	496600	-.049	.560	0	.440
8	↓	.125	452680	.402	.496	.240	.480
9	↓	.266	456110	-.201	.609	-.90 → -.29	.490
10	↓	.390	441090	.582	.516	.58	.510

DISTRIBUTION LIST FOR ED-TR-76070

Names	Copies
EDGEWOOD ARSENAL	
TECHNICAL DIRECTOR	
Attn: SAREA-TD-E	1
FOREIGN INTELLIGENCE OFFICER	1
CHIEF, LEGAL OFFICE	1
CHIEF, SAFETY OFFICE	1
CDR, US ARMY TECHNICAL ESCORT CENTER	1
PUBLIC HEALTH SERVICE LO	2
AUTHOR'S COPY, Development & Engineering Directorate	12
DIRECTOR OF CHEMICAL LABORATORY	
Attn: SAREA-CL-C	1
DIRECTOR OF DEVELOPMENT & ENGINEERING	
Attn: SAREA-DE-S	4
DIRECTOR OF TECHNICAL SUPPORT	
Attn: SAREA-TS-R	2
Attn: SAREA-TS-L	3
DEPARTMENT OF DEFENSE	
Administrator Defense Documentation Center Attn: Accessions Division Cameron Station Alexandria, VA 22314	12
Director Defense Intelligence Agency Attn: DIR-4G1 Washington, DC 20301	1
DEPARTMENT OF THE ARMY	
HQDA (DAMO-ODC) WASH DC 20310	1
Chief, Office of Research, Development & Acquisition	
Attn: DAMA-CSM-CM	1
Attn: DAMA-ARZ-D Washington, DC 20310	1
US ARMY MATERIEL DEVELOPMENT AND READINESS COMMAND	
Commander US Army Materiel Development and Readiness Command	
Attn: DRCSF-C	1
Attn: DRCDE-WB	1
Attn: DRCDE-R/Dr. D. Stefanye	1
Attn: DRCDE-DW-W/Mr. J. Hughes 5001 Eisenhower Ave Alexandria, VA 22333	1
Commander US Army Foreign Science & Technology Center	
Attn: DRXST-IS1 220 Seventh St., NE Charlottesville, VA 22901	2
US ARMY ARMAMENT COMMAND	
Commander US Army Armament Command	
Attn: DRSAR-RD/Mr. J. Brinkman	1
Attn: DRSAR-RD/Dr. Gerald Penrod	1
Attn: DRSAR-RDG-A/Mr. J. Miller	1
Attn: DRSAR-RDG/Mr. I. Marcus	1
Attn: DRSAR-RDT Rock Island, IL 61201	1
Commander Frankford Arsenal	
Attn: Library Branch, TSP-L Bldg 51-2 Philadelphia, PA 19137	1
Commander US Army Missile Command	
Attn: DRSMI-R	1
Attn: DRSMI-RDK/Mr. R. Deep Redstone Arsenal, AL 35809	1
Commander US Army Picatinny Arsenal	
Attn: SARPA-AD-D/Mr. S. Wasserman	1
Attn: SARPA-FR-S-A/Mr. R. Kline	1
Attn: SARPA-FR-S-A/Mr. S. Kahn Dover, NJ 07801	1
US ARMY TRAINING & DOCTRINE COMMAND	
Commandant US Army Missile & Munitions Center & School	
Attn: ATSK-CTD-FM	1
Attn: ATSK-CTD-FC	1
Attn: ATSK-TEB-E Redstone Arsenal, AL 35809	1
Commandant US Army Ordnance Center & School	
Attn: ATSL-CTD-MS-C APG-Aberdeen Area	1
US ARMY TEST & EVALUATION COMMAND	
Record Copy CDR, APG	
Attn: STEAP-AD-R/RHA APG-Edgewood Area, Bldg E5179	1

Names	Copies
CDR, APG	
Attn: STEAP-TL	1
APG-Aberdeen Area	
DEPARTMENT OF THE NAVY	
Commander	
US Naval Ordnance Systems Command	
Attn: ORD-0631	1
Attn: ORD-035	1
Attn: ORD-5524	1
Washington, DC 20360	
Director	
US Office of Naval Research	
Attn: Mr. S. Curley	1
495 Summer Street	
Boston, MA 02210	
Commander	
US Naval Surface Weapons Center	
Attn: Code 312/Mr. R. Regan	1
Attn: Code 312/Mr. S. Hastings	1
Attn: Code 730, Technical Library	1
Silver Spring, MD 20910	
Commander	
US Naval Surface Weapons Center	
Dahlgren Laboratories	
Attn: Code KBB/Dr. T. Clare/Mr. P. Daniels	2
Dahlgren, VA 22448	
Commander	
US Naval Weapons Center	
Attn: Code 533/Technical Library	1
Attn: Code 6003/Dr. W. Haseltine	1
China Lake, CA 93555	
Director	
US Naval Research Laboratory	
Attn: Technical Infl. Division	1
Attn: Code 7720/Dr. A. Kolb/Dr. E. McClean	2
Washington, DC 20390	
US AIR FORCE	
Commander	
Armament Development & Test Center	
Attn: ADBOS-12/Dr. D. Daniel	1
Attn: ADBOS-12/Mr. E. Sears	1
Eglin AFB, FL 32542	
Commander	
AFATL	
Attn: DLRA/Technical Library	1
Eglin AFB, FL 32542	
Commander	
AFFDL	1
Wright-Patterson AFB, OH 45433	

Names	Copies
Commander	
Aeronautical Systems Division	
Attn: ASD/ASAMCC	1
Wright-Patterson AFB, OH 45433	
ADDED ADDRESSEES	
Commander	
US Army Research Office	
Attn: DRXRD-EG-I-492/Mr. R. E. Singleton	1
P. O. Box 12211	
Research Triangle Park, NC 27709	
Director	1
US Army BMD	
Advanced Technology Center	
P. O. Box 1550	
Huntsville, AL 35809	
Environmental Sciences Services Administration	
Attn: Code 82.70/J. W. Wright	1
Boulder, CO 80301	
Director	
National Bureau of Standards	
Attn: Technical Library	1
US Department of Commerce	
Washington, DC 20234	
Director	
National Aeronautics and	
Space Administration	
Attn: Technical Library	1
Goddard Space Flight Center	
Greenbelt, MD 20771	
Director	
National Aeronautics and	
Space Administration	
Attn: MS 185/Technical Library	1
Langley Station	
Hampton, VA 23365	
Director	
National Aeronautics and	
Space Administration	
Scientific and Technical	
Information Facility	
Attn: SAK/DL	1
P. O. Box 33	
College Park, MD 20740	
ARO, Inc	
Attn: Technical Library	1
Arnold AFB, TN 37389	

DISTRIBUTION LIST FOR ED-TR-76070 (Contd)

Names	Copies
Sandia Laboratories	
Attn: Areodynamics Department	1
Attn: Org 5620/Mr. R. Maydew	1
Attn: Div 5625/Mr. W. Curry/Mr. W. Caudle	2
Attn: Div 5625/Mr. H. Vaughn/Mr. A. Wilson	2
Albuquerque, NM 87115	
California Institute of Technology	
Aeronautics Department	
Attn: Professor H. Liepmann	1
Pasadena, CA 91102	
California Institute of Technology	
Guggenheim Aeronautical Laboratory	
Attn: Technical Library	1
Pasadena, CA 91103	
Director	1
Guggenheim Aerospace Laboratory	
New York University	
New York Heights	
New York, NY 10053	
Calspan Corporation	
Attn: Library	1
P. O. Box 235	
Buffalo, NY 14421	
Director	1
Applied Physics Laboratory	
Johns Hopkins University	
Laurel, MD 20810	
Director	1
Department of Aeronautics	
Johns Hopkins University	
34th & Charles Sts	
Baltimore, MD 21218	
Massachusetts Institute of Technology	
Department of Aeronautics	
and Astronautics	
Attn: Technical Library	1
77 Massachusetts Avenue	
Cambridge, MA 02139	
Ohio State University	
Department of Aeronautical and	
Astronautical Engineering	
Attn: Technical Library	1
Columbus, OH 43210	
University of Maryland	
Department of Aeronautical Engineering	
Attn: Professor A. W. Sherwood	1
Attn: Professor W. L. Melnik	1
College Park, MD 20740	

Names	Copies
University of Maryland	
Department of Mechanical Engineering	
Attn: R. C. Marks	1
Attn: Dr. Sallet	1
College Park, MD 20740	
University of Virginia	
Department of Aeronautical Engineering	
Attn: Professor I. Jacobson	1
Charlottesville, VA 22901	
Iowa State University	
Department of Aeronautical Engineering	
Attn: Professor J. D. Iverson	1
Ames, Iowa 50010	
Director	
US Army Ballistics Research Laboratories	
Attn: DRXBR/Dr. C. Murphy	1
Attn: DRXBR/A. Platou	1
Attn: DRXBR/R. Krieger	1
Attn: DRXBR/Dr. Sedney	1
Attn: DRXBR/Dr. A. Mark	1
Attn: DRXBR/R. McCoy	1
Attn: DRXBR/J. Whiteside	1
APG-Aberdeen Area	